Development of the β-NMR technique towards the study of hyperfine anomalies in short-lived nuclei

Weiterentwicklung der β-NMR-Technik zur Untersuchung der Hyperfeinanomalien in kurzlebigen Kernen

Zur Erlangung des Grades eines Doktors der Naturwissenschaften (Dr. rer. nat.)
Genehmigte Dissertation von Marcus Jankowski aus Oldenburg (Oldb.)
Tag der Einreichung: 25.06.2024, Tag der Prüfung: 17.07.2024

1. Gutachten: Prof. Dr. Thorsten Kröll
2. Gutachten: Prof. Dr. Magdalena Kowalska
Darmstadt, Technische Universität Darmstadt

TECHNISCHE UNIVERSITÄT DARMSTADT

Physics Department
Institut für Kernphysik
AG Thorsten Kröll

Development of the β-NMR technique towards the study of hyperfine anomalies in short-lived nuclei
Weiterentwicklung der β-NMR-Technik zur Untersuchung der Hyperfeinanomalien in kurzlebigen Kernen

Accepted doctoral thesis by Marcus Jankowski

Date of submission: 25.06.2024
Date of thesis defense: 17.07.2024

Darmstadt, Technische Universität Darmstadt

Erklärungen laut Promotionsordnung

§ 8 Abs. 1 lit. c PromO

Ich versichere hiermit, dass die elektronische Version meiner Dissertation mit der schriftlichen Version übereinstimmt.

§ 8 Abs. 1 lit. d PromO

Ich versichere hiermit, dass zu einem vorherigen Zeitpunkt noch keine Promotion versucht wurde. In diesem Fall sind nähere Angaben über Zeitpunkt, Hochschule, Dissertationsthema und Ergebnis dieses Versuchs mitzuteilen.

§ 9 Abs. 1 PromO

Ich versichere hiermit, dass die vorliegende Dissertation selbstständig und nur unter Verwendung der angegebenen Quellen verfasst wurde.

§ 9 Abs. 2 PromO

Die Arbeit hat bisher noch nicht zu Prüfungszwecken gedient.

Darmstadt, 25.06.2024

M. Jankowski

Abstract

Die Kenntnis der magnetischen Dipolmomente von Atomkernen ist für die Untersuchung der Kernstruktur sehr wertvoll. Da diese Kerneigenschaft in hohem Maße von der Konfiguration der ungepaarten Nukleonen im Kern abhängt, kann sie als Referenz dienen, um Modellvorhersagen zu überprüfen und deren zugrunde liegenden Annahmen zu bewerten. Wenn die magnetischen Momente mit großer Genauigkeit bestimmt werden, können kleine Effekte, wie z. B. die Hyperfeinanomalie, die durch die endliche Größe des Kerns und insbesondere die Verteilung der Kernmagnetisierung hervorgerufen wird, untersucht werden. Informationen über die Hyperfeinanomalie können dazu beitragen, Parameter der Kernstrukturmodelle einzuschränken. Die Bedeutung experimentell ermittelter magnetischer Momente und ihrer Präzision ist daher nicht zu unterschätzen.

β-detektierende Kernspinresonanzspektroskopie (β-NMR) ist eine leistungsstarke, spektroskopische Methode, mit der die magnetischen Momente von kurzlebigen, β-emittierenden Kernen mit großer Präzision bestimmt werden können. Solche Untersuchungen werden am VITO-Experiment in der Forschungseinrichtung ISOLDE am CERN durchgeführt. An diesem experimentellen Aufbau wurde kürzlich eine Reihe von Verbesserungen vorgenommen, um seine Auflösung weiter zu erhöhen. Unter anderem wurden ein supraleitender Magnet und ein neues Datenerfassungssystem installiert, welches ein wesentlicher Bestandteil der für diese Dissertation durchgeführten Arbeiten ist und hier im Detail vorgestellt wird. Es verwendet ein Field Programmable Gate Array, um die detektierten β-Teilchen in Echtzeit durch eine Auswahl an Eigenschaften, wie z. B. ihre Ankunftszeit oder das Integral ihrer Signale, zu charakterisieren. Die Eigenschaften werden für alle individuellen β-Ereignisse gespeichert, was eine flexible und tiefgehende Datenanalyse ermöglicht. Darüber hinaus wurde eine neue Methode zur Auswertung der β-NMR-Spektren entwickelt, die die Frequenz- und Zeitabhängigkeit der gemessenen Signale berücksichtigt und eine umfassendere Darstellung der aufgenommenen Daten durch einen zweidimensionalen Fit ermöglicht.

In dieser Arbeit werden die ersten β-NMR-Untersuchungen von kurzlebigem ^{47}K unter Verwendung des neuen, verbesserten Versuchsaufbaus vorgestellt. Das magnetische Moment $\mu_I = 1.936\,182(19)\mu_\mathrm{N}$ wird aus diesen Messungen bestimmt. Die Unsicherheit beträgt $10\,\mathrm{ppm}$, was einer Verbesserung um zwei Größenordnungen gegenüber dem Literaturwert entspricht. Die differentielle Hyperfeinanomalie zwischen stabilem ^{39}K und ^{47}K wird zu $^{39}\Delta^{47} = 0.360(9)\,\%$ bestimmt. Der hier berechnete Wert wird mit der theoretischen Hyperfeinanomalie verglichen, die durch die Kombination von Atomtheorie (Hartree-Fock) und Kerntheorie (Density Functional Theory) berechnet wurde. Es wird gezeigt, dass ausschließlich von magnetischen Momenten ausgehend die relativen Beiträge von Spin und Bahndrehimpuls zu den magnetischen Momenten von ^{39}K und ^{47}K nicht genau bestimmt werden können, die differentielle Hyperfeinanomalie jedoch in der Lage ist, als zusätzliche Bedingung die Anzahl der möglichen Zusammensetzungen der magnetischen Momente stark zu reduzieren. Diese Analyse deutet darauf hin, dass Experiment und Theorie konsistent sind, wenn im theoretischen Ansatz der orbitale Beitrag von ^{39}K und ^{47}K unverändert bleibt, aber der Spinbeitrag im Vergleich zu den berechneten Werten verringert wird. Zukünftige theoretische Arbeiten und weitere Studien an anderen K-Isotopen und anderen Isotopenketten werden zeigen, ob diese Schlussfolgerung allgemeiner ist. Somit lässt sich sagen, dass präzise Messungen der Hyperfeinanomalie in instabilen Kernen es ermöglichen sollten, Kernstrukturmodelle zu testen, die Fähigkeit solcher Modelle zur Vorhersage magnetischer Momente zu erhöhen und schließlich das Verständnis des Operators des magnetischen Moments zu verbessern.

Abstract

The knowledge of magnetic dipole moments of atomic nuclei is very valuable for nuclear structure research. Because this nuclear property depends to a large degree on the configuration of the unpaired nucleons in the nucleus, it can serve as a reference to benchmark the model predictions and assess its underlying assumptions. If magnetic moments are determined with great precision, one can address small effects, such as the hyperfine anomaly, which arises from the finite size of the nucleus, and particularly the distribution of nuclear magnetisation. Obtaining information on the hyperfine anomaly can help to constrain nuclear structure models. The importance of experimentally determined magnetic moments and the quest for reaching higher precision can therefore not be underestimated.

β-detected nuclear magnetic resonance (β-NMR) is a powerful spectroscopic technique that is used to determine the nuclear magnetic moments of short-lived β-emitting nuclei with great precision. Such studies are conducted at the VITO beamline at the ISOLDE facility at CERN. This setup has recently undergone several major upgrades to further enhance its resolution, including the installation of a $4.7\,\mathrm{T}$ superconducting magnet and a new data acquisition system. The latter system was a major part of the work conducted for this thesis and is presented in detail. It uses a field-programmable gate array to characterise the detected β particles in real-time by a selection of their properties, such as time of arrival or signal integral. The properties are saved for all individual β events, enabling a flexible in-depth data analysis. In addition, a new method of evaluating the β-NMR spectra was developed. It considers the frequency and the time dependency of the measured signals and allows for a more comprehensive representation of the recorded data through a two-dimensional fit.

This thesis presents the first β-NMR studies on short-lived ^{47}K using the newly upgraded experimental setup. The magnetic moment $\mu_I = 1.936\,182(19)\mu_\mathrm{N}$ was derived from these measurements. It was possible to reduce the uncertainty to $10\,\mathrm{ppm}$, which is two orders of magnitude smaller than in the literature. The differential hyperfine anomaly between stable ^{39}K and ^{47}K was also determined at $^{39}\Delta^{47} = 0.360(9)\,\%$. This precisely measured differential hyperfine anomaly is then compared to the theoretical hyperfine anomaly obtained by combining atomic (Hartree-Fock) and nuclear (Density Functional Theory) theoretical approaches. It is shown that in contrary to the magnetic moments alone, which cannot pinpoint the relative contributions of spin and orbital angular momentum to the total magnetic moment of ^{39}K and ^{47}K, their differential hyperfine anomaly provides a strong constraint on the composition of the magnetic moment. This analysis points to the conclusion that consistency is achieved when the orbital contribution to the magnetic moment of both ^{39}K and ^{47}K remains unchanged, but their spin contributions are lowered with respect to the calculated values. Ongoing theoretical efforts and further studies on other K isotopes and other isotopic chains will show whether this conclusion is more universal. In summary, as shown here, precise measurements of the hyperfine anomaly in unstable nuclei should allow to test nuclear structure models, to increase the ability of such models to predict magnetic moments, and finally to improve understanding of the magnetic moment operator.

Contents

List of Figures

1. Introduction

Magnetic moments are important properties that describe the nucleus and help to understand its structure [85]. They are dependent on contributions from the nucleons in the nucleus, i.e. protons and neutrons, but they are especially sensitive to unpaired nucleons. As such, magnetic moments give rise to assessing nuclear structure models. A prime example is the extreme single particle model which assumes that a single unpaired nucleon of a nucleus moves in a potential generated by all other nucleons. It would then be possible to fully describe the nucleus by its unpaired nucleon. The assumptions and parameters can thus be directly probed with the magnetic moment. Numerous measuring techniques for magnetic moments exist [108], for example nuclear magnetic resonance (NMR) which is typically used for stable nuclei. The magnetic moments of radioactive nuclei can provide additional information on the structure of nuclei, but they require more effort to obtain. A common approach to obtain magnetic moments of short-lived isotopes is laser spectroscopy, which observes differences in the hyperfine structure along isotopic chains. Another, often significantly more precise technique is β-detected NMR [50], which relies on detecting the asymmetry exhibited in the β decay of nuclei with polarised nuclear spins [47].

A setup conducting β-NMR studies is the VITO beamline at the ISOLDE facility at CERN. It was initially commissioned in 2016 [73, 71] and has undergone several upgrades since [45, 30]. A recent achievement at VITO was the determination of the magnetic dipole moment of a short-lived nucleus with parts-per-million accuracy [50]. Optical pumping was employed to polarise the nuclear spin of ^{26}Na. The isotopes were then implanted into an ionic liquid sample, which resulted in resonances with a width of several ppm. Among the latest improvements to the setup is the installation of a $4.7\,\mathrm{T}$ superconducting magnet [63], new detectors a new data acquisition system.

This thesis focuses on the technical aspects of the upgraded beamline and in particular the data acquisition system VCS, which was developed in the scope of this work. The aim of VCS is to provide the highest-possible flexibility during the data acquisition and the analysis. This is achieved by using an oscilloscope card with an integrated field-programmable gate array (FPGA) that processes each detected β particle by a selection of properties, such as its time of arrival or its signal amplitude. The properties of all β events are saved and allow for a comprehensive analysis. One such approach based on the data recorded with VCS is presented in this thesis. It exploits the time of arrival of all recorded β particles to evaluate the β decay asymmetry, not only as a function of the frequency applied during the β-NMR scan, but also as a function of the time since the implantation of the isotope into the sample. This two-dimensional method is thereby able to consider the relaxation of the signal during a β-NMR measurement for the first time and yields a more complete representation of the data. The obtained line shapes and the enhancements resulting from this two-dimensional approach are discussed in detail.

A series of commissioning experiments of the upgraded setup and VCS took place in 2022. These β-NMR studies of ^{47}K implanted into an ionic liquid allow to obtain the magnetic moment $\mu_I(^{47}\mathrm{K}) = 1.936\,182(19)\mu_\mathrm{N}$ with two orders of magnitude greater precision than the literature value. More importantly, the experiments also serve as preparation for future measurements at VITO: The differential hyperfine anomaly $^{39}\Delta^{47} = 0.360(9)\,\%$ of the two isotopes ^{39}K and ^{47}K is determined with unprecedented precision. By calculating the distribution of the magnetisation in the nucleus and the spin asymmetries using Density Functional Theory (DFT), it is possible to obtain combinations of spin and orbital contributions that yield the magnetic moments of the two

isotopes [9]. The differential hyperfine anomaly determined in this thesis yields an additional constraint to these spin and orbital contributions, which now need to reproduce the two magnetic moments and the differential hyperfine anomaly linking them. This significantly narrows down the possible combinations of the two contributions. It is then demonstrated that the spin contribution to the magnetic moments needs to be reduced with respect to the outcome of the DFT calculations. This result can help to improve the nuclear structure models [44]. In return, it can be confirmed that this method of deriving the differential hyperfine anomaly with β-NMR is sensitive to the spin and orbital contribution to the magnetic moment and thus allows to draw conclusions on the distribution of the magnetisation in the nucleus [9].

After presenting the fundamentals of nuclear and atomic theory required for this thesis in Chapter 2, the techniques of NMR and β-NMR follow in Chapter 3. The VITO beamline at ISOLDE will be described in Chapter 4, including a detailed description of the data acquisition system VCS. Chapter 5 presents the preparation of the experiments and the data analysis, in particular the two-dimensional approach of representing the recorded β-NMR spectra and the derivations of the magnetic moment $\mu_I(^{47}\mathrm{K})$ and the differential hyperfine anomaly $^{39}\Delta^{47}$. It is then concluded with the discussion in Chapter 6 and the summary and outlook in Chapter 7.

2. Theory

This chapter presents the fundamentals of the theory required in the scope of this thesis. The nuclear theory comprises the nuclear shell model and the introduction of spins, followed by the derivation of electromagnetic moments. An overview on the atomic theory for the fine structure and the hyperfine structure is given, and subsequently an explanation of the hyperfine anomaly.

2.1. Nuclear shell model and spin

A range of nuclei with certain numbers of protons Z and/or neutrons N shows properties that make them distinct even compared to nuclei that differ by only a few nucleons, e.g. in terms of their stability. These numbers Z and N are called magic numbers and take values 2, 8, 28, 50, 82 for protons and neutrons and 126 for neutrons [80, 40]. If both Z and N take one of these values, the nuclei are also referred to as doubly magic. A model that is able to yield these magic numbers and many properties of the corresponding nuclei is the nuclear shell model that describes the nucleus in analogy to the orbitals of electrons. It considers the nucleons to occupy single-particle orbitals in a mean-field potential. This mean field potential is induced by the other nucleons in the nucleus. The Hamiltonian describing this system of A nucleons with kinetic energy T and potential energy V then takes the shape

$$H = T + V = \sum_{i=1}^{A} \frac{-\hbar^2}{2m_i}\nabla_i^2 + \sum_{i,j=1,i<j}^{A} v(\boldsymbol{r_i}, \boldsymbol{r_j}) \tag{2.1}$$

$$= \left[T + \sum_{i=1}^{A} v(\boldsymbol{r})\right] + \left[V - \sum_{i=1}^{A} v(\boldsymbol{r})\right] \tag{2.2}$$

$$= T + V_{\mathrm{MF}} + V_{\mathrm{res}}, \tag{2.3}$$

where m_i is the mass of a nucleon and $\boldsymbol{r}$ its position. The variables V_{MF} and V_{res} are the mean-field potential and the residual interactions.

The total angular momentum of a nucleon is described by $\boldsymbol{j}$ and results from the coupling of the orbital angular momentum $\boldsymbol{l}$ and the intrinsic angular momentum $\boldsymbol{s}$, also known as spin, of this nucleon. Consequently, the nuclear spin $\boldsymbol{I}$ results from coupling all spins $\boldsymbol{j}$ of all nucleons. It takes the values $\boldsymbol{I}^2 = \hbar^2 I(I+1)$ and $I_z = m_I\hbar$ with $m_I = -I, \ldots, I$ [53]. The nuclear spin I is determined by unpaired nucleons, i.e. paired protons or neutrons do not contribute to I. Figure 2.1 shows the order of the nuclear levels with the respective quantum numbers, and the magic numbers.

2.2. Electromagnetic moments

It is possible to describe the charge and current distribution of a nucleus with an expansion into a series of magnetic moments and electric moments [96]. The first terms of this expansion, namely the magnetic dipole moment and the electric quadrupole moment, prevail this description and are briefly introduced in this section.

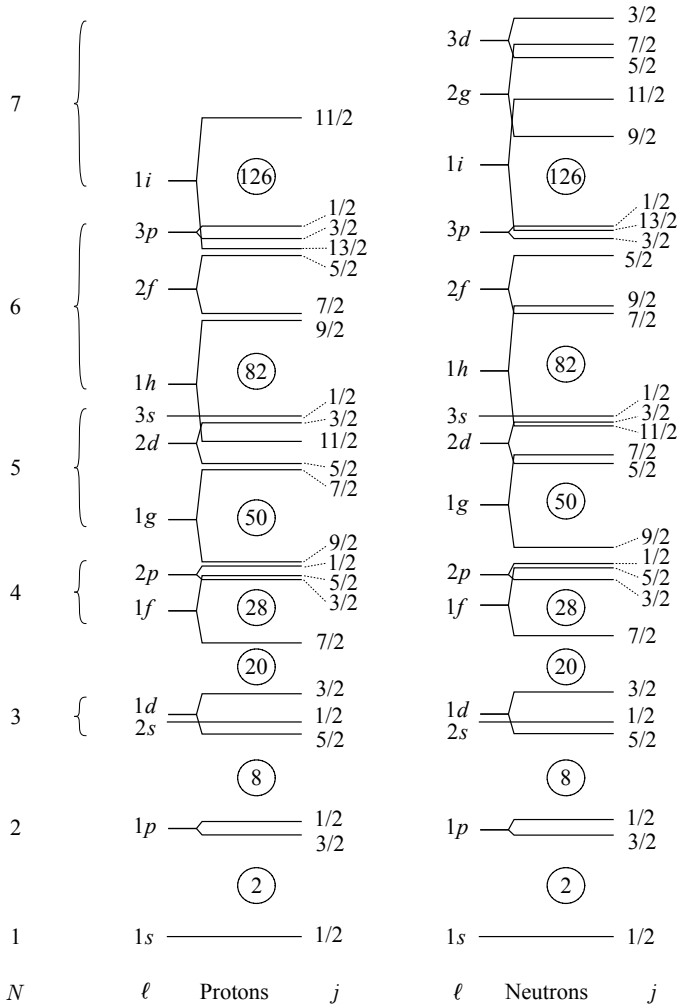

Figure 2.1.: Ordering of the levels in the nuclear shell model including the spin-orbit splitting (adapted from [92]). Shown along the levels are the corresponding principal quantum number N, the orbital angular momentum l and total angular momentum j of the nucleons as well as the magic numbers 2, 8, 20, 28, 50, 82 and 126.

2.2.1. Magnetic dipole moment

The magnetic dipole moment, often referred to as the magnetic moment, arises from two contributions, namely the orbital angular momentum of all nucleons and their intrinsic angular momentum (spin). Consequently, the operator of the magnetic moment considers the sum of the contributions from all nucleons with

$$\boldsymbol{\mu_I} = \frac{\mu_\mathrm{N}}{\hbar}\left(\sum_{i=1}^{A} g_l^i \boldsymbol{l_i} + \sum_{i=1}^{A} g_s^i \boldsymbol{s_i}\right), \tag{2.4}$$

where g_l^i and g_s^i are the orbital and spin gyromagnetic ratios of the i-th nucleon and $\boldsymbol{l_i}$ and $\boldsymbol{s_i}$ represent the respective operators of the orbital angular momentum and spin of the nucleons [96]. The nuclear magneton $\mu_\mathrm{N} = e/(2m_\mathrm{p})$ is often given as the unit of the magnetic moment.

It is also possible to express operator of the magnetic moment as

$$\boldsymbol{\mu_I} = \mu_\mathrm{N} g_I \boldsymbol{I}, \tag{2.5}$$

where $\boldsymbol{I}$ is the operator of the nuclear spin and g_I is the nuclear g-factor. The expectation value along the z-orientation yields the magnetic moment

$$\mu_I = \langle I, m_I = I | \boldsymbol{\mu_z} | I, m_I = I \rangle = g_I I \mu_\mathrm{N}. \tag{2.6}$$

This means that $\mu_I = 0$ for $I = 0$.

One simplification to compute the magnetic moment for nuclei with odd A is the so-called single particle model. It assumes that all nucleons pair to spin zero, except for one valence nucleon, which then gives the magnetic moment of the entire nucleus with

$$\mu_I = \left[\left(j - \frac{1}{2} \right) g_l + \frac{1}{2} g_s \right] \text{ for } j = l + 1/2 \tag{2.7}$$

$$\mu_I = \frac{j}{j+1} \left[\left(j + \frac{3}{2} \right) g_l - \frac{1}{2} g_s \right] \text{ for } j = l - 1/2, \tag{2.8}$$

where g_l and g_s are the orbital and spin g-factors of a free proton or a free neutron [113, 81]. A magnetic moment based on the single particle model is also called Schmidt moment. These values show deviations to the experimentally determined magnetic moments since a possible mixing of wave functions is not considered. Therefore, the g-factors are often replaced with effective g-factors that include some corrections to obtain a better approximation of nuclei with single unpaired nucleons [26].

Techniques to determine magnetic dipole moments μ_I are for example laser spectroscopy, elastic magnetic electron scattering and β-NMR [87, 117, 66, 32, 50].

2.2.2. Electric quadrupole moment

The electric quadrupole moment, commonly referred to as quadrupole moment, is a consequence of an asymmetrical charge distribution in the nucleus. As such, it provides information on the deformation of the nucleus, i.e. its sign represents the nucleus being oblate or prolate [26, 13]. Its operator is

$$\boldsymbol{Q} = \sqrt{\frac{16\pi}{5}} \sum_i^A q_i r_i^2 Y_2^0(\theta_i, \phi_i) = \sum_i^A q_i r_i^2 (2\cos^2\theta_i - 1) \tag{2.9}$$

with $q_i = e$ being the charge of protons and $q_i = 0$ for neutrons. Analogue to Equation (2.6), the observed quantity is

$$eQ = \langle I, m_I = I | \boldsymbol{Q} | I, m_I = I \rangle. \tag{2.10}$$

For $I < 1$, the observable quadrupole moment is zero even though it is possible that nuclei with spin $I = 0$ or $I = 1/2$ are deformed [82]. A positive quadrupole moment indicates a prolate (elongated) nucleus, while a negative quadrupole moment indicates an oblate (flattened) nucleus.

2.3. Atomic theory

Given here is an overview on the atomic theory required for the understanding of this thesis. After a brief introduction to the fine structure of an atom, the hyperfine structure is explained before it is applied with optical pumping described in Section 3.2.1. What follows is an overview on the hyperfine anomaly that describes effects on the hyperfine structure arising from the finite size of the nucleus.

2.3.1. Fine structure

The electrons of an atom moving around the nucleus induce a magnetic field B_{int} that can couple with the magnetic dipole moment μ_S of the electrons and causes the energy levels in the atom to split. When the spin $\boldsymbol{S}$ and the orbital angular momentum $\boldsymbol{L}$ of the electron couple, its total angular momentum can be expressed with $\boldsymbol{J}$, where $\boldsymbol{J}$ takes the values $J = |L - S|, \ldots, L + S$. These energy levels have $2J + 1$ possible projections ranging from $m_J = -J$ to $m_J = J$.

2.3.2. Hyperfine structure

Analogue to the fine structure, the electromagnetic field induced by the electrons can also couple with the nuclear multipole moments through the so-called hyperfine interaction [23]. This results in the total angular momentum $\boldsymbol{F} = \boldsymbol{I} + \boldsymbol{J}$ of the atom, whose levels are known as the hyperfine structure.

The first contribution to the hyperfine structure considered here is the interaction of the magnetic field $\boldsymbol{B}_{\mathbf{int}}$ induced by the electrons and the magnetic dipole moment $\boldsymbol{\mu_I}$ of the nucleus [23], whose Hamiltonian can be expressed as

$$H_{\mathrm{m}} = -\boldsymbol{\mu_I} \cdot \boldsymbol{B}_{\mathbf{int}}. \tag{2.11}$$

Resulting from this interaction is a shift in energy

$$\Delta E_{\mathrm{m}} = \frac{A}{2} K, \tag{2.12}$$

where $K = F(F+1) - J(J+1) - I(I+1)$ with $F = |J - I|, \ldots J + I$ and A is the magnetic dipole hyperfine parameter, which is defined as

$$A = \frac{\mu_I B_{\mathrm{int}}}{IJ}. \tag{2.13}$$

Here, μ_I is the magnetic dipole moment of the nucleus and B_{int} is the magnetic field at the nucleus. Because of $\mu_I = 0$ for $I = 0$, this shift in energy occurs only for nuclei with spin $I > 0$.

The second contribution to the hyperfine structure is the interaction of the quadrupole moment $\boldsymbol{Q}$ and the electric field gradient $\boldsymbol{\nabla E}$ at the position of the nucleus. It can be described by the Hamiltonian

$$H_{\mathrm{Q}} = -\frac{1}{6} \boldsymbol{Q} \cdot \boldsymbol{\nabla E}. \tag{2.14}$$

The energy shift is then given by

$$\Delta E_{\mathrm{Q}} = \frac{B}{4} \frac{\frac{3}{2} K(K+1) - 2I(I+1)J(J+1)}{I(2I-1)J(2J-1)}, \tag{2.15}$$

in the first order of perturbation theory [23], with the electric quadrupole hyperfine parameter B, which is defined as

$$B = eQ \left\langle \frac{\delta^2 V_e}{\delta z^2} \right\rangle. \tag{2.16}$$

Here, Q is the electric quadrupole moment and $\left\langle \frac{\delta^2 V_e}{\delta z^2} \right\rangle$ is the electric field gradient. A quadrupole moment Q is only present when $I > 1/2$, therefore this energy shift ΔE_{Q} occurs only for $I > 1/2$. The total shift in energy for the hyperfine structure is then given by

$$\Delta E = \Delta E_{\mathrm{m}} + \Delta E_{\mathrm{Q}} \tag{2.17}$$

The hyperfine parameters A and B of an isotopic chain are typically measured with laser spectroscopy [66]. If the hyperfine parameters A_{ref} and B_{ref} of an isotope with spin I_{ref}, magnetic dipole moment $\mu_{I,\,\mathrm{ref}}$ and electric quadrupole moment Q_{ref} are known [66], it is possible to obtain the corresponding parameters I, μ_I and Q of another isotope with

$$\mu_I = \mu_{I,\,\mathrm{ref}} \frac{I}{I_{\mathrm{ref}}} \frac{A}{A_{\mathrm{ref}}} \tag{2.18}$$

$$Q = Q_{\mathrm{ref}} \frac{B}{B_{\mathrm{ref}}}. \tag{2.19}$$

Consequently, laser spectroscopy allows to gain information on the structure of the nuclei, its wave functions and possible deformations.

2.3.3. Hyperfine anomaly

The description of the hyperfine structure in the previous section was made under the assumption that the nucleus is point-like. However, the nucleus has a finite size. The magnetic field B_{int} induced by the electrons is hence not constant over the nuclear volume because $s_{1/2}$ and, to a smaller degree, $p_{1/2}$ electrons have a non-zero probability of penetrating the nucleus. Since the size of the nucleus is isotope-dependent, the interaction of B_{int} and the nucleus is also isotope-dependent. What follows is that

$$\frac{A}{A_{\mathrm{ref}}} \neq \frac{\mu_I}{I} \frac{I_{\mathrm{ref}}}{\mu_{I,\,\mathrm{ref}}} = \frac{g_I}{g_{I,\,\mathrm{ref}}}. \tag{2.20}$$

The ratio A/A_{ref} of the hyperfine parameters not being equal to the ratio $g_I/g_{I,\,\mathrm{ref}}$ of the nuclear g-factors ($g_I = \mu_I/(I\mu_{\mathrm{N}})$) contradicts Equation (2.18). Therefore, Equation (2.18) used to determine the magnetic dipole moment μ_I based on the hyperfine structure is not fully accurate [36]. This so-called differential hyperfine anomaly (HFA) arises from two effects [90]. The first is the Bohr-Weisskopf effect which reflects the distribution of the nuclear magnetisation [14, 12] while the second one, the Breit-Rosenthal effect, considers the distribution of the nuclear charge [97].

The two factors ϵ_{BW} and ϵ_{BR} are introduced to correct for the Bohr-Weisskopf effect and the Breit-Rosenthal effect, respectively [25]. Consequently, the hyperfine parameter is then written as

$$A = A_{\mathrm{point}}(1 + \epsilon_{\mathrm{BW}})(1 + \epsilon_{\mathrm{BR}}), \tag{2.21}$$

with A_{point} being the hyperfine parameter under the assumption of a point-like nucleus. The magnetic moment μ_I can then be computed with

$$\mu_I = \mu_{I,\,\mathrm{ref}} \frac{I}{I_{\mathrm{ref}}} \frac{A}{A_{\mathrm{ref}}} (1 + {}^{\mathrm{ref}}\Delta), \tag{2.22}$$

where ${}^{\mathrm{ref}}\Delta$ is the differential hyperfine anomaly of an isotope with respect to a reference isotope. It can also be written with its two constituents

$${}^{\mathrm{ref}}\Delta = {}^{\mathrm{ref}}\Delta_{\mathrm{BW}} + {}^{\mathrm{ref}}\Delta_{\mathrm{BR}}. \tag{2.23}$$

${}^{\mathrm{ref}}\Delta_{\mathrm{BW}}$ and ${}^{\mathrm{ref}}\Delta_{\mathrm{BR}}$ denote the differential hyperfine anomalies arising from the Bohr-Weisskopf and the Breit-Rosenthal effect. They are defined as

$${}^{\mathrm{ref}}\Delta_{\mathrm{BW}} = \epsilon_{\mathrm{BW,\,ref}} - \epsilon_{\mathrm{BW}} \tag{2.24}$$

$${}^{\mathrm{ref}}\Delta_{\mathrm{BR}} = \epsilon_{\mathrm{BR,\,ref}} - \epsilon_{\mathrm{BR}} \tag{2.25}$$

The overall differential hyperfine anomaly can then be calculated with [90]

$$^{\mathrm{ref}}\Delta = \frac{A_{\mathrm{ref}}}{A}\frac{g_I}{g_{I,\,\mathrm{ref}}} - 1. \tag{2.26}$$

The Breit-Rosenthal effect is often assumed to be negligible compared to the Bohr-Weisskopf effect [35, 5] . It is hence considered that the hyperfine anomaly is caused only by the Bohr-Weisskopf effect and the distribution of the magnetisation in the nucleus. Two components $\epsilon_{\mathrm{BW},\pi}$ and $\epsilon_{\mathrm{BW},\nu}$ from protons and neutrons, respectively, contribute to the Bohr-Weisskopf effect. The contribution from the protons can be denoted as [42, 104]

$$\epsilon_{\mathrm{BW},\pi} \approx -\sum_{i=1}\left[\alpha_{\mathrm{S}\pi}b_{2i,\mathrm{S}}\langle R^{2i}\rangle_{\mathrm{S}\pi} + \alpha_{\mathrm{L}\pi}b_{2i,\mathrm{L}}\langle R^{2i}\rangle_{\mathrm{L}\pi} + \alpha_{\mathrm{S}\pi}(b_{2i,\mathrm{S}} - b_{2i,\mathrm{L}})\langle ZR^{2i}\rangle_{\mathrm{S}\pi}\right], \tag{2.27}$$

where $\alpha_{\mathrm{S}\pi}$ and $\alpha_{\mathrm{L}\pi}$ are the fractions of the magnetic dipole moment arising from the spin and the angular momentum of the protons. $Z = \sqrt{2\pi}[sY^{(2)}]^{(1)}/\langle s\rangle$ is the spin asymmetry operator with the spherical harmonics $Y^{(2)}$ and $\langle R^{2i}\rangle_{\mathrm{S},\pi}$ and $\langle R^{2i}\rangle_{\mathrm{L},\pi}$ are the expectation value of the even radial moments of the proton spin and angular distribution. The contribution of the neutrons to the Bohr-Weisskopf effect takes a similar form, although neutrons have zero charge and therefore no orbital angular momentum contribution:

$$\epsilon_{\mathrm{BW},\nu} \approx -\sum_{i=1}\left[\alpha_{\mathrm{S}\nu}b_{2i,\mathrm{S}}\langle R^{2i}\rangle_{\mathrm{S}\nu} + \alpha_{\mathrm{S}\nu}(b_{2i,\mathrm{S}} - b_{2i,\mathrm{L}})\langle ZR^{2i}\rangle_{\mathrm{S}\nu}\right]. \tag{2.28}$$

Consequently, the three fractions $\alpha_{\mathrm{S}\pi}$, $\alpha_{\mathrm{L}\pi}$ and $\alpha_{\mathrm{S}\nu}$ add to unity. The expansion of the electronic wave functions close to the nucleus yields the coefficients $b_{2i,\mathrm{S}}$ and $b_{2i,\mathrm{L}}$ with

$$\frac{\int_0^R fg\,\mathrm{d}r}{\int_0^\infty fg\,\mathrm{d}r} = \sum_{i=1} b_{2i,\mathrm{S}}R^{2i} \tag{2.29}$$

$$\frac{\int_0^R fg(1-r^3/R^3)\,\mathrm{d}r}{\int_0^\infty fg\,\mathrm{d}r} = \sum_{i=1} b_{2i,\mathrm{L}}R^{2i}, \tag{2.30}$$

where f and g denote the upper and lower radial components of the atomic wave functions and R is the radius in nuclear coordinates.

One possibility of precisely determining the differential HFA experimentally is the following. The hyperfine parameters A are first obtained under the assumption of a point-like nucleus neglecting the non-uniform magnetic field across the nucleus. This can be done, for example, using laser spectroscopy. Based on that, the magnetic dipole moments μ_I are determined, see Equation (2.18). Another technique that works with a uniform magnetic field across the nucleus and is therefore not sensitive to the distribution of nuclear magnetisation is then employed. An example for such a technique is β-NMR which allows to obtain μ_I directly, see Section 3.2. The difference in the ratio of the magnetic dipole moments will then yield the differential hyperfine anomaly Δ. This approach is pursued in Section 5.4.

3. Techniques

The principal technique deployed for the measurements in this thesis is β-detected nuclear magnetic resonance (β-NMR). It complements conventional nuclear magnetic resonance (NMR) and enables studies with far greater sensitivity by actively polarising the nuclear spin and utilising a highly efficient detection method. This chapter gives an introduction to the fundamental principles of NMR, followed by an explanation of the β-NMR technique.

3.1. NMR

NMR is a powerful tool that allows studying the properties of atoms and molecules. It relies on the interaction of nuclei with spin $I \neq 0$ with an external magnetic field B_0 [11, 93]. The technique is applied in a wide range of fields, including physics, chemistry, medicine, and material sciences [3, 62, 111].

All nuclei with $I \neq 0$ have a magnetic dipole moment μ_I. If such nuclei are exposed to a magnetic field, they interact with the field [105]. The Hamiltonian of the nuclei can then be expressed by

$$H = H_0 + H_\mathrm{M}, \tag{3.1}$$

where H_0 is the Hamiltonian of the unperturbed nucleus and H_M describes the perturbation due to the magnetic field. If a static magnetic field B_0 is applied, the Hamiltonian H_M is

$$H_\mathrm{M} = -\boldsymbol{\mu_I} \cdot \boldsymbol{B_0}. \tag{3.2}$$

Substituting the operator of the magnetic dipole moment

$$\boldsymbol{\mu_I} = g_I \mu_\mathrm{N} \boldsymbol{I}, \tag{3.3}$$

one obtains

$$H_\mathrm{M} = -g_I \mu_\mathrm{N} \boldsymbol{I} \cdot \boldsymbol{B_0} = -g_I \mu_\mathrm{N} I_z B_0, \tag{3.4}$$

if B_0 is applied along the z-axis [76, 1]. Here, $\mu_\mathrm{N} = e\hbar/(2m_\mathrm{p})$ is the nuclear magneton and $g_I = \mu_I/(I\mu_\mathrm{N})$ is the nuclear g-factor. Consequently, the state described with the nuclear spin I splits into $2I+1$ substates m_I taking values $m_I = -I, \ldots, I$. This is referred to as the Zeeman interaction or the Zeeman effect [6]. The difference in energy between these equidistant substates is

$$\Delta E = E(m_I) - E(m_I + 1) = |g_I| \mu_\mathrm{N} B_0. \tag{3.5}$$

In order to minimise the energy of the system, the nuclear spins align parallel or anti-parallel to the external magnetic field B_0, depending on the sign of μ_I. The population probability p_I of a substate m_I at thermal equilibrium is temperature-dependent and can be expressed with the Boltzmann distribution via

$$p_I = \frac{e^{-E(m_I)/k_\mathrm{B}T}}{\sum_{m_I} e^{-E(m_I)/k_\mathrm{B}T}}, \tag{3.6}$$

where k_B is the Boltzmann constant and T is the temperature. Therefore, the different states m_I have different populations. For example, for $I = 1/2$ and $\mu_I \neq 0$, the $m_I = 1/2$ state is more populated than $m_I = -1/2$.

The energy difference ΔE between the m_I substates, see Equation (3.5), can also be written as

$$\Delta E = |g_I|\mu_\mathrm{N} B_0 = \omega_0 \hbar = \nu_0 h, \tag{3.7}$$

where $\nu_0 = \omega_0/(2\pi)$ denotes the Larmor frequency of the nucleus. This frequency ν_0 can be thought of as describing the precession of the magnetic dipole moment μ_I around the z-direction of the magnetic field B_0.

When a second magnetic field B_1 oscillating at or close to the Larmor frequency ν_0 is applied orthogonal to B_0, transitions between the m_I substates are induced. It is hence possible to determine ν_0 by scanning the frequency of the applied B_1 field and measuring the electromagnetic wave emitted by the nuclei when they return to thermal equilibrium. Following Equation (3.7), determining the Larmor frequency ν_0 in a given magnetic field B_0 allows to derive the nuclear g-factor

$$|g_I| = \frac{\nu_0 h}{\mu_\mathrm{N} B_0}. \tag{3.8}$$

If the spin I of the nucleus is known, it is then possible to compute the magnetic dipole moment μ_I, see Equation (3.3), with

$$\mu_I = \frac{\nu_0 h I}{B_0}. \tag{3.9}$$

3.1.1. Free Induction Decay

Pulsed NMR, also known as Fourier Transform NMR, is the most commonly applied NMR technique today [6, 69]. It uses induction coils to transmit an oscillating magnetic field B_1 orthogonal to B_0 that excites the nuclear spins in the sample. Typically, this B_1 is a short pulse (in the order of a few µs) close to ν_0 that tips the spins away from the B_0 axis by $90°$ towards the axis of the B_1 field. Consequently, the ensemble of spins will then precess around B_1 at the Larmor frequency ν_0 before relaxing to the equilibrium condition, again aligning with B_0. Their precession produces a weak magnetic field that oscillates at the Larmor frequency ν_0, which induces a voltage oscillating at the same frequency in the coils previously used to excite the spins or in a separate pick-up coil. This signal is known as the Free Induction Decay (FID) [69].

The FID oscillates at the Larmor frequency ν_0, which is often in the range of hundreds of MHz. Rather than digitising the nuclear response directly via this high-frequency FID, an electronic circuit processes the analogue signal from the coil to provide a low-frequency output that can be digitised more conveniently. Quadrature detection is employed in order to distinguish between positive and negative frequencies [69]. The FID is first duplicated, after which one of the two outgoing signals is phase-shifted by $90°$. Frequency mixers are then used to obtain the differences between these signals and a reference frequency, typically the frequency used to excite the spins with the B_1 field. It is hence referred to as the carrier frequency ν_carrier. This processing allows to obtain two signals $a(t)$ and $b(t)$ with a phase shift of $90°$ that oscillate at a frequency

$$\nu = \nu_\mathrm{carrier} \pm \nu_0, \tag{3.10}$$

typically in the order of kHz. These signals $a(t)$ and $b(t)$ are then digitised. Figure 3.1 shows an example of such low-frequency signals and their phase shift.

The two components $a(t)$ and $b(t)$ are considered as the real part $\mathrm{Re}(f(t)) = a(t)$ and the imaginary part $\mathrm{Im}(f(t)) = b(t)$ of a complex signal $f(t) = a(t) + ib(t)$. In order to obtain the spectrum of this signal, $f(t)$ is taken as the input of the complex Fourier transform [76]

$$F(\nu) = \int_{-\infty}^{+\infty} f(t) e^{-i2\pi\nu t} \mathrm{d}t. \tag{3.11}$$

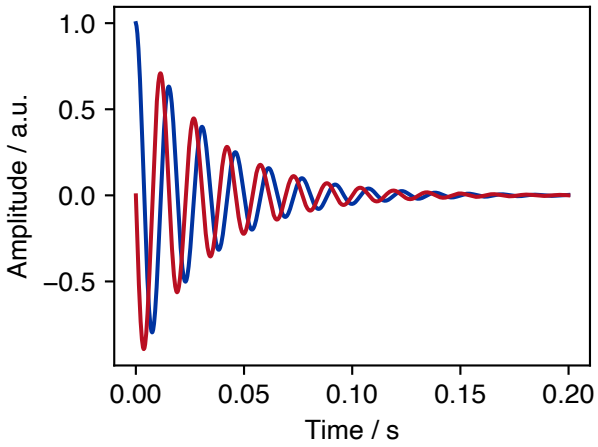

Figure 3.1.: The two components obtained from an FID after applying a $90°$ phase shift and frequency mixing.

An example of such a resulting spectrum is shown in Figure 3.2, based on the FID signal shown in Figure 3.1. A fit is then applied to the peak with Lorentzian line shape to obtain ν, which is used to determine the corresponding Larmor frequency ν_0 of the nuclei with Equation (3.10).

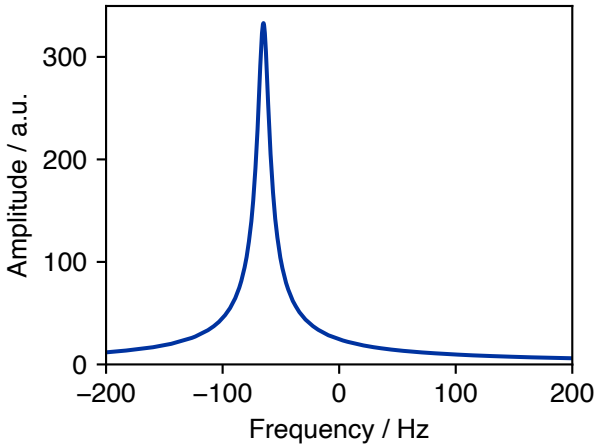

Figure 3.2.: The spectrum of the signal components shown in Figure 3.1, computed with a complex Fourier transform.

3.1.2. Relaxation times

For an ensemble of spins at thermal equilibrium, the population distribution of spin states can also be described as a net magnetisation parallel to B_0. When the spins relax after a $90°$ excitation, they return to thermal equilibrium through two different types of relaxation processes.

Spin-lattice (longitudinal) relaxation describes the recovery of net magnetisation parallel to the magnetic field B_0, characterised by the time constant T_1. The excess in energy dissipates into the environment in the form of photons or heat. Spin-spin (transversal) relaxation describes the recovery of the net magnetisation perpendicular to the magnetic field B_0, characterised by the time constant T_2. This arises due to differences in the precession frequency of the spins over time, leading to a loss of phase coherence. In Figure 3.2, the transversal relaxation of the signal can be observed as the exponential decay of the envelope of the signal.

3.1.3. Correction for magnetic susceptibility and NMR shielding

The magnetic field experienced by the nucleus is dependent on its environment. According to Equation (3.7), this also makes the Larmor frequency environment dependent. For example, the alkyl proton in methanol will resonate at a different frequency than the hydroxyl proton, due to the differences in nature and relative energies of their environment. This is termed NMR shielding and characterises the degree of shielding of B_0 relative to the bare nucleus [52, 51]. A correction needs to be applied to correct for this shielding σ [61, 64], which can be in the order of several hundred ppm [50]. In addition, B_0 and thus ν_0 are shifted due to the susceptibility of the sample. A material that is diamagnetic repels the magnetic field [6]. It is necessary to correct for this by considering the volume magnetic susceptibility κ and the geometry of the sample with respect to the magnetic field, reflected in the shape factor α. The susceptibility corrections are in the order of several parts-per-million (ppm). Both corrections combined allow obtaining the Larmor frequency ν_0 from the measured Larmor frequency ν_L via

$$\nu_0 = \frac{\nu_\mathrm{L}}{\left[1 + (1/3 - \alpha)\,\kappa\right](1 - \sigma)} \tag{3.12}$$

with the shape factor α characterising the geometry of the sample, the volume magnetic susceptibility κ and the NMR shielding σ of the environment of the nucleus.

3.1.4. Limitations of NMR

The most severe limitation of NMR is its relatively low sensitivity, mainly arising from two factors [76]. First, the detected signals arising from tipping the spins are relatively weak. Second, the polarisation, i.e. the difference in populations, of the nuclei is rather small. In the case of ^{1}H nuclei, the polarisation at thermal equilibrium is in the order of 10^{-5} to 10^{-4} [37]. One way of overcoming these limitations is via hyperpolarisation, which increases the polarisation above thermal equilibrium conditions [37]. Examples of this technique are Dynamic Nuclear Polarisation (DNP) [49, 91] or polarisation transfer with parahydrogen [34]. More information on hyperpolarisation can be found in [37]. Another approach to enhance the degree of polarisation is optical pumping [46], which is introduced in more detail in the next section.

3.2. β-NMR

β-detected NMR (β-NMR) offers a sensitivity that is multiple orders of magnitude greater than in conventional NMR [71, 62]. It tackles the two principal issues of low polarisation and inefficient detection by combining hyperpolarisation and detection via decay radiation. The β-NMR approach presented here uses optical pumping to achieve a hyperpolarisation of the nuclei before they are implanted into a sample, resulting in degrees of polarisation ranging often between $10\,\%$ and $80\,\%$ [72, 100, 89]. The signal detection works via decay radiation: When spin-polarised radioactive nuclei decay, the emitted β particles exhibit an asymmetry [116]. β-NMR exploits this phenomenon by observing the change in the β decay asymmetry of short-lived nuclei depending on the frequency ν of the applied B_1 field [106, 47], with a decrease in asymmetry at $\nu = \nu_\mathrm{L}$. β-NMR allows for a variety of measurements, such as the determination of magnetic dipole moments of radioactive nuclei with ppm precision [84, 50]. This section explains the method of optical pumping, the β decay asymmetry and its detection.

3.2.1. Optical pumping and nuclear spin polarisation

One way of obtaining a hyperpolarisation of an ensemble of nuclear spins I is optical pumping, a technique that uses circularly polarised laser light to induce transitions between the m_F substates (Zeeman substates) of the hyperfine structure, see Section 2.3.2.

A laser needs to be brought into resonance with the optical transition of interest. In the work presented here, this is done by first tuning the laser close to the required frequency, followed by accelerating or decelerating the ion beam, which results in the beam perceiving a laser frequency ν_{per} that is different to the set laser frequency ν_{las} due to the Doppler effect. An electrostatic potential is used to alter the velocity and thus tune ν_{per} until the resonance condition is met, referred to as 'Doppler tuning'. The perceived frequency ν_{per} can be calculated through

$$\nu_{\mathrm{per}} = \nu_{\mathrm{las}}\sqrt{\frac{1-\beta}{1+\beta}} \text{ with } \beta = \sqrt{1 - \frac{m^2c^4}{(eU+mc^2)^2}}, \tag{3.13}$$

where ν_{las} is the laser frequency, U is the total acceleration voltage and m is the mass of the ion. This method is widely used in laser spectroscopy to conveniently tune the transition of interest into resonance with the laser light [117].

Allowed transitions from a lower state F to a higher state F' follow the transition rule $\Delta F = 0, \pm 1$, with the exception of $F = 0 \rightarrow F' = 0$ not being allowed. The laser light used for optical pumping is circularly polarised (σ^+ or σ^-), which means the additional transition rule $\Delta m_F = \pm 1$ arises for $\sigma^\pm$ polarisation. Once excited, the atom relaxes to a lower state via a spontaneous decay with $\Delta m_F = 0, \pm 1$. It is thus possible to transfer angular momentum from the photons to the atoms. The excitation/de-excitation cycles repeat numerous times, eventually resulting in $m_F = F$ obtaining the highest population for σ^+ polarisation or $m_F = -F$ for σ^- polarisation.

Figure 3.3 shows an optical pumping scheme for $^2S_{1/2} \rightarrow {}^2P_{3/2}$ (D_2 line) for an atom with nuclear spin $I = 1/2$, such as ^{47}K. The transition is excited with σ^+ polarised light, following the transition rule $\Delta m_F = +1$ and eventually leading to the highest population of the $m_F = 1$ substate.

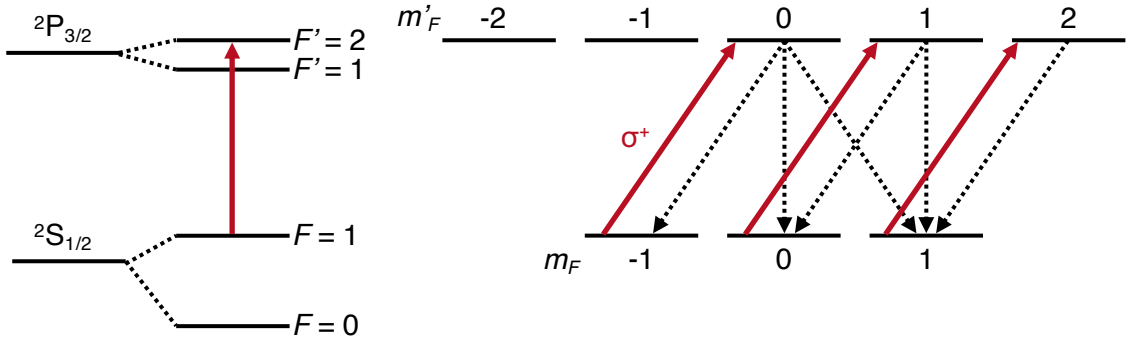

Figure 3.3.: Optical pumping scheme for $I = 1/2$ with the transition $F = 1 \rightarrow F' = 2$ and σ^+ polarised light (according to the selection rule $\Delta m_F = +1$). This corresponds e.g. to the D_2 line of ^{47}K ($3p^6 4s\ {}^2S_{1/2} \rightarrow 3p^6 4p\ {}^2P_{3/2}$).

Optical pumping leads to an imbalance in the population of the m_F states and thus causes a polarisation of the atom, whereas β-NMR requires a polarisation of the nuclear spin I. However, the polarisation of F has already resulted in a polarisation of I and J due to the hyperfine interaction. The spins I of the nucleus and J of the electron now get decoupled while maintaining the nuclear spin polarisation P_I. This is achieved by gradually increasing the magnetic field, causing the atoms to move from the Zeeman regime to the Paschen-Back regime. At this point, the description of the substates with the quantum number m_F becomes

invalid. Instead, an asymptotic conversion into the corresponding substates characterised by m_I and m_J takes place, with these quantum numbers becoming the correct description [1]. An example of the level splitting of the hyperfine structure undergoing the transition from the Zeeman regime to the Paschen-Back regime is shown in Figure 3.4 for the $^2S_{1/2}$ state of an atom with $I = 1/2$. The splitting in this figure is computed with the Breit-Rabi formula [24, 103].

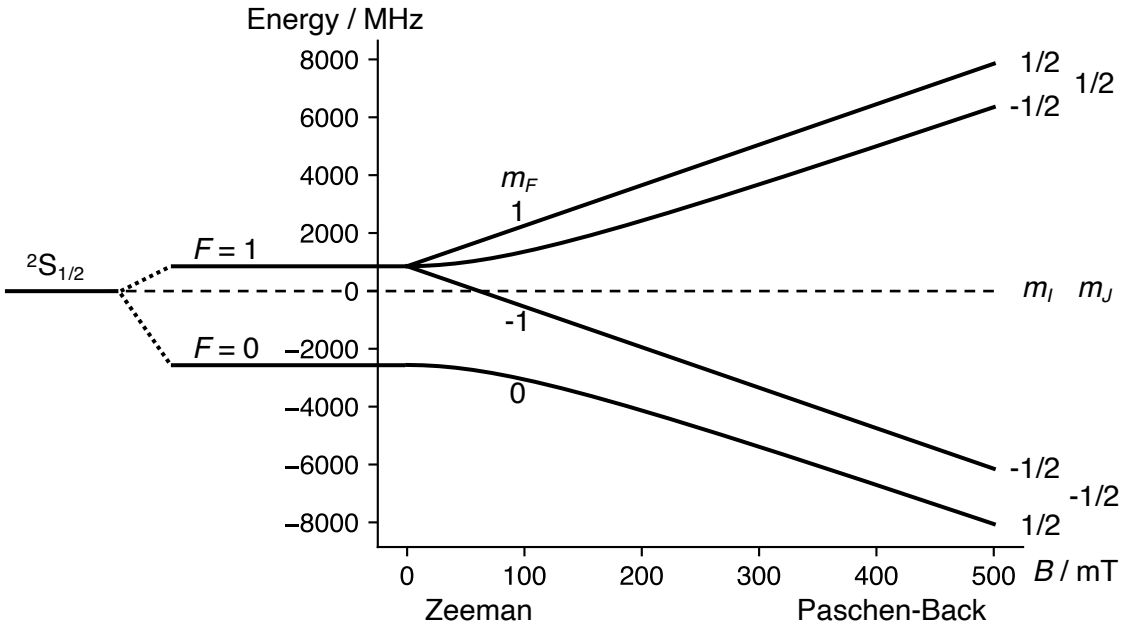

Figure 3.4.: The hyperfine structure of the $^2S_{1/2}$ state of an atom with spin $I = 1/2$, here ^{47}K with its splitting into Zeeman levels in weak magnetic fields and the transition to the Paschen-Back regime in strong magnetic fields.

3.2.2. β decay asymmetry and detection

Spin-polarised radioactive nuclei exhibit an asymmetry in their β decay due to the violation of parity conservation in the weak force [116]. The angular distribution of these particles is given by

$$W_\beta(\theta) = 1 + A_\beta \frac{v}{c} P_I \cos(\theta), \tag{3.14}$$

where v is the velocity of the β particle, c is the speed of light, P_I is the degree of nuclear spin polarisation and A_β is the asymmetry parameter. The angle θ is given with respect to the polarisation axis at $0°$ [109]. As seen in this equation, the exhibited asymmetry $W_\beta(\theta)$ is directly proportional to the polarisation P_I. The asymmetry parameters a_β of the different transitions depend on the difference $\Delta I = I_{\text{fin}} - I_{\text{ini}}$ of the spin I_{ini} of the parent nucleus and I_{fin} of the daughter nucleus. It is possible to compute a_β of the individual transitions with

$$a_\beta = \begin{cases} -1 & \text{for } \Delta I = -1 \\ I_{\text{ini}}/(I_{\text{ini}}+1) & \text{for } \Delta I = +1 \\ -1/(I_{\text{ini}}+1) & \text{for } \Delta I = 0 \text{ (Gamow-Teller transition)} \\ 0 & \text{for } \Delta I = 0 \text{ (Fermi transition).} \end{cases} \tag{3.15}$$

The overall asymmetry parameter A_β is the average of the individual a_β weighed with the branching ratios of the corresponding transitions [74].

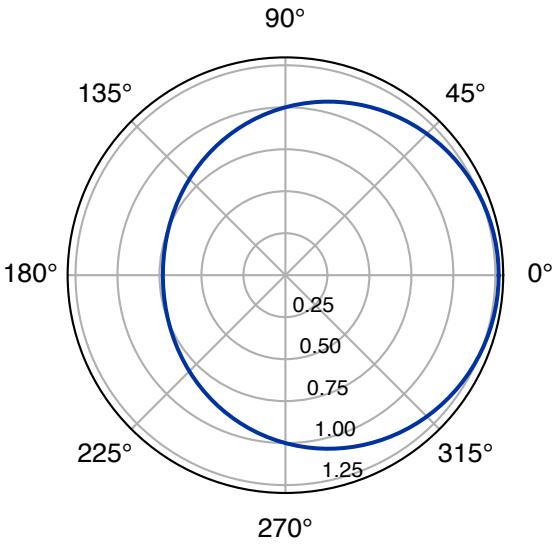

Figure 3.5.: The angular distribution of the emitted β particles, shown with arbitrary values of $a_\beta = 90\,\%$ and $P_I = 30\,\%$. The polarisation axis of the nuclear spins is along $0°/180°$.

An example of an angular distribution of β particles is shown in Figure 3.5 for $A_\beta = 90\,\%$ and $P_I = 30\,\%$. As seen here, the largest asymmetry is present at $\theta = 0°$ and $\theta = 180°$, i.e. on the polarisation axis of the nuclear spins. Typically, a pair of two β detectors is therefore located at these positions to determine the normalised experimental β decay asymmetry A_{exp} with

$$A_{\text{exp}}(\theta_1, \theta_2) = \frac{N_1(\theta_1) - N_2(\theta_2)}{N_1(\theta_1) + N_2(\theta_2)}, \tag{3.16}$$

where $N_1(\theta_1)$ and $N_2(\theta_2)$ are the number of β events in two detectors located at angles θ_1 and θ_2.

The β decay asymmetry changes after the ensemble of nuclei has been implanted into the host in a magnetic field B_0 due to the longitudinal relaxation with time constant T_1. It is hence possible to denote

$$W_\beta(\theta, t) = 1 + A_\beta \frac{v}{c} P_I(0) e^{-t/T_1} \cos(\theta) \tag{3.17}$$

for the change in β asymmetry under relaxation.

To conduct the β-NMR measurements, an oscillating magnetic field B_1 is applied orthogonal to B_0, just like in conventional NMR. When B_1 is close to or at the Larmor frequency ν_0 of the nuclei, transitions between the m_I substates are induced and the polarisation P_I diminishes. This results in the exhibited β decay asymmetry becoming isotropic again, see Equation (3.14), giving rise to efficient detection of the Larmor frequency.

4. Experimental setup

This chapter introduces the facility and the setup where the experiments presented in this thesis took place. It gives an overview on CERN in Section 4.1, its radioactive ion beam facility ISOLDE in Section 4.2 and the VITO beamline in Section 4.3. The subsequent Section 4.4 presents the basic working principles of the data acquisition system at VITO.

4.1. CERN

The European Organization for Nuclear Research (CERN) is located on the Swiss-French boarder in Geneva. Its accelerator complex, see Figure 4.1, starts with Linac4, a linear accelerator which accelerates H^- to an energy of $160\,\mathrm{MeV}$. These ions are then stripped of their electrons, leaving a beam of H^+, i.e. protons, for the injection into the Proton Synchrotron Booster (PSB) [114], which consists of four synchrotron rings with a diameter of $50\,\mathrm{m}$ that accelerate the proton bunches every $1.2\,\mathrm{s}$ to energies of up to $2\,\mathrm{GeV}$. The proton bunches are organised in a sequence, the so-called super-cycle, with their intensity and destination depending on the requests from the different experiments and facilities at CERN. This super-cycle is repeated periodically until a change is asked for by one of the receivers of the proton bunches. It has no fixed length but typically contains 20 to 40 proton bunches. The PSB is part of the injection complex of the Large Hadron Collider (LHC) via the Proton Synchrotron (PS) and the Super Proton Synchrotron (SPS). ISOLDE is the only facility connected directly to the PSB.

4.2. ISOLDE

ISOLDE (Isotope Separator On-Line Device) is CERN's facility to produce radioactive ion beams (RIBs), providing users with more than 1300 isotopes from 76 elements [16, 99]. Since its beginnings in 1967, it has undergone several major upgrades and extensions [75, 65, 17]. Nowadays, its main features include two target stations and mass separators and a radio-frequency quadrupole cooler buncher delivering low-energy beams of up to $60\,\mathrm{keV}$. A subsequent post-accelerator can accelerate the produced isotopes to energies of up to $10\,\mathrm{MeV/u}$ and provide them to three HIE-ISOLDE beamlines (High Intensity and Energy ISOLDE). They study interactions of the beam with a fixed sample to gain information on the nuclear structure by reactions [27, 16]. The layout of ISOLDE including some of its infrastructure is depicted in Figure 4.2. All experiments described in this thesis took place at the VITO beamline, explained in detail in the next Section 4.3, which is located in the centre of the ISOLDE hall.

The facility receives proton bunches from the PSB with an energy of $1.4\,\mathrm{GeV}$, a duration of $2.4\,\mu\mathrm{s}$ and an intensity of up to $3.3 \times 10^{13}\,\mathrm{protons/bunch}$. They arrive in intervals of $1.2\,\mathrm{s}$ or multiples thereof, though the average proton current is limited to $2\,\mu\mathrm{A}$ due to radiation restrictions [75, 28]. ISOLDE takes the majority of protons accelerated at CERN [29].

Two target stations and separators are available to produce the short-lived nuclei: the General Purpose Separator (GPS) and the High Resolution Separator (HRS). When the proton beam impinges one of the thick targets, it induces fission, spallation and fragmentation, which generate a wide range of isotopes. Different

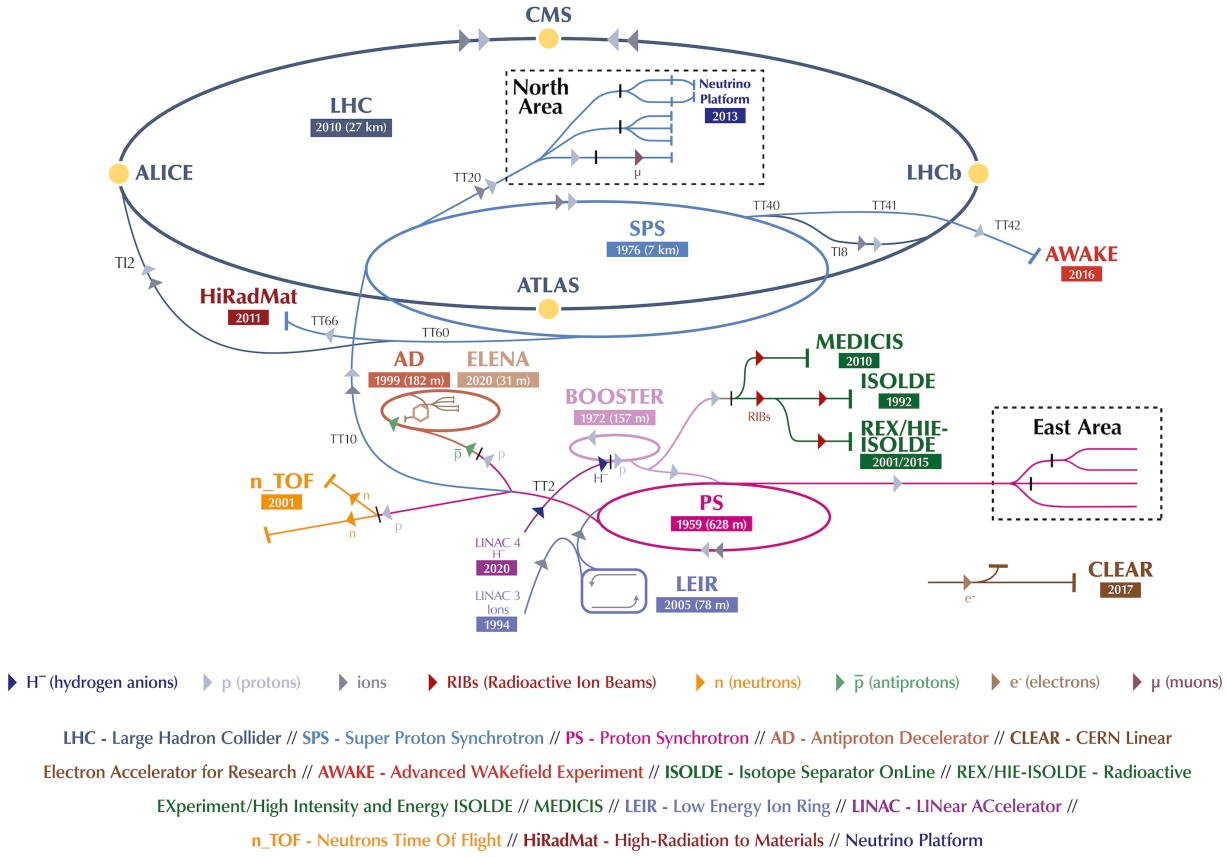

Figure 4.1.: The CERN accelerator complex with Linac4 injecting protons into the PSB which are then accelerated to an energy of $1.4\,\mathrm{GeV}$ and provided to, among others, ISOLDE [77].

target materials, such as tantalum, titanium and uranium carbide (UC_x), benefit particular nuclear reactions and thus enhance the yields of certain isotopes. Currents between $600\,\mathrm{A}$ and $800\,\mathrm{A}$ heat the targets to temperatures in the order of $1000\,^{\circ}\mathrm{C}$ to $2000\,^{\circ}\mathrm{C}$ [16]. The isotopes then diffuse and effuse out of the target [99]. Depending on the isotope of interest, the extraction line can be heated or cooled to minimise or maximise adsorption which can be utilised to e.g. purify beams of noble gases or volatile molecules [16].

In order to accelerate the isotopes towards the experimental setups, it is necessary to ionise them. Atoms with low work function, such as the alkali metals sodium or potassium, get surface ionised upon contact with the hot target or the extraction line. A dedicated tungsten cavity brought to temperatures in the order of $2300\,^{\circ}\mathrm{C}$ is also available for surface ionisation [39]. Plasma sources are used for elements with higher work function, e.g. noble gases. In all other cases, the Resonant Ionisation Laser Ion Source (RILIS) is available to ionise the element of choice through multi-step excitations with pulsed lasers. Due to the difference in energy levels between different isotopes, this method is highly selective and provides the user with comparably pure isotope beams [98, 39]. Both, target material and the method of ionisation, hence influence the yields and the purity of the beam and are therefore chosen with respect to the isotope of interest [99]. Users can check the availability and expected production rates of the isotopes with the ideal target type and ionisation method in an on-line database [4].

An electrostatic potential of up to $60\,\mathrm{kV}$ extracts the ions from the source and accelerates them towards the respective separators. The separators use dipole magnets to filter the isotopes by their mass-to-charge ratio A/q, where the charge q of the ions is quantised and typically 1 or maximum 2. GPS comprises a single

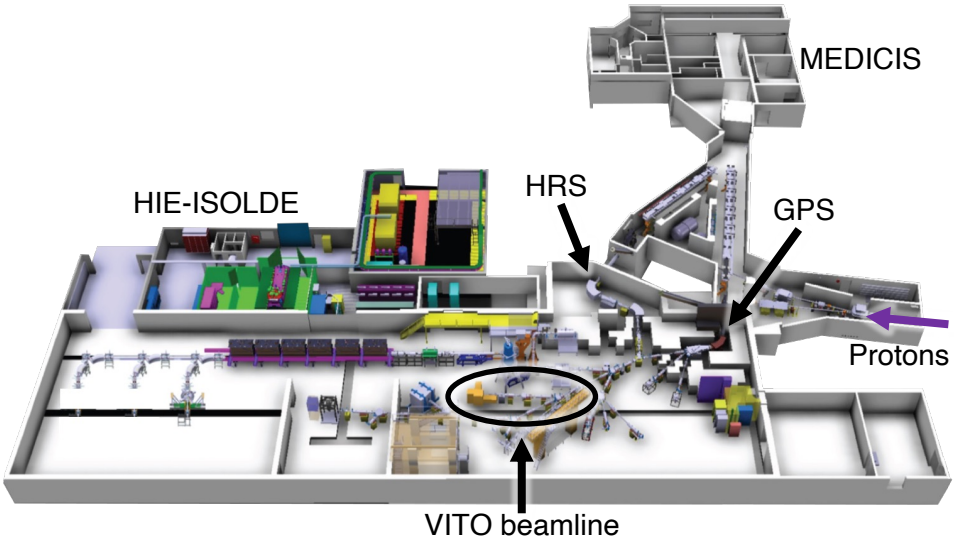

Figure 4.2.: The ISOLDE facility at CERN with the proton beam entering ISOLDE from the right, the two separators GPS and HRS as well as the VITO beamline in the centre of the hall. HIE-ISOLDE for high intensity and energy experiments is in the left part and the MEDICIS facility is in the background. For an explanation of all labelled features, see text. Illustration based on [60].

H-type magnet, bending the beam by $70°$ at a radius of $1.5\,\mathrm{m}$ with a mass resolution of $m/\Delta m \approx 800$. This separator can also provide users with nuclei $13\,\%$ lighter or heavier than the set mass A in two beamlines used for collections, referred to as GLM for lower masses and GHM for higher masses. HRS, on the other hand, has two $90°$ and $60°$ C-type magnets with a radius of $1\,\mathrm{m}$ to achieve a higher mass resolution of $m/\Delta m \approx 6000$ [28].

The beam from HRS is then fed into ISCOOL, ISOLDE's radio-frequency quadrupole cooler buncher (RFQ), to reduce the emittance and the energy spread of the beam [41]. Spatial constraints did not allow for the installation of an RFQ at GPS. ISCOOL is a linear Paul trap that uses helium at a pressure of $0.1\,\mathrm{mbar}$ as a buffer gas to cool the beam and quadrupolar, oscillating electric fields to confine it radially. A differential pumping system is in place to keep all other beamlines at pressures in the order of $10^{-6}\,\mathrm{mbar}$. It is also possible to use ISCOOL for bunching [28]. In this mode, it creates potential well that keeps the ions trapped until the users pull down a potential to release the beam towards their setup. This is especially useful for laser spectroscopy to reduce the energy spread and suppress the background. More information on this can be found in [78]. Bunching the beam is also beneficial when it comes to the acquisition of relaxation times, see Section 3.1.2. It ensures that all of the beam is implanted into the sample at the same time, thus guaranteeing a simultaneous start of the relaxation in order to see the shortest possible components of relaxation in the recorded data.

Electrostatic potentials eventually guide the ion beams to the experimental setups across the hall. ISOLDE also allows for travelling setups to be installed for measurement campaigns. It is planned to upgrade the facility in order to receive proton beams with higher intensities and energies of up to $2\,\mathrm{GeV}$ to enhance the isotope production [43]. All in all, ISOLDE contributes profoundly to wide fields of research with dedicated beamlines for laser spectroscopy, nuclear and atomic physics, solid-state physics, medical research and material sciences [17, 18].

It is also worth noting that only a fraction of the protons received by ISOLDE actually interacts with the targets [28]. To make use of the remainder of protons, the MEDICIS facility (Medical Isotopes Collected from ISOLDE) was founded, which places additional thick targets behind ISOLDE's GPS and HRS targets to produce radioisotopes for medical research [33].

4.3. β-NMR beamline

The VITO (Versatile Ion-Polarisation Techniques On-Line) beamline at ISOLDE is devoted to experiments with spin-polarised beams of short-lived radioactive nuclei [106, 71, 45, 30, 63]. Its prime focus is research in the fields of atomic and nuclear physics, material sciences and biochemistry where it employs highly-sensitive β-NMR [73, 70, 67, 68, 10, 94].

This section first introduces the different parts of the beamline and their working principle. The components around the sample and the detection system are then explained in greater detail, with an additional section focussing on the hardware of the NMR measurements. Subsequently, it is described how to record hyperfine spectra, relaxation curves and β-NMR resonances. A rendering of the setup depicted in Figure 4.3.

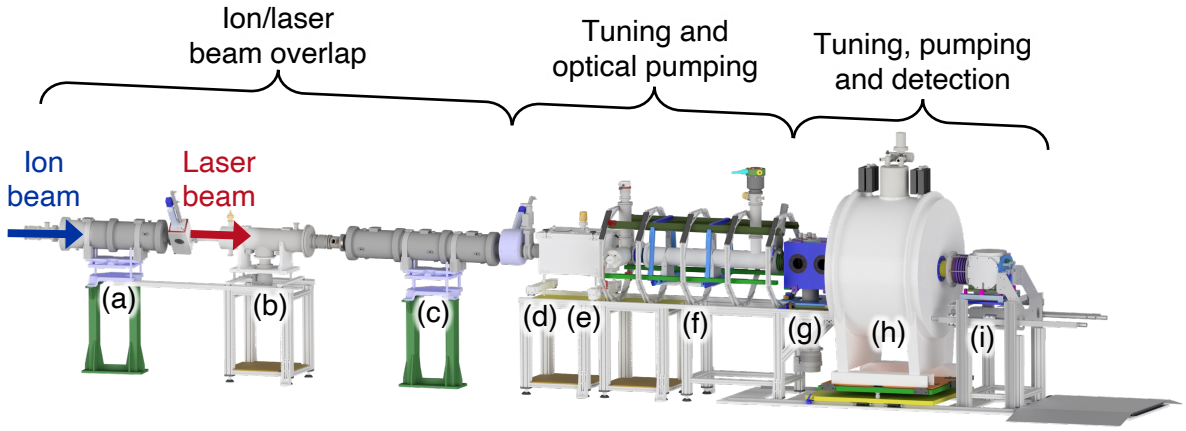

Figure 4.3.: Overview on the VITO beamline at ISOLDE: (a) quadrupole doublet, (b) $5°$ bender, (c) quadrupole triplet, (d) Doppler tuning electrodes, (e) charge exchange cell, (f) optical pumping section, (g) front detector chamber, (h) superconducting magnet and (i) sample loading chamber. The blue and red arrows indicate the positions where the ion beam and the laser beam enter the setup.

4.3.1. Beamline overview

Overlap of ion and laser beam

The radioactive ion beam provided by ISOLDE enters the VITO beamline through a quadrupole doublet, (a) in Figure 4.3, which is used to focus and defocus the beam. It is followed by a chamber with a Faraday cup and a wire scanner to check the beam current and its profile while tuning it towards the sample. The next element (b) is a $5°$ bender which, as the name suggests, bends the beam by $5°$. At this stage, the laser light is coupled into the setup through a port and tuned to achieve a collinear overlap with the beam further down the setup for optical pumping. A quadrupole triplet (c) is followed by another Faraday cup and wire scanner to aid focussing and steering the beam during the initial set-up [63].

Doppler tuning and neutralisation

In order to establish optical pumping, the selected optical transition of the chosen isotope needs to be in resonance with the laser light. A crucial element to establish such conditions is a pair of electrodes that accelerate and decelerate the ion beam, as described in Section 3.2.1. These two so-called Doppler electrodes (d) are located in the charge exchange chamber. They are oriented collinearly around the ion beam at a length of circa $200\,\mathrm{mm}$, with a crown-shaped electrode on the inside and a mesh-like electrode on the outside. A potential is applied to the Doppler electrodes that changes the energy of the ion beam by up to $\pm 1\,\mathrm{keV}$ to

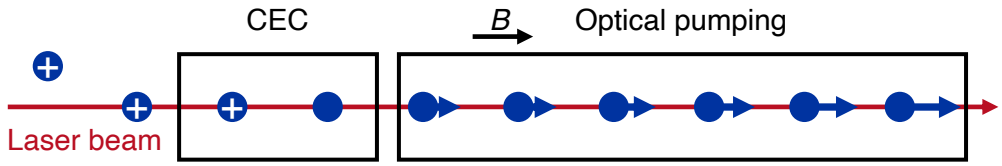

Figure 4.4.: The laser beam is coupled into the beamline in the $5°$ bender and brought to a collinear overlap with the ion beam. The ions are then neutralised in the charge exchange cell. Repeated excitation/de-excitation cycles in the optical pumping section result in an increasing polarisation of the atomic spin F, shown with the increasing length of the arrows.

tune the beam into resonance with the laser light. More information on their design and testing can be found in [45].

When beams of alkali metals are used, it is beneficial for optical pumping to have an atom beam rather than an ion beam because the transitions of their single valence electron are more accessible with the available lasers. A charge exchange cell (CEC) can be used to neutralise the ion beam (e). It is a cylinder attached to a $20\,\mathrm{mm}$-diameter tube through which the ion beam passes on its way to the sample. The CEC is filled with an alkali metal, such as sodium or potassium, and six heating rods bring it to temperatures of e.g. $200\,°\mathrm{C}$ for sodium and $150\,°\mathrm{C}$ for potassium to liquefy and vaporise the alkali. When the radioactive ion beam passes through the vapour, it collides with the gaseous alkali atoms, retrieves its missing electrons and is thus neutralised. The arms of the cell are heated, too, albeit to lower temperatures of $100\,°\mathrm{C}$ and $75\,°\mathrm{C}$ for sodium and potassium, respectively, allowing the alkali to liquefy and flow back into the cylinder to be vaporised again. More information on the design and implementation of the CEC can be found in [45] and [30].

Optical pumping

The atom beam subsequently enters the optical pumping section (f). At this stage, it is collinearly overlapping and in resonance with the laser beam, enabling optical pumping. A length of $2\,\mathrm{m}$ for this interaction section ensures that numerous excitation/de-excitation cycles occur to maximise the polarisation of the atoms, cf. Section 3.2.1. Helmholtz coils are positioned around this area. They induce a magnetic field in the order of $2\,\mathrm{mT}$ in the direction of the beam propagation to provide a quantisation axis for the orientation of the spins. The coils also shield the section from magnetic fields of neighbouring setups. A schematic of the $5°$ bender, the CEC and the optical pumping section is shown in Figure 4.4.

Superconducting magnet and spin decoupling

The polarised beam then passes through the chamber (g) housing the front detector. Here, the guiding field is surpassed by the increasing component of the $4.7\,\mathrm{T}$ field of the superconducting magnet (h). As explained in Section 3.2.1, the transition of the beam from the Zeeman regime in the weak magnetic field of the optical pumping section to the Paschen-Back regime in the strong field decouples the atomic spin F into the nuclear spin I and the electron angular momentum J.

The Bruker 47/16 superconducting magnet is a solenoid oriented along the beam axis with a bore of $160\,\mathrm{mm}$ in diameter and houses the last part of the beamline with the sample in its centre. It offers a field strength of $4.7\,\mathrm{T}$, equivalent to a proton Larmor frequency of $\approx 200\,\mathrm{MHz}$. Passive shimming enhances the field homogeneity to a sub-ppm level across the measurement volume. A field map acquired after the shimming process indicates deviations of less than $0.8\,\mathrm{ppm}$ in a sphere of $30\,\mathrm{mm}$ radius around the sample. The measurements show a temporal drifts of the field below $0.06\,\mathrm{ppm/h}$. The high homogeneity and stability result in a magnetic field that is effectively constant over the entire sample volume during a measurement campaign, and thus contribute to narrower resonances and improve the resolution of the β-NMR spectra.

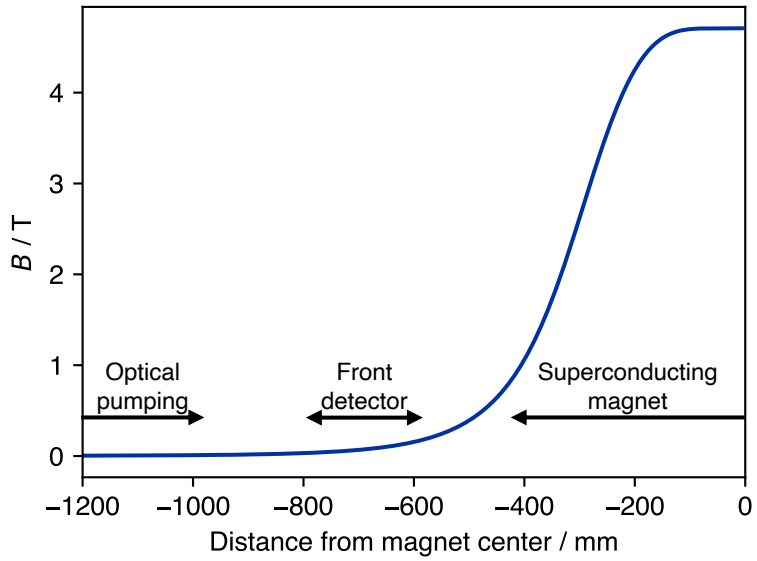

Figure 4.5.: The overall magnetic field B on the beam axis, comprising the guiding field of the Helmholtz coils in the optical pumping section and the field of the 4.7 T superconducting magnet. The positions of the optical pumping section, the front β detector and the superconducting magnet are indicated as well.

In addition, the magnet is equipped with active shielding to diminish its stray field. More details on the magnet specifications can be found in [63]. The overall magnetic field on the beam axis is shown in Figure 4.5. Indicated is the position of the optical pumping section and the front detector, explained below.

Sample carriage

To make sure the components located in the magnet, e.g. the sample and a reference probe, are easily accessible, they are mounted on an aluminium plate, referred to as 'sample carriage', see (a) in Figure 4.6. The plate offers equidistant threaded holes every $25\,\mathrm{mm}$ across its entire surface to allow for a flexible arrangement of the equipment, thus keeping the system modular for future changes. It is equipped with conical pins (b) on one side, whose counterparts are rigidly integrated in the beamline. An aluminium profile connects the carriage to the rear flange at the end of the beamline (cf. (i) in Figure 4.3). This entire assembly rests on rails and can therefore be moved out of the magnet to make the components on the sample carriage available. When the system is moved back into the magnet, the rear flange closes the beamline and the conical pins align the sample carriage with the rest of the setup, ensuring a fast and reproducible positioning of all components with respect to each other and the polarised beam.

Measurement equipment around the sample

The central component located on the sample carriage is the sample, (c) in Figure 4.6. It is attached to a sample holder, which fits in a support structure (illustrated in blue). Rather than gluing the holders to the support structure, they are held in place by a tight fit, which allows for easy sample changes and ensures a highly reproducible alignment. Two types of samples are generally used at the setup. The first is crystals which can simply be glued to one of the holders. Figure 4.6 shows the setup for the second type, liquids. Sheets of mica (red) with a diameter of $8\,\mathrm{mm}$ and a thickness of less than $1\,\mathrm{mm}$ are attached to the holder at an angle of $45°$, leaning towards the beam axis, to keep a liquid droplet in position. This system is advantageous for sample changes: Rather than cleaning the holder in place to prepare for the next liquid sample, the entire holder with the mica can be replaced and cleaned outside the setup while the subsequent measurement is

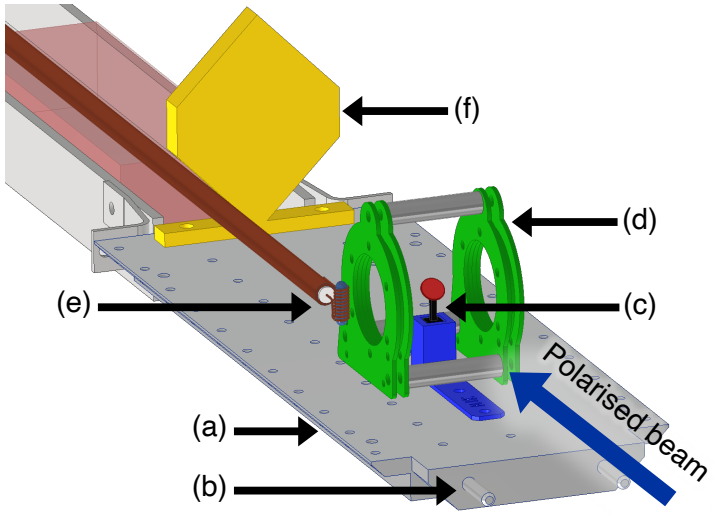

Figure 4.6.: Schematic of the sample carriage and its elements around it: (a) aluminium breadboard, (b) conical pins for alignment, (c) sample holder (black and blue) with sample (red), (d) rf coil, (e) ^{2}H reference probe and (f) rear β detector. The polarised beam travels along the magnetic field axis from the bottom right and is implanted into sample. See text for details on the displayed components.

already running with the next sample on a different holder. The exchangeable samples are also advantageous during the initial set-up when the beam is tuned onto the sample using stable isotopes, such as ^{23}Na or ^{39}K. A copper disc with the same orientation and dimensions as the mica sheets is then installed in the holder to read out the beam current at the sample position, while an additional copper plate is mounted behind it to read out the current of the beam missing the sample. The beam is then tuned by maximising the current on the copper sample while minimising the current on the plate behind it.

A set of $30\,\mathrm{mm}$ Helmholtz coils (d) wound on a glass support structure is centred around the sample. The coils provide the signal to excite the spins of the radioactive probe nuclei, see Section 3.1. To precisely determine the magnetic field B_0 at the time of the measurement, a ^{2}H reference probe (e) performing pulsed NMR is located at the same height as the sample, $25\,\mathrm{mm}$ to its side. These two components are explained more detailed in Section 4.3.2.

β detection

The last crucial component mounted on the sample carriage is a β particle detector, cf. (f) in Figure 4.6. It is one of the two detectors to acquire the asymmetry in the β particle emission from the sample, one being located in front of the sample at a position of $0°$ and one behind it at $180°$, see Figure 3.5. This rear detector, located $170\,\mathrm{mm}$ behind the sample, is made from $10\,\mathrm{mm}$-thick EJ-200 plastic scintillator in the dimensions $50\,\mathrm{mm}$ by $50\,\mathrm{mm}$. Two Onsemi 60035 silicon photomultipliers (SiPMs) are attached to opposite corners of the scintillator [86, 63]. Because SiPMs are not affected by magnetic fields, the detector can be located inside the superconducting magnet without the use of light guides. To prevent any background from the laser used for optical pumping, the entire detector is wrapped in $50\,\mu\mathrm{m}$-thick aluminised Mylar. The SiPMs are surface mounted on printed circuit boards (PCBs), each of them connected to an operational amplifier (Texas Instruments OPA656) to amplify the signal and allow for individual gain adjustment. A breakout board distributes the wires to the SiPM boards and allows for a bundled connection to the vacuum feedthroughs. The signals are summed and fed into a single channel of the data acquisition system, see Section 4.4.

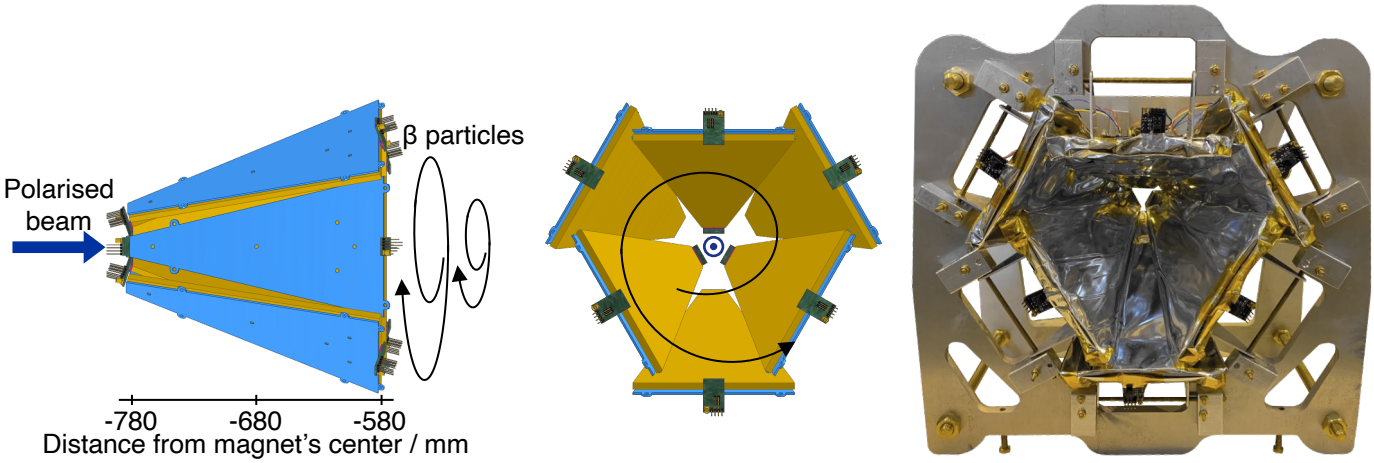

(a) Side view. (b) Front view. (c) Front view, assembled detector.

Figure 4.7.: The front β detector seen (a) from the side with the polarised beam passing through the aperture of the detector towards the sample and the β particles following their helical trajectories in the opposite direction. (b) shows an axial view with the polarised beam coming out of the plane and the β particles spiralling into the plane towards the detector. The assembled detector in its support structure is depicted in (c) with the aperture in the centre. Some of the SiPMs and the Mylar wrapping are visible.

The front detector is located on the other side of the sample with respect to the rear detector. Its design had to take into account two aspects. Due to its position in front of the sample on the beam axis, an aperture is required in its centre to let the polarised beam pass towards the sample. Another important point are the trajectories of the β particles in the magnetic field. The Lorentz force acts on the β particles and diverts them onto helical trajectories whose gyro-radii depend on their energy, their initial angle of emission and the magnetic field at their position. A small emission angle and/or a low energy of the particles result in smaller gyro-radii which could result in their loss through the aperture of the detector. This and the fact that particles emitted close to the beam axis exhibit the highest β decay anisotropy, as shown in Section 3.2.2, speak in favour of a small aperture. On the other hand, the aperture needs to be large enough to avoid an implantation of the radioactive beam into the detector which would inevitably influence the measured asymmetry. If the emission angles and energies of the particles are too high, they can be lost upon impact at the wall of the vacuum chamber before they reach the detector.

Taking this into account, the final implementation of the front detector consists of six trapezoidal scintillators oriented as a funnel, whose larger opening faces the sample. An illustration of the design is shown in Figure 4.7 along with a photo of the assembled detector in its surrounding support structure. This arrangement of scintillators forms an aperture of about $30\,\mathrm{mm}$ in diameter for the beam to pass, whereas on the other side the diameter is around $160\,\mathrm{mm}$. It is located outside the superconducting magnet in the chamber annotated (g) in Figure 4.3 at a distance of $580\,\mathrm{mm}$ to $780\,\mathrm{mm}$ to the sample in a magnetic field of less than $200\,\mathrm{mT}$. The six detector segments follow the same design as the rear detector, being made from EJ-200 with two Onsemi 60035 photomultipliers on opposite sides and aluminised Mylar wrapping. To feed the signals of the front detector into the data acquisition system, the outputs of two scintillators located opposite to each other are summed, resulting in three input channels covering the front detector. More information on the detector setup is provided in [63].

Laser system

Circularly-polarised light is required for optical pumping, see Section 3.2.1. To obtain this, a MATISSE Ti:sapphire tunable ring laser is used to provide laser light of the required wave length to induce the optical transition. A beam splitter linearly polarises the laser beam, followed by a $\lambda/4$ plate to achieve a circular polarisation before the laser beam is coupled into the beamline through a quartz window. It is possible to focus the laser beam with a set of lenses acting as a telescope in order to maximise the overlap between the laser beam and the isotope beam in the optical pumping section.

4.3.2. NMR hardware

β-NMR

For the β-NMR studies, a magnetic field B_1 needs to be induced to excite the spins of the radioactive probe nuclei, see Section 3.1. A Rohde & Schwarz SMY01 rf generator provides a signal of frequency ν that is amplified by an ENI 240L broadband amplifier with a maximum output of $40\,\mathrm{W}$ [38]. This signal is then used to induce the B_1 field with a pair of Helmholtz coils, see (d) in Figure 4.6. The coils are wound around a glass support structure and have a diameter of $30\,\mathrm{mm}$.

^{2}H reference probe

With the Larmor frequency ν_0 being dependent on the magnetic field B_0, it is crucial to determine the magnetic field B_0 at the time of the β-NMR studies with great precision. A ^{2}H reference probe is hence deployed to perform pulsed NMR, see Section 3.1.1. It comprises a sealed glass tube filled with D_2O that has a height of $20\,\mathrm{mm}$, an inner diameter of $2\,\mathrm{mm}$ and an outer diameter of $3\,\mathrm{mm}$. The probe is located $25\,\mathrm{mm}$ to the side of the sample at the same height, see (e) in Figure 4.6. It is held in place by the coil wound around it for transmitting the B_1 field and receiving the FID signal. The difference in the magnetic field B_0 between the sample and the probe position was measured to be less than $0.1\,\mathrm{ppm}$ [63].

A second Rohde & Schwarz SMY01 rf generator is used to induce the B_1 field that excites the spins of the ^{2}H reference probe. This SMY01 for the reference probe and the other SMY01 for the β-NMR measurements share a common $10\,\mathrm{MHz}$ clock to ensure the ratio of the Larmor frequencies of the β-NMR sample and the reference is not affected by different internal clocks of the rf generators. The frequency ratio of the rf generators was evaluated for different frequencies and found to be off by less than $2\,\mathrm{ppb}$ (parts-per-billion).

4.3.3. Measurement types

Three types of β-detecting measurements are regularly performed at the VITO beamline fulfilling different purposes. They are briefly introduced here with the objective of their acquisition and their respective parameters:

Hyperfine structure (HFS) Ideal conditions for optical pumping are essential to achieve a high degree of nuclear spin polarisation and thus a good signal-to-noise ratio in the following measurements. Here, (part of) the hyperfine structure is recorded through the β-decay asymmetry as a function of the laser frequency perceived by the isotope beam by scanning over the voltage applied to the Doppler electrodes. One discrete voltage step, corresponding to one data point of the spectrum, is equivalent to one proton bunch impinged on the ISOLDE target. No rf is applied. The Doppler voltage belonging to the highest peak in the spectrum is noted, corresponding to the conditions yielding the highest nuclear spin polarisation. Its amplitude corresponds to the baseline of the following β-NMR and T_1 measurements. Saturation curves are also recorded to ensure a maximisation of the nuclear spin polarisation.

***T_1* scan** These measurements are recorded with a Doppler voltage fixed to the position of the highest peak in the HFS scan and no rf being applied. These scans observe the β-decay asymmetry as a function

of time to determine the spin lattice relaxation time constant T_1, as described in Section 3.1.2. No parameters are changed during the measurement, allowing to simply sum the data of multiple proton bunches for increased statistics. An exponential function is used to fit the data if it indicates a single relaxation component. Additional scans with the laser being blocked, i.e. no nuclear spin polarisation, are recorded to benchmark the T_1 acquisition against the instrumental asymmetry and evaluate the presence of longer relaxation components. T_1 scans are also used to verify a successful implantation of the polarised beam after a sample change.

β-NMR scan The Doppler voltage is again fixed to the potential determined in the HFS scan. As the name implies, the β-decay asymmetry is now acquired as a function of the frequency of the B_1 field induced by the coil around the sample to record a β-NMR spectrum. One discrete frequency step is equivalent to one proton bunch. When the applied rf is in resonance with the Larmor frequency of the nuclei, the asymmetry is being 'destroyed'. The peak recorded here consequently has the opposite orientation with respect to the HFS scan and its amplitude should be equivalent to the baseline of the HFS scan. In order locate the β-NMR resonance, frequency modulation is used to scan a broader range with fewer data points. Once the rough resonance position is established, the frequency modulation is deactivated and the resonance is scanned in smaller steps. Multiple scans with different rf amplitude are recorded to check for saturation and reduce power broadening. A reference measurement with the ^{2}H probe, cf. Section 4.3.2, is performed for each β-NMR scan to precisely determine the magnetic field B_0.

4.4. Data acquisition system

A major part of the work conducted for this thesis is the implementation of the VITO Control System (VCS), the new control and data acquisition system (DAQ) for β-NMR studies at the VITO beamline. VCS was developed in parallel to the upgrades of the experimental setup in 2021, which also included a superconducting magnet and new β detectors. It replaces the decades-old Master Control Program (MCP) which was originally designed for collinear laser spectroscopy on continuous isotope beams. As such, it counted the number of detected events occurring during a specified time. The functionality to acquire time-dependent signals was added to this system only later and only on a hardware level, meaning that the time windows of the acquisition had to be defined before the measurement. This represents a significant limitation for the data analysis of the β-NMR spectra since their signals are time-dependent as the orientation of the spins returns to thermal equilibrium, see Section 3.1.2. The relaxation time T_1 of the isotope in the host is not necessarily known before the experiment, hampering an appropriate setting of the observation time windows.

VCS resolves this issue and provides the highest-possible flexibility during the data analysis by characterising each detected β event individually in a time-resolved manner. The system can be divided into two main parts: one for slow signals setting all parameters for the acquisition of a data point, and one handling fast signals during the acquisition of that data point. An oscilloscope with a field-programmable gate array (FPGA) is the core of VCS. It runs customised firmware that controls the ISOLDE infrastructure and pre-processes the β events recorded by the detectors in real-time before sending their properties off to the host computer. A variety of devices is integrated in VCS for slow signals, including an digital-to-analogue converter to provide the Doppler voltage and an rf generator to record β-NMR spectra [63]. VCS is written in LabVIEW, based on the Control System++ (CS++) [21, 20, 107] developed by the Experimental Control Systems Group at GSI [22] and published under the European Union Public Licence (EUPL).

This section introduces the hardware used for VCS, followed by the firmware running on the FPGA and the LabVIEW application on the host computer before giving an outlook on the future of the system.

4.4.1. Control and data acquisition hardware

VCS uses a variety of commercially available standard hardware to reduce costs and increase maintainability. The main component of the system is a PCI eXtensions for Instrumentation Express (PXIe) crate that houses two modules; an oscilloscope with an integrated FPGA and a general purpose analogue-to-digital and digital-to-analogue converter (ADC and DAC). Additional hardware for the data acquisition include two rf generators for β-NMR and the reference probe as well as a PicoScope USB oscilloscope. An overview of the used hardware is explained in detail in this section. Figure 4.8 illustrates the communication of all devices involved in the data acquisition. Here, thick lines represent digital communication with the host computer, whereas thin solid lines are analogue signals and dashed lines show transistor-transistor logic (TTL) signals.

Host computer

VCS runs on a computer located at the VITO beamline that manages the incoming data from the FPGA and controls all peripheral devices. Furthermore, it shows a live view of the spectra being recorded and offers the option to perform a preliminary analysis to decide on the next measurements during a beam time. It has six hard disks combined in a RAID10 configuration that stripes the acquired data across three hard disks and uses the other three for mirroring. This achieves a redundancy and ensures no collected data is lost in the case of a hardware failure. After a measurement campaign, the data is moved to network storage at CERN. The computer is equipped with a NI PCIe-GPIB module to enable communication with older hardware via the General Purpose Interface Bus (GPIB).

PXIe chassis

The NI PXIe-1083 crate can house up to five extension modules [57]. It is connected to the host computer via Thunderbolt 3 allowing transfer rates of up to $500\,\mathrm{MB\,s^{-1}}$. Various PXIe modules are available from numerous manufacturers, allowing to adapt and upgrade the system in the future if necessary. The crate has an integrated reference clock that synchronises all inserted modules via the backplane connector.

FPGA oscilloscope card

The DAQ uses a NI PXIe-5170R oscilloscope with an integrated Xilinx Kintex-7 XC7K325T FPGA and $0.75\,\mathrm{GB}$ of storage [58]. It is installed in the PXIe-1083 crate and as such connected to the host computer, see Figure 4.8. The card's clock frequency is $250\,\mathrm{MHz}$ and its sampling rate is up to $250\,\mathrm{MS/s}$. It has four analogue inputs with a 14-bit resolution and a range of $-5\,\mathrm{V}$ to $5\,\mathrm{V}$ used to read out the signals from the β detectors. In addition, it is equipped with six channels for logic signals with the same resolution of up to $250\,\mathrm{MHz}$ ($4\,\mathrm{ns}$). These are used to receive the trigger when the protons impinge the ISOLDE target (proton trigger) and to control the ISOLDE infrastructure, including the beam gate, the cooler buncher ISCOOL and a shutter for the laser. While the logic channels accept TTL inputs, their output is limited to $3.3\,\mathrm{V}$. A logic level shifter is therefore added to the outputs of the FPGA to drive the TTL hardware. The FPGA can be programmed in LabVIEW through the usual block diagrams, which are then compiled in a hardware description language (HDL). Every time the DAQ is started, the bitfile containing the firmware is loaded to the FPGA. It is therefore possible to easily integrate the FPGA into the LabVIEW DAQ and use it for pre-processing the data before it is streamed to the host computer for the analysis.

General purpose I/O card

The second extension card in the chassis is a NI PXIe-6341 [59]. This general purpose input/output card has a sampling rate of $500\,\mathrm{kS/s}$ and total of 16 analogue inputs and two analogue outputs with $16\,\mathrm{bit}$ resolution. Another 24 connections are available for digital signals. One of the analogue outputs is used for tuning the isotope beam in resonance with the laser. It provides a voltage in the range of $-10\,\mathrm{V}$ to $10\,\mathrm{V}$ to a Kepco BOP100 bipolar amplifier with a gain of 100. The resulting potential is applied to the Doppler electrodes and changes the energy of the isotope beam by up to $\pm 1\,\mathrm{keV}$.

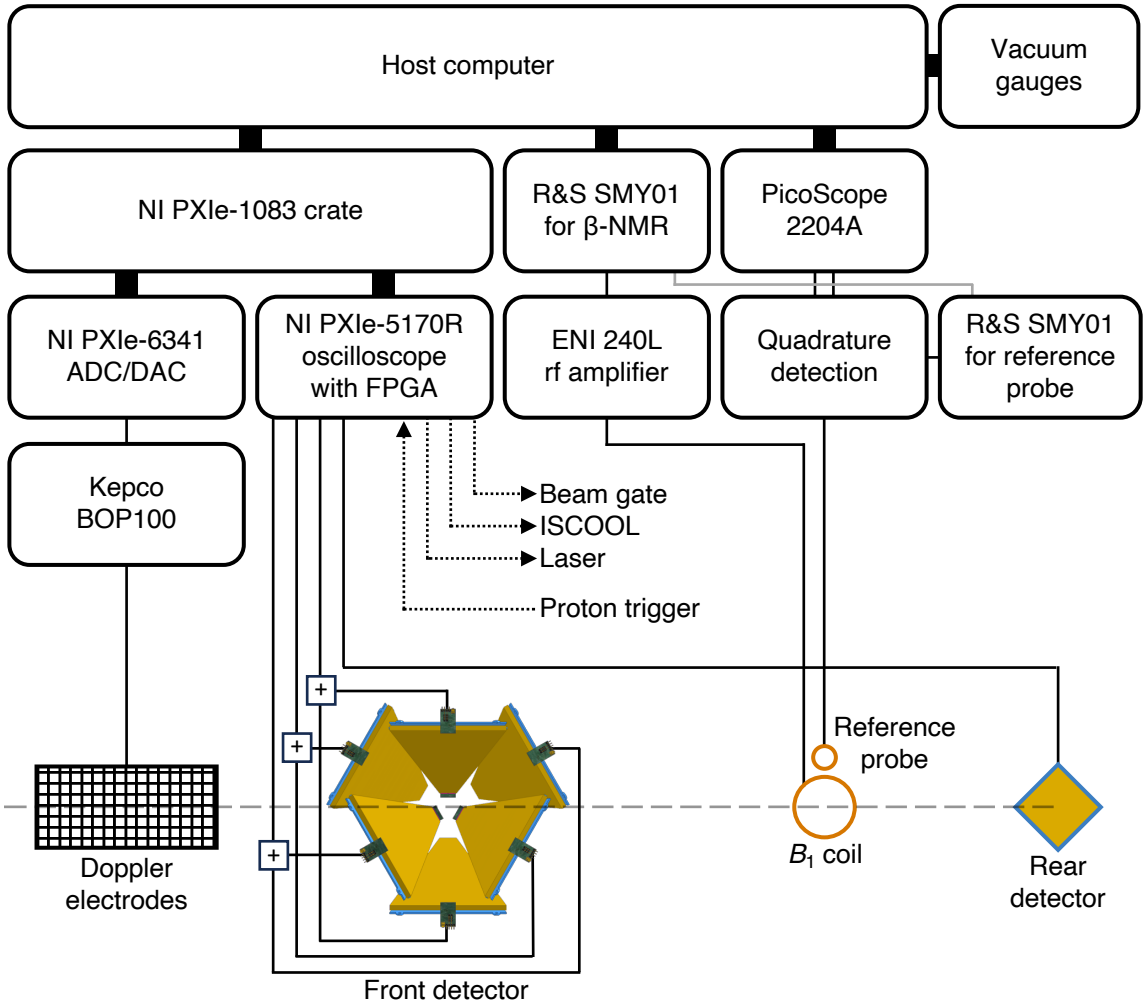

Figure 4.8.: Schematic of all devices involved in the data acquisition and how they interact (top). Thick connections between devices indicate digital communication with the DAQ whereas thin connections are analogue signals. The dotted connections represent TTL signals to receive the proton trigger from ISOLDE and control the beam gate, the cooler buncher ISCOOL and the laser shutter. Note the connection between the two SMY01 rf generators that establishes a common reference clock. The bottom part shows the beamline components relevant to the DAQ, and their order on the beam axis (dashed line). It depicts how the DAQ provides the Doppler voltage and the magnetic field B_1, and what equipment reads out the detectors as well as the reference probe determining the field B_0.

Additional hardware

A Rohde & Schwarz SMY01 rf generator provides the signal for the magnetic field B_1 that excites the spins in β-NMR measurements. The rf generator communicates with the host computer via GPIB. To generate a sufficiently high rf field, the signal is amplified by a ENI 240L broadband amplifier.

As of the writing of this thesis, further hardware required for the β-NMR measurements is not integrated in VCS yet. A second Rohde & Schwarz SMY01 rf generator supplies the ^{2}H reference probe for it to induce the B_1 field, as explained in Section 4.3.2. This SMY01 for the reference probe and the other SMY01 for the β-NMR measurements have a common reference clock to minimise discrepancies in the ratio of their output frequencies. A PicoScope 2204A USB oscilloscope takes the two components of the ^{2}H reference probe's FID as an input to determine the magnetic field B_0 with quadrature detection, see Section 5.2.2. The oscilloscope offers two input channels and a bandwidth of $10\,\mathrm{MHz}$ with a maximum vertical range of $\pm 20\,\mathrm{V}$ [112]. Furthermore, the host computer obtains the vacuum pressures at different positions of the beamline from two Pfeiffer MaxiGauges to log them and allow remote supervision.

4.4.2. FPGA firmware

This section describes the centrepieces of the new DAQ. The FPGA oscilloscope controls the beam release and other ISOLDE infrastructure through an integrated pulse pattern generator. Even more importantly, it pre-processes the detected β events in real-time by selected properties before streaming them to a host computer for an in-depth analysis. The FPGA runs a customised version of the 'Stream to Host.vi' oscilloscope example provided by NI that is complemented with additional features. All channels sample the signals at a frequency of $250\,\mathrm{MHz}$, equivalent to a time resolution of $4\,\mathrm{ns}$. Its main loop, on the other hand, runs at a frequency of $125\,\mathrm{MHz}$, resulting in two samples being acquired and processed per channel per main loop clock cycle. The firmware is optimised to handle β events detected with the SiPMs that have pulse durations in the order of $100\,\mathrm{ns}$ to $200\,\mathrm{ns}$ and peak rates of up to $1\,\mathrm{MHz}$, decreasing with the decay of the isotope, usually with a half-life around $1\,\mathrm{s}$.

Pulse pattern generator

A variety of logic signals needs to be handled by the DAQ with high time resolution to synchronise the infrastructure at ISOLDE and the data acquisition, allowing to e.g. control the release of the isotope beam. Most importantly, VCS needs to receive a TTL pulse with a duration of $15\,\mu\mathrm{s}$ when the protons impinge the target in order to start the acquisition routine. After about $6\,\mathrm{ms}$, when the high voltage used to extract the ions from the target has stabilised, the beam gate is opened by supplying a TTL `HIGH` to ISOLDE's user beam gate input. This signal remains on `HIGH` as long as the beam gate is supposed to stay open, e.g. $500\,\mathrm{ms}$. Doing so fills the cooler buncher ISCOOL with the isotope beam, allowing it to cool (see Section 4.2). Another TTL output is then required to change from `HIGH` to `LOW` to pull down a potential on ISCOOL's extraction plate. This releases all of the beam towards the experimental setup during a relatively short time, normally in the order of $5\,\mathrm{ms}$, and thus ensures a quasi-simultaneous implantation of the nuclei into the sample as is required for T_1 relaxation measurements. A third TTL output controls a shutter for the laser used for optical pumping. It is for safety reasons only on `HIGH`, equivalent to an open shutter, during the acquisition when a polarised beam is required. Figure 4.9 gives an overview on a typical pattern of the TTL signals.

The customisation of the FPGA firmware allows to integrate a pulse pattern generator offering one trigger input and five outputs into VCS. With the FPGA handling the entire trigger logic for the ISOLDE beam gate, ISCOOL and the laser shutter, additional hardware to create pulse patterns is no longer required. The actual implementation in the firmware is rather simple, with the corresponding block diagram of the Virtual Instrument (VI) shown in Figure 4.10. To configure the pulse pattern generator, the user needs to enable it with `Enable DPG` and specify a delay with respect to the proton trigger after which the logic level changes and a duration for how long it remains on that level. These values can simply be modified in the corresponding

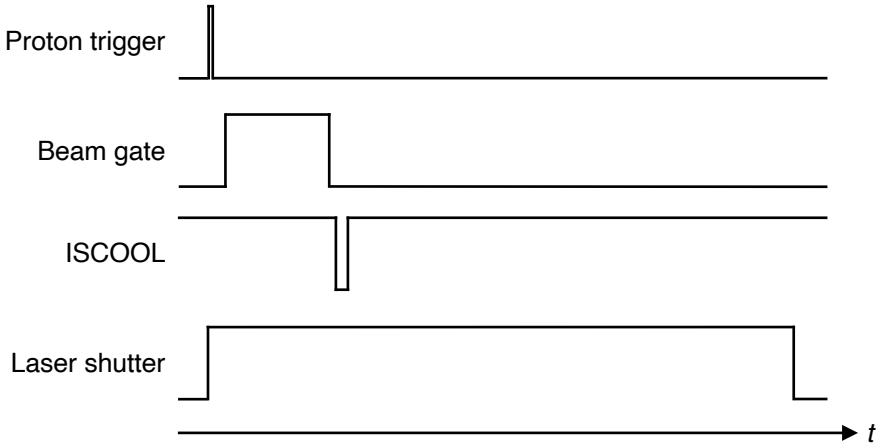

Figure 4.9.: Logic input and outputs required during the acquisition of one data point. After the recording is started with the incoming proton trigger from ISOLDE, signals are send to open and close the beam gate and ISCOOL as well as the laser shutter. Note the inverted logic of ISCOOL which releases the isotopes on a logic `LOW`.

part of the `*.ini` file (see Section 4.4.3). Once the proton trigger is received, the outputs `PD0` to `PD4` will change their state according to the sub-VIs in the centre of the block diagram. This sub-VI, cf. Figure 4.11, compares the time since the proton trigger with the user-defined delays and widths and changes the state accordingly. Note that the output designated for ISCOOL is inverted as it releases the isotope beam towards the experiment on a logic `LOW` rather than `HIGH`. The outputs `PD3` and `PD4` are prepared for future additions to the DAQ and therefore not further explained at this stage.

Window coincidence mask

The main VI on the FPGA includes a function that then checks if one of the two samples acquired per main loop clock cycle fulfils the current trigger condition and is therefore active, i.e. if one of the samples is above the trigger threshold in case the DAQ is set to a leading edge trigger. It translates this information into the so-called window coincidence mask (WCM) which provides information what channels are active during this clock cycle. The representation of the WCM is an 8-bit integer where the states of the first four bits correspond to the four channels of the DAQ being active or not. The WCM is written to a FIFO (First In First Out) together with a timestamp and the ADC values of the two samples in each loop iteration. This data is then read from the FIFO to characterise the β events, see next section.

β event characterisation

The objective of using an FPGA oscilloscope for pre-processing the incoming data is to enable a time-resolved recording of all detected β events for a flexible and comprehensive data analysis while retaining a comparatively small file size. This is achieved by characterising the signals by a selection of properties in real-time. Only these properties are then streamed from the FPGA to the host computer rather than full waveforms, thus maximising the available bandwidth for higher signal rates and the efficiency of the data handling.

An exemplary signal that is typical for a β event acquired with SiPMs as used in the detectors is shown in Figure 4.12. It illustrates which properties of a pulse can be recorded by analysing the waveform of an event. The first is the event's time of arrival `Time` that is defined as the time between the proton trigger and the signal exceeding the trigger threshold. Next is the amplitude `Maximum` of this event. Additionally, the

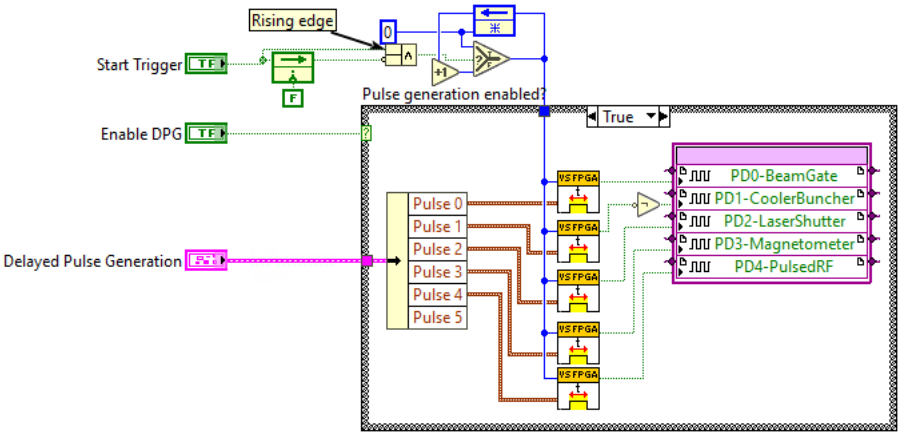

Figure 4.10.: Implementation of the pulse pattern generator on the FPGA utilising the PFI inputs and outputs to control the ISOLDE infrastructure. Note the inversion of the output controlling ISCOOL. The top part ensures that a rising edge has been registered in the proton trigger `Start Trigger`.

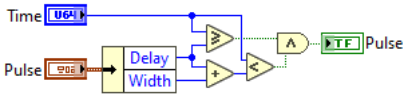

Figure 4.11.: Sub-VI selecting the output state based on the elapsed `Time` since the proton trigger and the user-specified `Delay` and `Width`.

`Integral` is calculated up to the time when the signal falls again below the trigger threshold. The time over threshold `ToT` is thus also obtainable, as indicated in the exemplary waveform.

Figure 4.13 shows the most important parts of the block diagram calculating the pulse properties on the FPGA. The VI updates the `Pulse Properties` cluster based on the incoming data from the FIFO if at least one of the channel's two samples acquired during that clock cycle is at or above the trigger threshold. With the oscilloscope having four channels, there are four parallel instances of this VI running on the FPGA to process the signals. Presented here is therefore a basic description of the working principle referring to only one channel and its two samples per main loop clock cycle. Essential for the calculation of the pulse properties are the inputs `Channel`, `WCM` and `Previous WCM`, representing the channel to be analysed and the WCM of the current and previous clock cycle. The logic in the bottom left of the block diagram, see Figure 4.13, utilises these inputs to distinguish between four possible cases: 1. both clock cycles inactive, 2. first clock cycle inactive, then active, 3. both clock cycles active, and 4. first clock cycle active, then inactive. Here, 'active' refers to at least one of the two samples per clock cycle being above the trigger threshold.

When the VI determines the pulse properties of the events in a channel, it also keeps track what other channel(s) may be active at any point during an event. If another channel becomes active, its corresponding bit in the `WCM` input of the VI changes to 1. This `WCM` is compared to that in the `Pulse Properties` with a logic `OR`, meaning that a channel becoming active will change its bit to 1 in the `WCM` of the `Pulse Properties` cluster. The bit representation of this event's `WCM` will therefore remain at 1 even if the other channel is no longer active, thus allowing to efficiently record what other channels are active at any point during the event.

All other pulse properties (`Integral`, `Maximum` and `ToT`) are computed in the `case structure` in the centre of the VI. The cases, shown in Figure 4.14, are in accordance with the four possibilities mentioned above and may need a further discrimination depending on the samples `Data_0` and/or `Data_1` being active. They are now briefly introduced:

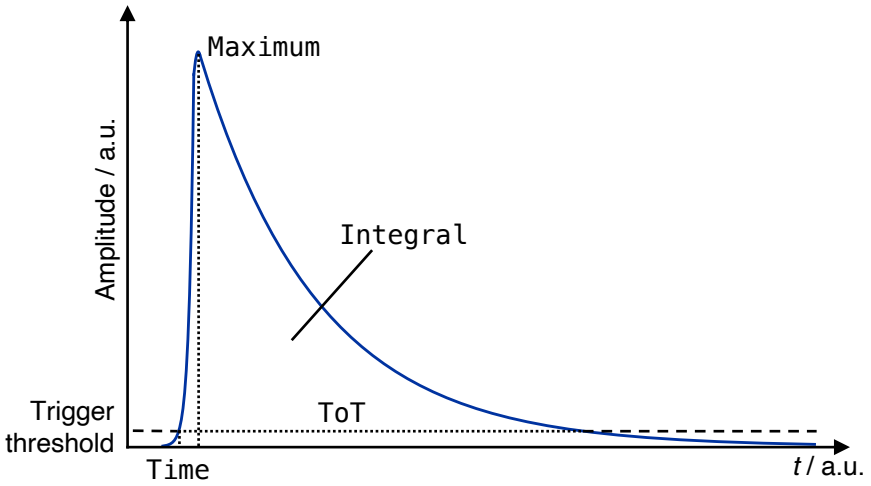

Figure 4.12.: Schematic illustrating the different properties of an event recorded in the β detectors to be characterised. The characterisation is initiated when the incoming signal exceeds the trigger threshold at the `Time` of arrival. The signal is considered an event during the time over threshold until it falls below the trigger threshold. During the time over threshold `ToT`, the event is characterised by its `Maximum` amplitude and its `Integral`.

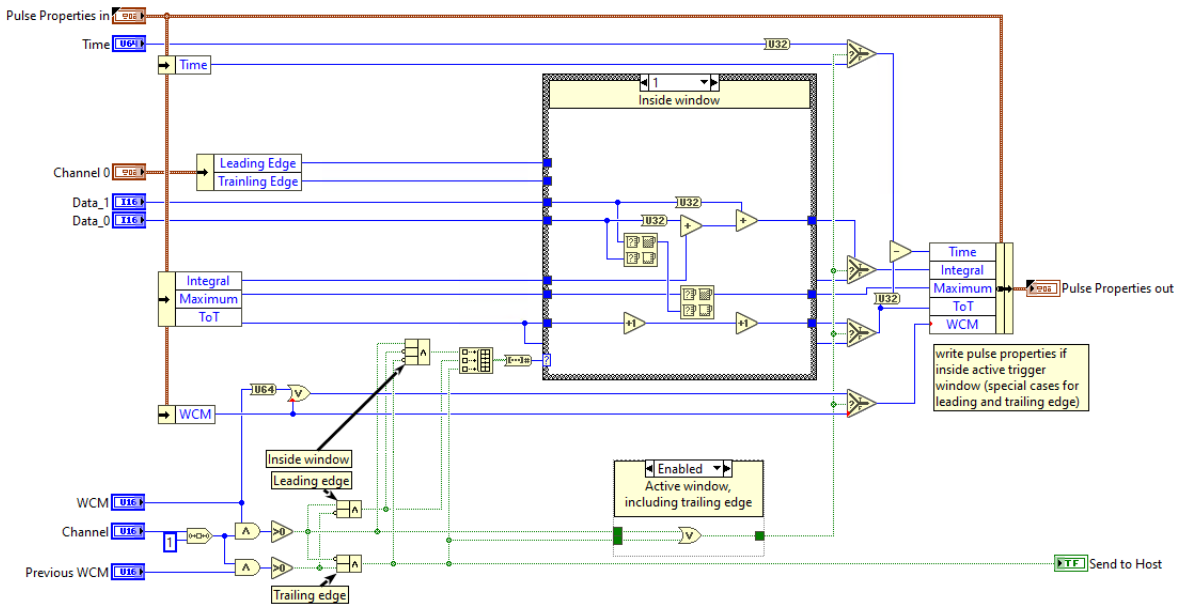

Figure 4.13.: The VI calculating the selected pulse properties in real-time as the events are being registered. To do so, it takes the two samples `Data_0` and `Data_1` of the clock cycle and applies simple comparisons and summing functions. For further details and explanations of the `case structure`, see text and Figure 4.14.

1. Both clock cycles inactive. As seen in Figure 4.14a, no pulse properties are calculated since neither sample is part of a β event. The `Pulse Properties` remains at its initialised values of 0.

2. First clock cycle inactive, then active. A differentiation needs to be made for this leading edge depending on one or both samples being active in Figure 4.14b and 4.14c. The time over threshold `ToT` is incremented by one or two time units, referred to as 'ticks'. With the sampling rate of the FPGA being $250\,\mathrm{MHz}$, one tick is equivalent to $4\,\mathrm{ns}$. The `Time` of arrival is computed as the current time subtracted by `ToT` to consider the number of samples active during that main loop clock cycle. The integral is simply `Data_1` or the sum of `Data_0` and `Data_1`. For the `Maximum` the larger of the two samples is taken.

3. Both clock cycles active. Both samples `Data_0` and `Data_1` are added to the previous `Integral` of the `Pulse Properties` cluster. The previous value of `Maximum` is also compared to the current samples and the highest value is taken. With both samples being active, the `ToT` is incremented by two ticks.

4. First clock cycle active, then inactive. The trailing edge requires a further discrimination between one or no samples being active. As before, if one sample is active, it is added to `Integral` and compared to `Maximum`. One tick is added to `ToT`. If no sample is active, the `Pulse Properties` cluster remains unchanged. Additionally, the logic at the bottom of the VI in Figure 4.13 detects a trailing edge and thus sets the `Send to Host` boolean to `TRUE` when the signal falls below the trigger threshold.

Once the `Send to Host` boolean is `TRUE`, the `Pulse Properties` cluster is sent to another FIFO from where it is made available to the host computer via DMA (Direct Memory Access). This simple approach characterising the pulse properties on the FPGA thus allows for a reconstruction of the signals and for an in-depth data analysis on the host computer.

Additionally, the `Send to Host` boolean is used on the FPGA to count the number of events that are registered per channel during three user-defined time windows. These three counters per channel are also streamed to the host computer and used to compute the β decay asymmetry displayed in a live view of the incoming data. This allows for a basic on-line analysis to check the progress of an ongoing scan. It is moreover possible to stream the raw data to the host computer. In this case, the events of all channels will not be characterised and simply be forwarded to the host whenever they are above the trigger threshold. This approach is used solely for debugging purposes as recording the waveforms of all events would result in significantly higher data rates without yielding meaningful additional information relevant for the β-decay asymmetry.

4.4.3. Software on the host computer

VCS is the implementation of CS++ tailored to the requirements of the VITO experiment. CS++ amends the LabVIEW Actor Framework by a collection of libraries. The Actor Framework is a model in which different parts of a program, so-called Actors, perform tasks simultaneously [20]. They communicate via messages to tell each other what to do, e.g., performing a task, sending messages to other Actors or launching Actors on their own. The asynchronous messages are advantageous for a simple implementation of callback messages, ensuring that the execution of a task was successful. For example, it allows to check if a device is connected correctly or if settings have been applied to a device. Every device of the DAQ as well as every major task, such as preparing a measurement and acquiring data, has its own Actor in the Actor Framework. In the case of hardware, for example, an Actor wraps around the driver of a device that enables its integration into the Actor Framework. Here, an abstract message can be sent to the Actor of the device to apply the corresponding setting through the device's driver. The Actors are hence entities that can be replaced as a whole to ensure modularity and maintainability. For example, in the case of a hardware failure, it is not necessary to rewrite

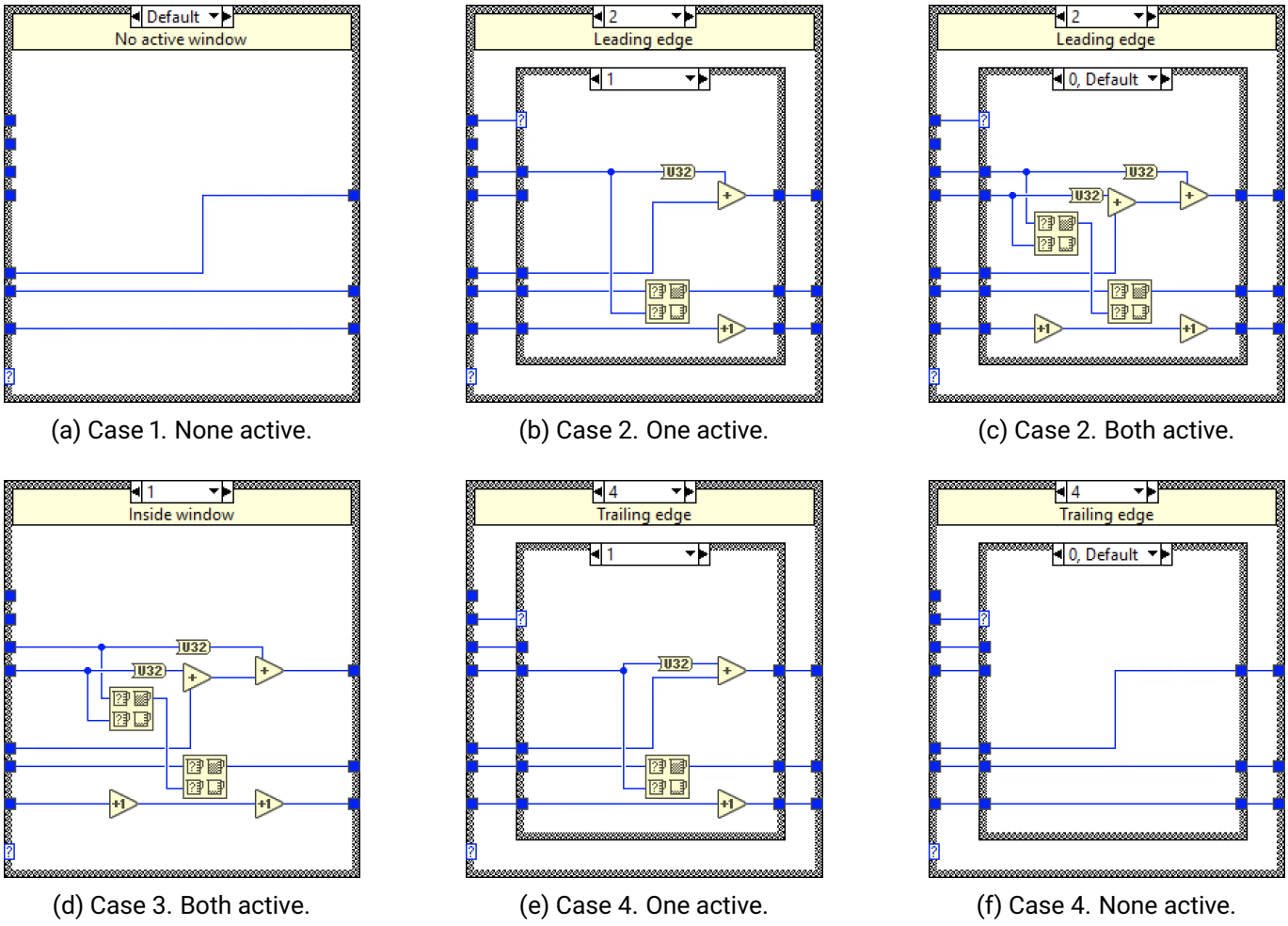

(a) Case 1. None active. (b) Case 2. One active. (c) Case 2. Both active.

(d) Case 3. Both active. (e) Case 4. One active. (f) Case 4. None active.

Figure 4.14.: The different cases in the `case structure` of Figure 4.13 for 1. channel inactive in previous and current clock cycle, 2. channel inactive in previous cycle and now active, 3. channel active in both cycles, and 4. channel active in first cycle and then inactive. When necessary, a discrimination is made for the cases depending on the of samples `Data_0` and `Data_1` of that clock cycle being active, i.e. above the trigger threshold.

major parts of the software, but to re-address the corresponding messages to the Actor of a spare device without having to change their format or the way they are generated. It is furthermore possible to create a dedicated graphical user interface (GUI) for each Actor, allowing to control individual hardware components for debugging purposes.

A configuration file, the `*.ini` file, is read by VCS upon start-up. Each Actor has its own two sections in this file, one with parameters relevant for the Actor and one with network addresses used to publish selected variables online. These parameters are settings that are not changed during a measurement, such as trigger thresholds, the timings of the pulse pattern generator or the directory where to save the data. Changing the parameters requires a restart of the DAQ to re-initialise them. The advantage is that all relevant parameters are available in the same file and accidental changes are unlikely. To keep track of the parameters, they are also saved in the measurement files. Some variables checked or recorded by VCS may be relevant even during an acquisition, e.g. the current number of β events in the respective detectors in a given time window. It is therefore possible to make use of LabVIEW's Shared Variables. The addresses of the variables specified in the `*.ini` file are read and used to publish the quantities from the host computer to make them available in the NI's Distributed System Manager. They are thus accessible through other applications or even from other computers, for example to provide a live view of the ongoing measurement. Depending on the specified access scope, it can be decided if the variables can be read only or also edited. Basic checks or control can therefore be enabled from any computer on the network for debugging purposes. Another aspect of VCS is the integration of the Datalogging and Supervisory Control (DSC) Module to show alarms and wait for their acknowledgments.

This section briefly introduces the GUI to enter the measurement parameters, the sequencer that handles the parameters in a state machine and the saving of the data.

Graphical user interface

The most prominent Actor to the user is `VCS_Measurement_GUI` which provides the GUI prompting to specify the settings according to the measurement types HFS, T_1 and NMR (see Section 4.3.3). Figure 4.15 shows a screenshot of the GUI with exemplary settings for a β-NMR measurement of ^{47}K in EMIM-DCA (see Section 5.1 for more information). It is first necessary to define the used isotope and a sample ID that is unique to the measurement. The parameters include the frequency range and the step size as well as the amplitude of the rf generator output. Further settings are the modulation frequency and its depth required during the initial search for a β-NMR resonance. The Doppler voltage that yielded the highest degree of spin polarisation, i.e. the highest β decay asymmetry in the HFS scan, needs to be specified, too. It is possible to enable shuffling the frequency steps to avoid asymmetric peak broadening that can occur when the frequencies are measured sequentially from low to high or high to low. The number of scans gives the option to gather more statistics on the specified measurement range. Once the user initiates the acquisition by clicking 'Send', the progress bars update based on the user-defined parameters, in this case performing three scans on the 212 steps covering the frequency range. The user-defined settings are then combined in a cluster and sent via message to the Actor `VCS_Measurement` that handles the measurement sequencer explained in the next section. In addition to the regular measurement types, a 'manual' option is implemented that allows editing parameters like the timing of the pulse pattern generator without changing the `*.ini` file. This option is used only during the initial start-up of a beam time in order to find appropriate settings for the beam gate timing or ISCOOL before launching the actual β-NMR measurement.

Measurement sequencer

`VCS_Measurement` coordinates all devices, the FPGA and the host computer to acquire one measurement. The Actor first produces parameter sets that are added to a queue, with one parameter set containing all settings required to record a single measurement step. These parameter sets are taken from the queue and processed in a state machine that applies the corresponding settings to all devices and initialises the data

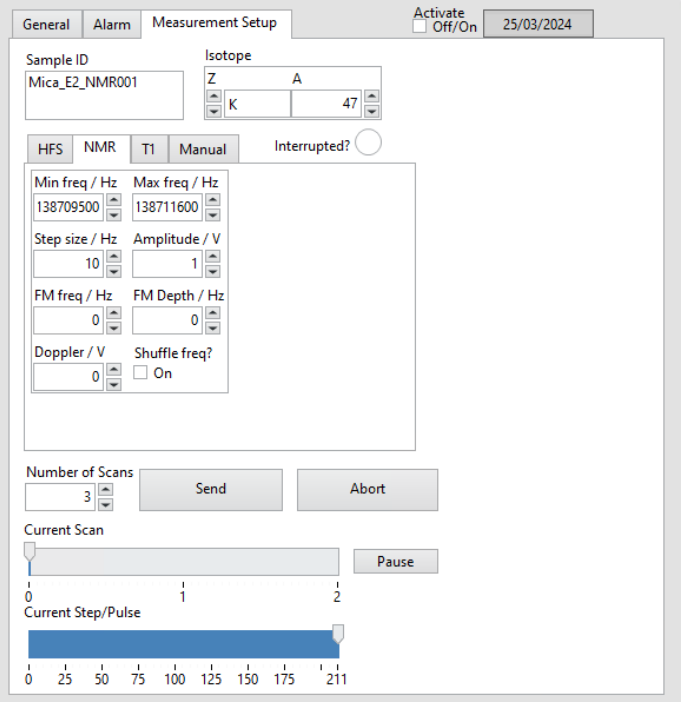

Figure 4.15.: Screenshot of the graphical user interface that prompts the user to enter the measurement parameters. Shown are exemplary settings of a β-NMR scan of ^{47}K implanted in EMIM-DCA on a mica sheet with three scans over the specified frequency range.

acquisition on the FPGA. All pulse properties of the β events of this measurement step are then recorded for a user-defined time window that is chosen in accordance with the isotope's half-life and its spin relaxation time. A major benefit of this producer/consumer pattern is the ability to pause or abort the measurement when necessary while keeping all recorded data. Introduced in this section is an overview on the most important aspects of this approach. A flow chart illustrating the sequencer managing the measurements is shown in Figure 4.16.

As mentioned above, the user defines the settings of a measurement through the `VCS_Measurement_GUI`. This Actor sends a message to `Setup Measurement` to produce parameter sets that represent the settings that need to be applied to the different VCS components to acquire the individual steps of the measurement. One parameter set contains all information for one measurement step/data point, e.g. for a β-NMR scan, it contains the Doppler voltage, the rf amplitude and the modulation settings as well as the rf frequency of the corresponding data point. An exemplary case for `Setup Measurement` preparing such parameter sets for a β-NMR measurement is depicted in Figure 4.17. The `Parameters` cluster in pink at the top contains all parameters that need to be assigned for all measurement steps. Some of them are hardcoded in this VI since they never need to be changed by the user, such as the unit of the rf generator's amplitude. The settings defined by the user through the GUI are fed into the VI via the pink input on the left. If they remain static during a β-NMR measurement, e.g. the rf amplitude and modulation as well as the Doppler voltage, they are simply assigned to the `Parameters` cluster. The only variable that does change during a β-NMR measurement is the frequency of the applied B_1 field, that is defined by the user through `RFStep size`, `RFMax freq` and `RFMin freq`. These variables serve as the input for the LabVIEW-integrated `Ramp Pattern` VI that provides an array of frequencies covering the user-defined range with the according step size. This array

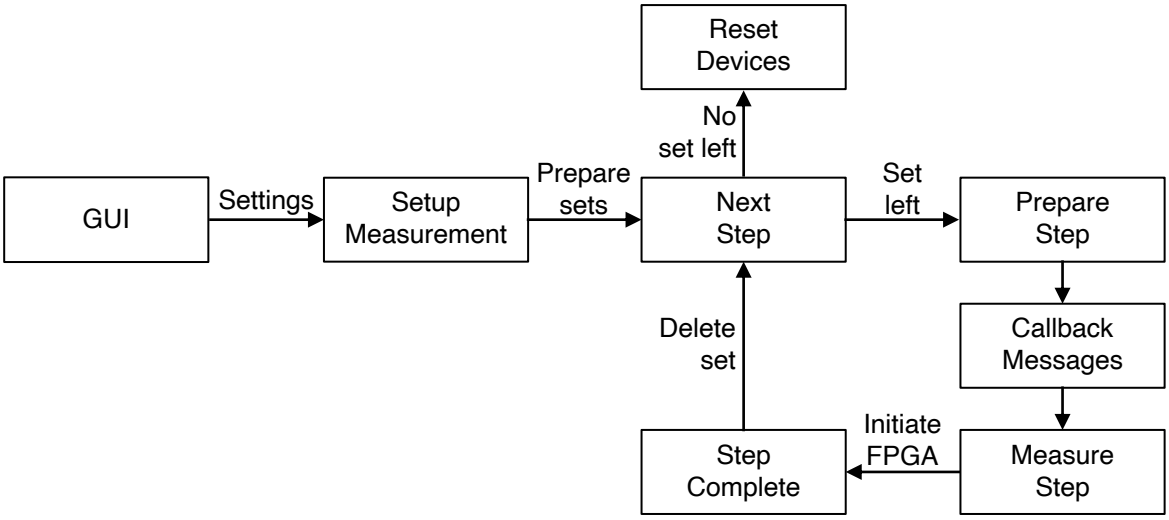

Figure 4.16.: Flow chart of the sequencer that handles the preparation and the acquisition of the measurements. The GUI provides the measurement settings defined by the user to the `Setup Measurement` VI that produces parameter sets, where one set is equivalent to one measurement step. These parameter sets are then processed in the loop on the right with one iteration being equivalent to one step/data point. See text for further details.

can optionally be shuffled to randomise the order of the frequencies to avoid asymmetric peak broadening. Finally, an indexing for loop iterates over the frequency array. It substitutes the default frequency value in the `Parameters` cluster and thus returns an array of clusters that all have different frequencies. This array represents the parameter sets. To gather more statistics on the defined measurement range, the outer for-loop can iterate over the parameter set generation multiple times, with one iteration being equivalent to one scan on the full measurement range. The parameter sets are then added to a queue (not shown in the block diagram) and a message is sent to `Next Step` to continue the preparations of the measurement, see Figure 4.16.

When a new measurement is started, the `Next Step` VI checks if the isotope and the sample ID have been defined and prompts a message to the user if this is not the case. It then checks whether there are still parameter sets left in the queue. If this is not the case, the measurement has been completed and the user will be notified, as indicated in Figure 4.16. Otherwise the next parameter set will be taken from the queue and some of the parameters will be published as Shared Variables to make them accessible for a live view, e.g. the B_1 frequency of the next step or the Doppler voltage. A message containing the parameters of the next step is then sent to the `Prepare Step` VI.

This VI, seen in Figure 4.18, first sets a cluster of three booleans used for callback messages to `FALSE`. The callback messages are an important feature at this point. After verifying that the Actors handling the rf generator, the DAC for the Doppler voltage and the pulse pattern generator have been launched and are thus available, the Actors will be sent their corresponding parameters. The devices then apply these settings to prepare for the next measurement step. Only if the messages containing the settings have been received successfully by their Actors, the callbacks set their booleans to `TRUE` and the measurement can proceed.

Once all callbacks have been received without any error, the `Measure Step` checks how much time has elapsed since the previous measurement step was initiated and compares this value to `Minimum Trigger Gap`, shown in Figure 4.19. If necessary, the VI will wait until the user-defined minimum time between two triggers is met. This function is essential to make sure that the previous isotope bunch implanted into the sample has decayed before the next bunch is being implanted, which could otherwise affect the signal-to-

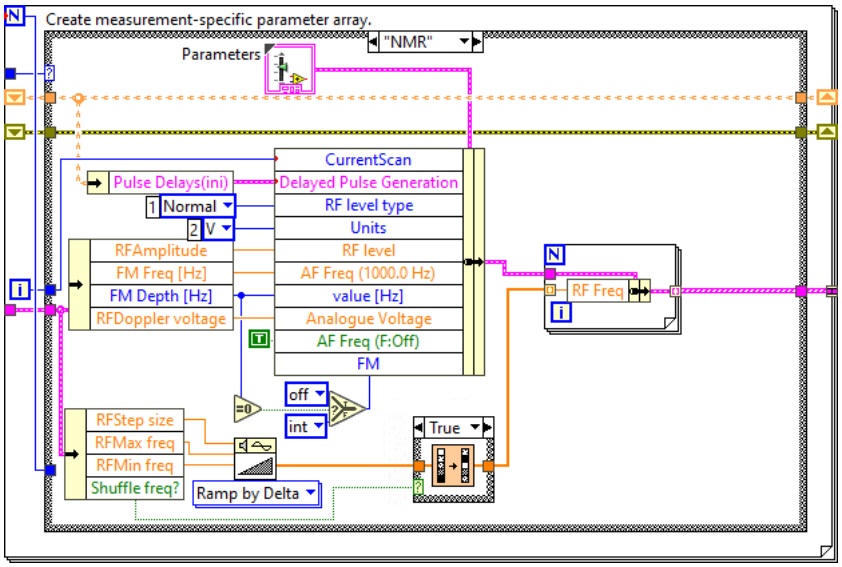

Figure 4.17.: Part of the `Setup Measurement` VI that produces the parameter sets to be added to a queue or further processing in the state machine. Shown is an example preparing a β-NMR measurement, with the generation of all frequency steps covering the user-defined range in the bottom part. For more details, see text.

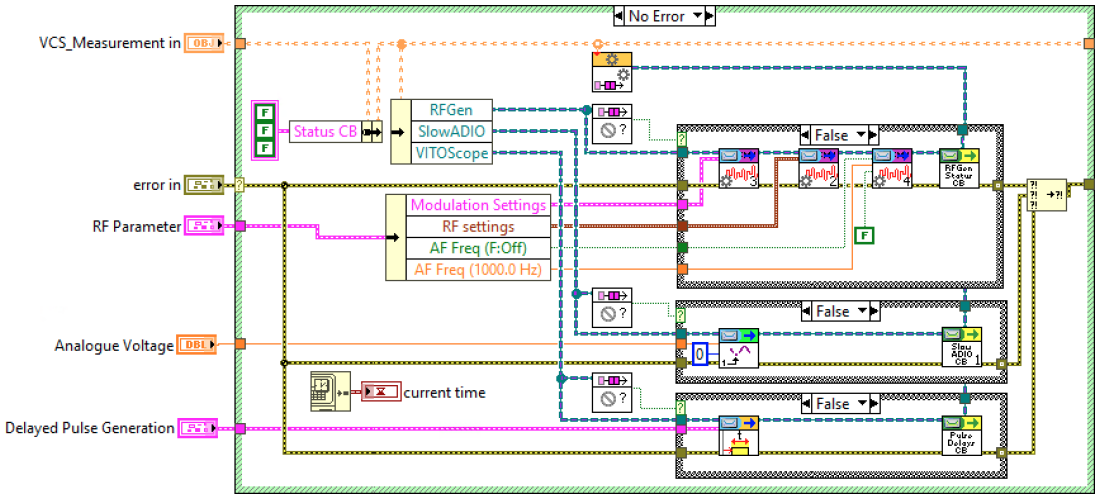

Figure 4.18.: The `Prepare Step` VI that sends messages to the Actors handling the rf generator, the Doppler voltage and the pulse pattern generator to apply the parameters of the next measurement step to the devices. Their callbacks ensure that the parameters messages have been received correctly.

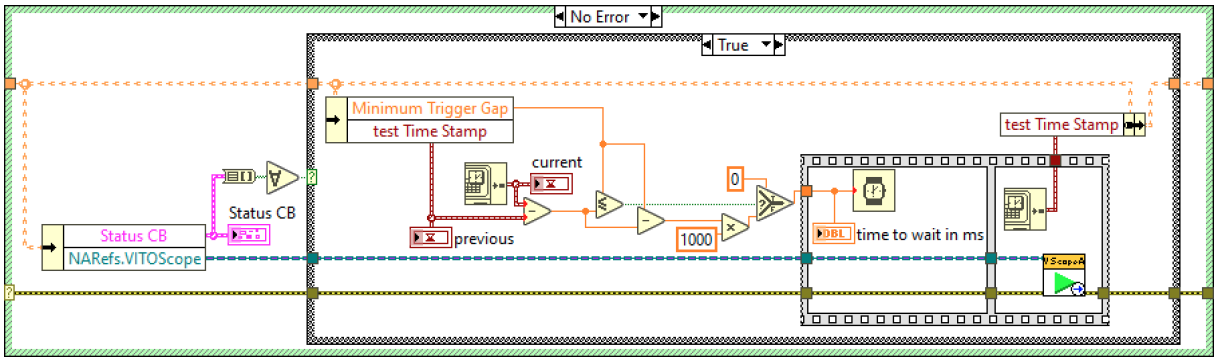

Figure 4.19.: The `Measure Step` VI that verifies that all callback messages have been received and that the `Minimum Trigger Gap` between two trigger signals has elapsed before initiating the data acquisition of this measurement step on the FPGA oscilloscope.

noise ratio. When this timing condition is reached, a message is sent to the `VITOScope` Actor handling the oscilloscope to initiate the FPGA and start the acquisition and the pulse pattern generator when the next proton trigger is received. The calculated pulse properties are fetched continuously from the FPGA to free up memory for the next β events to be characterised.

When the acquisition of this step has finished and the status of the FPGA changes back to idle, the `Step Complete` VI removes the parameter set of this step from the queue and sends a message to `Next Step`. Depending on whether or not there are parameter sets remaining in the queue, the measurement will either continue with the next parameter set or the user will be informed that the measurement has been complete, cf. Figure 4.16. All connected devices are then set to a default 'safe mode', meaning that all outputs are effectively turned off for safety reasons. When the user launches the next measurement, new parameter sets will be produced in the `Setup Measurement` VI and sent to the sequencer state machine.

VITO Scope and live view

The `VITOScope` Actor is the FPGA's counterpart on the host computer that integrates it into VCS. It is responsible for all communication with the FPGA, transferring the data to the host for saving and making it accessible for a live view during the acquisition. As described earlier, the FPGA firmware pre-processes the incoming β events and writes their properties to DMAs. `VITOScope` accesses these DMAs as soon as the data is available and continuously fetches the pulse properties arrays, cf. Figure 4.20. Note that the arrays have a length of eight even though they contain only seven pulse properties. Due to technical reasons, the FPGA's DMA need to have a length that is a power of two. The data of all four channels of the FPGA oscilloscope is then combined into a `Pulse Properties` cluster and sent to the Actor handling the data saving.

In addition to fetching the pulse properties, `VITOScope` also reads the values of the three counters mentioned in Section 4.4.2. The counters provide information on the number of β events detected across the four channels during three user-defined time windows. For a basic implementation of a live view, the counters are then published as Shared Variables to make them accessible in different programs and on other computers on the network. The β decay asymmetry is then calculated in the live view application as the normalised difference in the number of counts between the two detectors, cf. Equation (3.16). Depending on the type of the measurement, the asymmetry is shown as a function of Doppler voltage for a HFS measurement or as a function of ν for a β-NMR measurement. The live view allows the user to observe the evaluate the incoming data in real-time and decide on the next measurements.

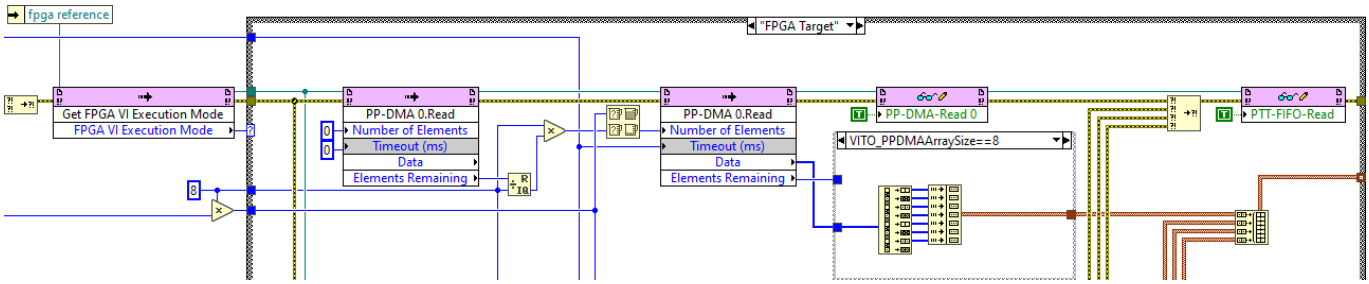

Figure 4.20.: A part of the `Fetch PP DMA` VI. Exemplarily shown here is accessing the FPGA's `PP-DMA 0` containing the calculated pulse properties of channel 0. The DMA's of the other three channels are accessed in the same way. The pulse properties of all channels are bundled into a cluster and sent to the Actor handling the saving (not shown).

Data saving

Saving the data is handled by `VCS Measurement Data`. The data is saved as a TDMS file, a binary, hierarchical format that is optimised for measurement data. While it is proprietary to NI, a variety of add-ons and packages is available to read the data in other programs and languages, such as MATLAB and Python [55, 95]. TDMS offers a three-level hierarchy that structures a measurement in files, groups and channels. All of these three levels may contain additional properties. VCS records one TDMS file per measurement and utilises the hierarchy to organise the data with respect to the three levels, e.g. the sample ID on the file level, rf settings on the group level or the time of arrival on the channel level. An overview on the entire file structure is on display in Figure 4.21.

4.4.4. Possible improvements

As of the writing of this thesis, not all possibilities of VCS are fully exploited. While additional outputs of the pulse pattern generator are already implemented, e.g. to perform pulsed NMR, they are currently not in use. Supplementary features that can amend the software are warnings and alarms to facilitate the supervision of the experiment and notify the user in case of problems, such as hardware failures, unexpected pressure readings, etc. The pressures acquired with the vacuum gauges currently lack logging in VCS. Beneficial would also be the full integration of the PicoScope to automatically record the FID of the ^{2}H reference probe for each β-NMR measurement rather than doing this manually.

Something else to consider is the usage of the HDF5 file format. HDF5 is designed for storing large amounts of scientific data, similar to TDMS, but it is an open format and offers more flexible hierarchy and better read/write accessibility compared to NI's proprietary TDMS format. Another drawback of NI's system is a number of VIs and registers running on the FPGA that cannot be accessed nor modified by the user. This prevents from implementing an FPGA firmware that is not based on one of NI's example codes, which mitigates developing additional features. At the moment, parts of VCS rely on LabVIEW's DSC Module, which is not available as a 64-bit version, therefore requiring all of VCS to run in 32-bit LabVIEW. VCS thus experiences performance limitations, especially with respect to the memory on the host computer that is available to buffer the data before writing it to disk when the β particle count rates are high. One option to overcome this issue is removing the respective part of VCS and omit warnings and alarms or implement similar functionality that does not rely on the DSC Module.

A more profound option would be replacing the LabVIEW application running on the host computer with an open-source program that would overcome the drawbacks of using NI's system altogether. The already existing hardware including the FPGA oscilloscope and its firmware could be retained and integrated into an

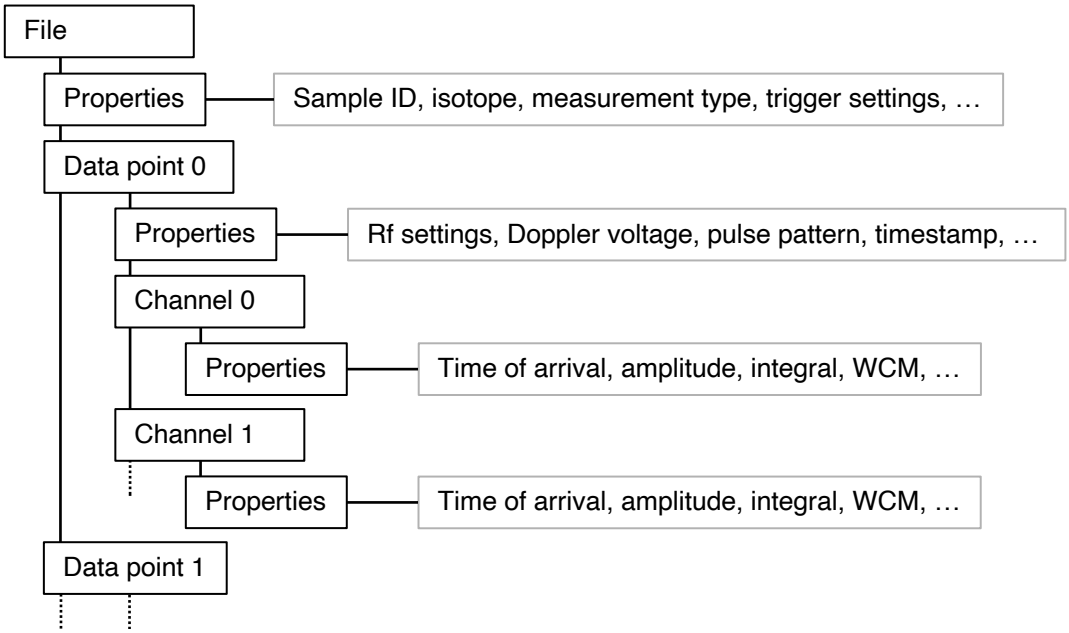

Figure 4.21.: The three-level hierarchy of a TDMS file as used by VCS with the levels file, group and channel among their corresponding properties. Dashed lines indicate repetitive parts.

upgraded DAQ. Software packages allowing such an integration exist in a variety of programming languages and the options to implement such a system, e.g. in Python, have already been evaluated successfully. Such a system would make VITO less dependent on proprietary software and would make VCS more accessible for its users and easier to maintain.

4.4.5. Summary

The centrepiece of the VITO Control System is an FPGA-based oscilloscope that performs a time-resolved characterisation of all detected β particles. Among the determined pulse properties are the time of arrival, amplitude, integral, time over threshold and window coincidence mask. Only these are then streamed to the host computer to minimise the required bandwidth. They enable an in-depth data analysis, thus overcoming the disadvantage of just counting the events, as was done by the previously used MCP. VCS builds on CS++ to integrate all measurement and acquisition devices to keep the system modular and flexible. The measurement implementation follows a producer/consumer pattern generating parameter sets that are handled in a state machine, with one parameter set being equivalent to one measurement step and one iteration of the state machine.

Despite the room for improvements, VCS in its current state is already significantly more potent than the previous system. By characterising all β-particles individually, it enables new features for the data analysis, especially for time-dependent, relaxing signals that can now be recorded without losing valuable information. Measurements of isotopes with unknown relaxation times are thus facilitated. Chapter 5 showcases the extensive possibilities VCS offers for an in-depth data analysis of time-dependent signals.

5. Experimental results

The following chapter presents the preparations, analysis and results of the experiments conducted for this thesis. Measurements of the hyperfine structure and β-NMR studies of ^{47}K implanted into cubic crystals and ionic liquids took place during three beam times. An overview on the experimental details and the preparations is given in Section 5.1. After presenting the processing of the HFS measurements and the reference probe's FIDs, the prime focus of Section 5.2 lays on the possibilities the new data acquisition VCS has to offer for the analysis of the β-NMR measurements. Besides the common one-dimensional fits along the frequency axis, an additional way of representing the data in two dimensions along the frequency and the time axes is introduced. What follows is the analysis of the β-NMR spectra that concludes with the determination of the differential hyperfine anomaly $^{39}\Delta^{47}$ between ^{39}K and ^{47}K in Section 5.4 and the magnetic dipole moment $\mu(^{47}\mathrm{K})$ in Section 5.5.

5.1. Experimental details

The results shown in this thesis are based on β-NMR studies of ^{47}K that took place at the VITO setup during three beam times in May, July and November 2022 in the scope of ISOLDE experiment IS666 [67, 68]. This section gives an overview on the experimental details.

Production of the polarised beam

All beam times used UC_x targets on which impinged 3.3×10^{13} protons per bunch at an energy of $1.4\,\mathrm{GeV}$. About $1 \times 10^7\,\mathrm{ions/\mu C}$ of ^{47}K ($I^\pi = 1/2^+$, $t_{1/2} = 17.5\,\mathrm{s}$) were produced. The radioactive K atoms were surface-ionised in the target station and accelerated to an energy of $50\,\mathrm{keV}$ before being separated by ISOLDE's High Resolution Separator. Considering the half-life, only one proton bunch was taken per PSB super-cycle, equivalent to a spacing of about $40\,\mathrm{s}$. Stable K was filled into the charge exchange cell and heated to a temperature of $150\,^\circ\mathrm{C}$, which causes it to vaporise and neutralise the passing ^{47}K ion beam. A tunable MATISSE Ti:Sa laser was used for optical pumping of the D_2 line ($3p^6 4s\ ^2S_{1/2} \rightarrow 3p^6 4p\ ^2P_{3/2}$) to generate the nuclear spin polarisation. It was set to a wave number of $13\,062.631\,\mathrm{cm}^{-1}$ ($\lambda \approx 765.54\,\mathrm{nm}$) with a power of up to $25\,\mathrm{mW}$ entering the beamline. The timings of the beam gate and ISCOOL provided through the VCS pulse pattern generator were varied during the beam times, depending on whether ISCOOL was used for bunching or not. Most commonly, when bunching was not applied, the beam gate was set to open $6\,\mathrm{ms}$ after the arrival of the proton trigger and it remained open for $500\,\mathrm{ms}$. In the case of using a bunched beam, the beam gate opened after $6\,\mathrm{ms}$ for $500\,\mathrm{ms}$ and ISCOOL released the beam towards VITO for $10\,\mathrm{ms}$ at a time of $510\,\mathrm{ms}$ after the proton pulse. The laser shutter was continuously open when a measurement was running.

Samples

Two different types of samples were used for the measurements, namely cubic crystals and room temperature ionic liquids (RTILs). Cubic crystals have no electric field gradient at the substitutional site and the nuclei implanted into such sites thus show relatively long relaxation times, typically in the order of seconds due to the absence of quadrupolar interaction [1]. RTILs are liquids consisting of ions and can be thought of as liquid salts [8, 79]. They have a very low vapour pressure and are thus suitable for applications in vacuum, i.e.

they do not noticeably evaporate at the pressure of $10^{-5}\,\mathrm{mbar}$ present in the VITO beamline. In comparison to cubic crystals, they show shorter relaxation times.

The two types of samples fulfil different purposes: First, cubic crystals are used to optimise the optical pumping conditions with HFS scans to maximise the nuclear spin polarisation and in return the created β decay asymmetry. For β-NMR measurements, they allow to coarsely determine the Larmor frequency of the probe nuclei due to a high β decay asymmetry and broad resonances that are relatively simple to locate. Second, ionic liquids are used for high-precision β-NMR measurements. The resonances of the liquid lay in the frequency range previously determined by the crystal, but they offer a significantly smaller FWHM due to the molecular tumbling in the liquid averaging out anisotropic effects [105]. Typically, the FWHM of β-NMR spectra in liquids is two orders of magnitude smaller than in a crystal, see e.g. Figure 5.8. RTILs can therefore be exploited to pin down the Larmor frequency ν_L of ^{47}K in its environment with great precision.

For the experiments presented here, the used crystals are KCl with the dimensions $10\,\mathrm{mm}$ by $10\,\mathrm{mm}$ by $1\,\mathrm{mm}$. They are polished on the side facing the beam and glued to a sample holder. The ionic liquid is 1-Ethyl-3-methyl-imidazolium dicyanamide (EMIM-DCA). Because of EMIM-DCA being hygroscopic, the samples were degassed over the course of at least $24\,\mathrm{h}$ in preparation for the beam times to remove any water contamination. One sample is a $15\,\mu\mathrm{L}$ droplet that is brought onto sample holder made out of a mica sheet using a pipette, see Chapter 4.3.1. The mica sheet does not significantly attenuate the emitted β particles. It shows no clear β-NMR resonance that could interfere with the measurements of ^{47}K.

Measurement procedures

A brief overview on the measurement procedures is given at this point. Several hyperfine structure measurements were conducted, scanning the Doppler tuning voltage and evaluating different laser light polarisations to determine the conditions that maximise the nuclear spin polarisation. Laser saturation curves were also acquired to verify that the laser light saturates the transitions for optical pumping to yield the highest polarisation. β-NMR measurements were then acquired with different amplitudes of the applied B_1 field to obtain rf saturation curves that allowed adjusting the rf power accordingly for the remainder of the experiment to avoid power broadening. This was followed by the measurements of the Larmor frequencies ν_L of ^{47}K in the respective environment. Most of the measurements utilised the VCS option to shuffle the frequency steps in order to avoid asymmetric peak broadening, see Chapter 4.4.3. VCS was always set to record the β events of one measurement step for $17\,\mathrm{s}$, starting from the proton bunch impinging the target. This was the maximum duration possible with that configuration of VCS. All high-precision β-NMR measurements were repeated multiple times on a number of EMIM-DCA samples to ensure the reproducibility of ν_L. The ^{2}H reference probe was used to obtain the magnetic field B_0 at the time of the respective β-NMR measurements.

5.2. Preparation and processing of the β-NMR measurements

This section describes the preparations for the β-NMR measurements as well as the processing of the recorded spectra. A short overview is first given on the hyperfine structure measurements used to establish suitable optical pumping conditions. This is followed by the FIDs recorded with the ^{2}H probe that allow for a precise determination of the magnetic field B_0 at the time of the β-NMR measurements. The time-resolved data acquisition VCS enables new analysis approaches for the β-NMR data, two of which are shown here: First, a conventional, one-dimensional representation of the spectra along the frequency axis is presented. Second, a more sophisticated approach is introduced which exploits the time-resolved data recorded with VCS to perform two-dimensional fits along the frequency and the time axes to take the relaxation of the signal into account.

5.2.1. Establishing optical pumping conditions

One of the main objectives of the first beam time in May 2022 was to establish suitable optical pumping conditions that would maximise the nuclear spin polarisation as a prerequisite for the upcoming β-NMR measurements. To do so, the β decay asymmetry was acquired in numerous HFS scans as a function of the Doppler tuning voltage. The orientation of the λ/4-plate was varied to evaluate the dependency of the β decay asymmetry on the laser light being σ^+ or σ^- polarised. Once the orientation of the λ/4-plate that maximises the β decay asymmetry was found, it was fixed and remained in that position for all experiments with ^{47}K.

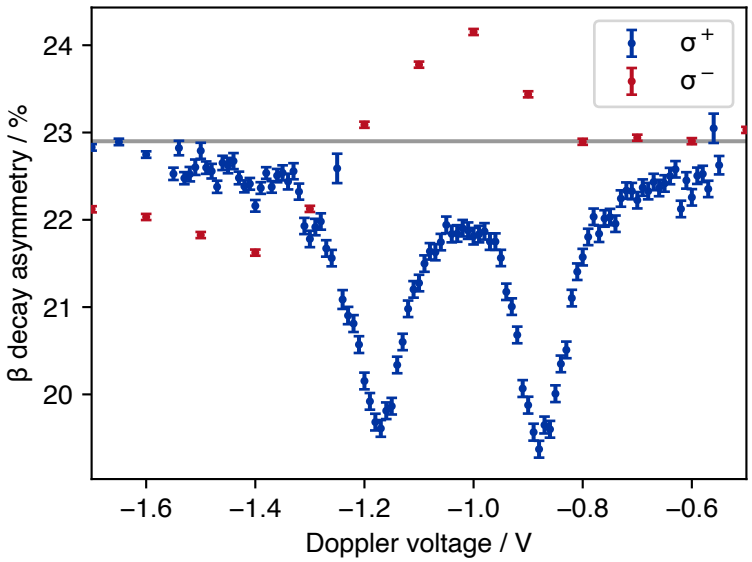

Figure 5.1.: Hyperfine structure measurement of the D_2 line ($3p^6 4s\ ^2S_{1/2} \rightarrow 3p^6 4p\ ^2P_{3/2}$) of ^{47}K with the polarisation of the laser light being σ^- and σ^+. The maximum β decay asymmetry with respect to the baseline, shown in grey, is observed for σ^+-polarisation at a Doppler tuning voltage of $-0.89\,\mathrm{V}$.

Figure 5.1 shows two example measurements of the hyperfine structure with σ^- and σ^+ polarisation of the laser light. The amplitude of the β decay asymmetry with respect to the baseline at about $22.9\,\%$, indicated in grey in the figure, differs for the two polarisations. While the amplitude for σ^- is about $1.5\,\%$ with respect to the baseline at Doppler tuning voltages of $-1.4\,\mathrm{V}$ and $-1.0\,\mathrm{V}$, σ^+ polarisation indicates a higher amplitude of about $3.4\,\%$ at a Doppler tuning voltage of $-0.89\,\mathrm{V}$. The β-NMR studies presented in this thesis were therefore using σ^+ polarisation. A laser power saturation curve was also recorded for this polarisation, with the aim to verify that the transition is saturated and the β decay asymmetry is maximised. When the optimum Doppler voltage and laser power were found, they were set for the following β-NMR experiments and regularly checked during the beam time. They were modified to retain the highest-possible nuclear spin polarisation when necessary. For the following ^{47}K beam times in July and November 2022, the orientation of the λ/4 plate remained unchanged to continue with σ^+ polarisation, while the HFS measurements and the laser saturation curves were repeated.

The Doppler tuning voltage, as seen in Figure 5.1, can be easily converted into the laser frequency perceived by the passing atoms with the relativistic Doppler equation, see Section 3.2.1, e.g. in order to evaluate isotope shifts in laser spectroscopy. More information on this can be found in [45]. In the scope of this thesis, however, the HFS measurements are only used to establish and maximise the nuclear spin polarisation for the β-NMR measurements. No further processing of the recorded hyperfine structures is therefore conducted at this point.

5.2.2. Determining the magnetic field B_0

Described here is the processing of the FID signal from the ^{2}H reference probe to infer the magnetic field B_0 for the subsequent β-NMR measurements with great precision. As explained in Section 3.1.1, the reference probe circuit yields two signal components, which can be considered as the real and the imaginary parts $\mathrm{Re}(f(t)) = a(t)$ and $\mathrm{Im}(f(t)) = b(t)$ of a complex FID signal $f(t) = a(t) + ib(t)$. An example of such a signal $f(t)$ is shown in Figure 5.2a. Due to slight imperfections in the electronic circuit, both components have a DC offset and their amplitudes are not identical. This needs to be corrected before further processing of the signal, otherwise the DC offset would appear as a $0\,\mathrm{Hz}$ frequency component in the spectrum and the difference in signal amplitude would affect the ratio of the components in the spectrum. The offsets $\bar{a}$ and $\bar{b}$ are therefore subtracted from $a(t)$ and $b(t)$, respectively, before normalising the signal components to the same integral $\Sigma a^2_{\mathrm{norm}}(t) = \Sigma b^2_{\mathrm{norm}}(t)$ with $a_{\mathrm{norm}}(t) = a(t)$ and $b_{\mathrm{norm}}(t) = b(t)\sqrt{\Sigma(a(t))^2/\Sigma(b(t))^2}$.

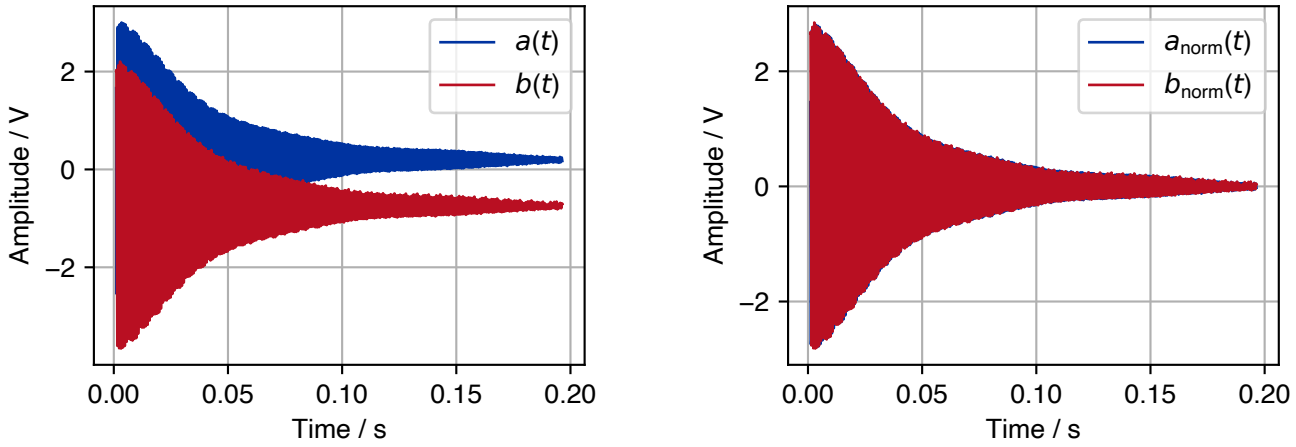

(a) Raw signal.

(b) Offset removed and signal normalised.

Figure 5.2.: Processed FID measured with the ^{2}H reference probe. The components coming from the quadrature detection circuit (see Section 4.3.2), are treated as the real part $a(t)$ and the imaginary part $b(t)$ of the signal. Left: raw, unprocessed data. Right: Offset removed and signals normalised to the same integral.

Figure 5.2b shows the normalised signal. It has a finite length and is not periodic. A so-called leakage effect can thus occur when the signal is Fourier transformed, which would lead to a frequency spectrum that does not represent the frequency components of the signal correctly [69, 19]. To tackle this issue, it is possible to apply a window function to a time signal which forces it to take the value 0 at the beginning and the end. Doing that yields a quasi-periodic signal that can be Fourier transformed with minimised leakage. Note that not applying a window function to the time signal in Figure 5.2b is equivalent to applying a rectangle window. With the Fourier transform of a rectangle being a sinc function, this causes side lobes in the spectrum around the actual frequency components [19]. To minimise this effect, a Hann window is applied to the signal components of the reference probe. The windowed signal is then extended in the time domain by adding zeros before applying the Fourier transform to obtain the frequency spectrum. While this so-called zero padding does not add any additional information to the signal in the time domain nor in the frequency domain, it does improve the apparent frequency resolution, i.e. the spectrum is 'smoother'. An actually higher frequency resolution can only be achieved by recording the time signal for longer.

A Fast Fourier Transform (FFT) algorithm is utilised to obtain the frequency spectrum, which is shown in Figure 5.3a. The envelope of the signal in the time domain determines the peak shape in the spectrum

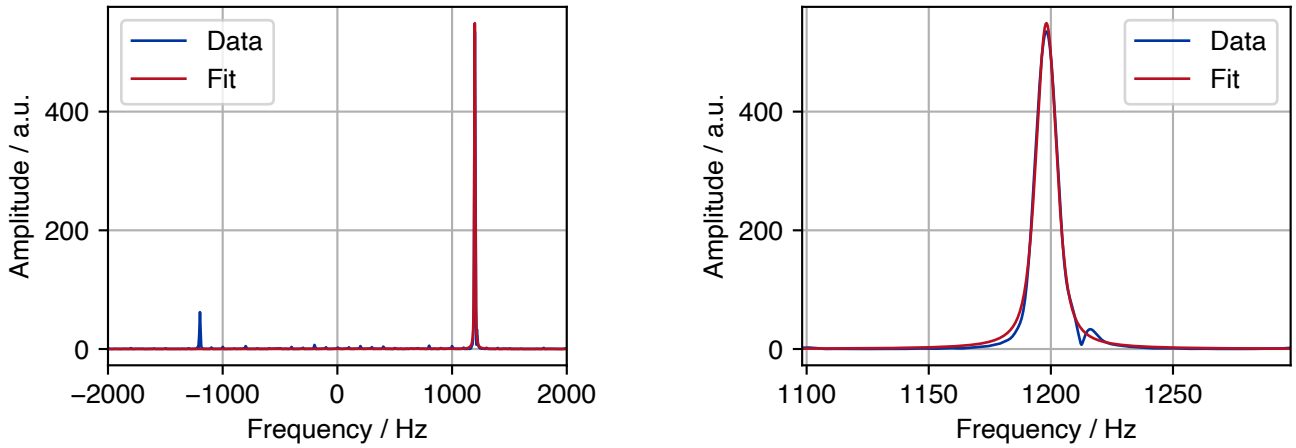

(a) Full spectrum.

(b) Zoomed in on the predominant frequency.

Figure 5.3.: The frequency spectrum corresponding to the data shown in Figure 5.2. (a) relevant part of the full spectrum, including a fit of the predominant frequency component with a Lorentzian. (b) zoomed in on this frequency range at around $1200\,\mathrm{Hz}$.

because the two form a Fourier pair. In this concrete case, the time signal's envelope can be approximated by an exponential function, which results in the frequency peaks taking roughly the shape of a Lorentzian function. The oscillations underneath the envelope of the time signal determine the position of the peaks in the spectrum. As visible in Figure 5.3a, the main frequency components are at around $\pm 1200\,\mathrm{Hz}$. Lower frequency components are also present in the spectrum, indicative in the form of a beating of the signal in the time domain, but these components are negligible compared to the predominant signal components. Note that the tail of the FID signal was not fully recorded, see Figure 5.2a, also contributing to the envelope of the signal not being an ideal exponential. In return, the peaks in the spectrum do not take ideal Lorentzian line shapes, evident in the form of side lobes, though this issue is mostly diminished by applying the window function to the data.

With the input signal treated as complex, the phase between the real and the imaginary part can be determined and becomes apparent in the components at around $\pm 1200\,\mathrm{Hz}$ having different amplitudes, with the predominant frequency component being around $+1200\,\mathrm{Hz}$. Subsequently, only this peak is fitted with a Lorentzian to obtain ν_{fit}, see Figure 5.3. The Larmor frequency $\nu^{^2\mathrm{H,\,D_2O}}$ of the ^{2}H reference probe is then computed via

$$\nu^{^2\mathrm{H,\,D_2O}} = \nu_{\mathrm{carrier}} - \nu, \tag{5.1}$$

with ν_{carrier} being the carrier frequency set on the rf generator, see Equation (3.10) in Section 3.1.1.

5.2.3. One-dimensional fitting along the frequency axis

The acquired β-NMR spectra need to be processed in order to obtain the Larmor frequency ν_{L} of the respective nucleus in its environment, here ^{47}K in a KCl crystal or in the ionic liquid EMIM-DCA. Typically, β-NMR resonances are shown with the β decay asymmetry as the function of the frequency ν of the applied field B_1, integrated over a defined observation time window. In order to obtain better statistical significance of such a one-dimensional resonances, one may try to extend the acquisition duration of each frequency step which results in the detection of more β events and thus more statistics. However, the nuclear spin polarisation is time-dependent and relaxes over time, as described in Section 3.1.2. Integrating over a longer period of time will therefore at some point be disadvantageous when the signal of interest has relaxed. The additional β

particles would no longer contribute to the β-NMR signal and thus diminish the statistical significance. This should be taken into account when recording and analysing the resonances. It is therefore crucial to determine an observation time window that represents a compromise between the amplitude of the signal which relaxes with T_1, thus preferring short observation windows, and the number of β events to consider more statistics, thus preferring longer observation windows.

The old data acquisition system required the observation time window to be set to a fixed value during the experiment. This was a major drawback, e.g. in the case of unknown relaxation times, since optimising the observation window for the relaxation time was not possible in the post processing of the data. The new data acquisition VCS resolves this problem. As described in Section 4.4, VCS characterises all β events by a number of properties during a maximum acquisition time of 17 s per frequency step. Among these pulse properties is the time of arrival of the β particles. It is therefore not required by the user to specify an observation time window a priori, regardless of the relaxation time. Instead, VCS enables to modify the observation time window in post-processing based on the time of arrival to retain full flexibility during the analysis.

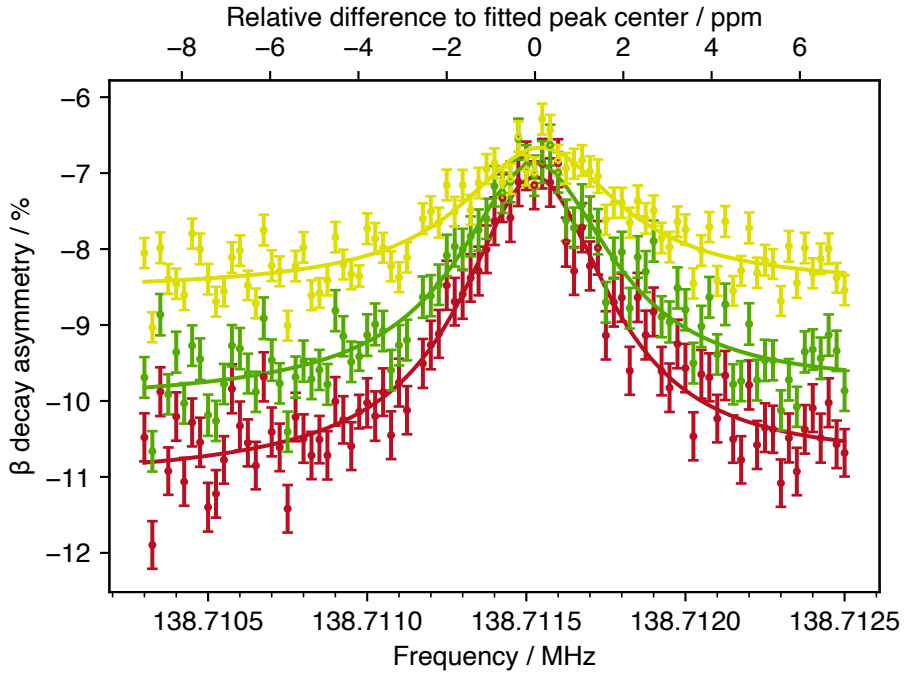

Figure 5.4.: The β decay asymmetry of one β-NMR measurement of ^{47}K in EMIM-DCA shown for different observation time windows: from 0 s to 5.5 s (red), 0 s to 8 s (green) and 0 s to 17 s (yellow). Respective fits with Lorentzian line shapes are also shown. One can see the decreasing amplitude and changing baseline due to the relaxation of the polarisation.

Presented here is a method designed to find the optimum observation time, which represents a compromise between the amplitude of the signal and the number of β events by using the data recorded with VCS. The aim is to minimise the uncertainty of the determined frequency ν_L during the post-processing. Figure 5.4 shows the same β-NMR measurement of ^{47}K implanted into EMIM-DCA but using three different observation time windows that start with the proton trigger at 0 s and have a duration of 5.5 s (red), 8 s (green) and 17 s (yellow). The respective fits were performed under the assumption of a Lorentzian line shape and are depicted in the same Figure. Shorter observation time windows offer higher amplitudes of the resonance but also larger

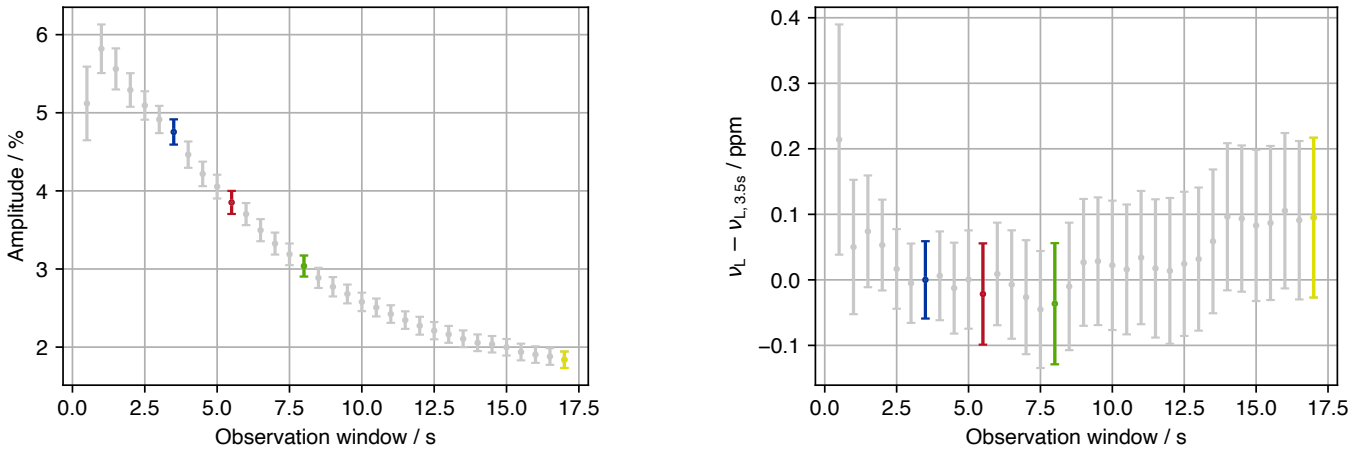

(a) Amplitudes of the fitted peak.

(b) Differences of ν_L of the fitted peak.

Figure 5.5.: The fitted resonance amplitude (a) and the Larmor frequency ν_L (b) for the data from Figure 5.4 as a function of the observation time window since the proton trigger. The Larmor frequencies are shown with respect to $\nu_{L,3.5\,s} = 138\,711\,530(8)\,\mathrm{Hz}$ obtained for an observation window of $3.5\,s$. Highlighted in red, green and yellow is the data corresponding to the three resonances shown in Figure 5.4.

uncertainties in the β decay asymmetry due to fewer β events being taken into account. VCS then enables to evaluate the fit parameters as a function of the observation time window. This is presented in Figure 5.5 for the amplitude and the resonance position, i.e. the Larmor frequency ν_L, of the previously shown data.

It is clearly visible how the relaxation influences the β-NMR resonances by decreasing the amplitude of the β-NMR resonances for longer observation windows. More relevant, however, is its influence on the Larmor frequencies determined with the fits. While the difference between them is a fraction of a ppm and therefore negligible compared to their uncertainty, the uncertainty varies with the observation time. Figure 5.6 shows how the uncertainty $\delta\nu_L$ decreases, reaching a minimum at an observation window of $3.5\,s$, before increasing again. This is the case since extending the observation time will at first include more β events which improves statistics, before the observation time window is so long that it includes more and more β particles for which the signal has already relaxed. The observation window of $3.5\,s$ thus offers the best compromise and allows reaching the smallest uncertainty in the determined Larmor frequency ν_L, with the resulting resonance being plotted in Figure 5.7 for comparison to the other observation windows of $5.5\,s$, $8\,s$ and $17\,s$ from Figure 5.4. In addition, Figures 5.5 and 5.6 also show the respective fit parameters of the $3.5\,s$ observation time window in blue, illustrating that neither the largest amplitude nor the highest number of β events guarantees the most precise determination of the Larmor frequency ν_L. Instead, the approach presented here considers the relaxation of the signal and the number of β events.

All measurements conducted in the scope of this thesis were processed accordingly by choosing the observation time window that minimised the uncertainty in the fitted Larmor frequency ν_L. The resonance of ^{47}K in EMIM-DCA from Figure 5.7 with an observation time window of $3.5\,s$ is shown again in Figure 5.8 together with a ^{47}K resonance recorded in a KCl crystal with an observation time of $7.5\,s$ selected in the same way as that for EMIM-DCA. While the FWHM of the resonance in the crystal is $167(6)\,\mathrm{ppm}$, the ionic liquid offers a FWHM of $3.4(2)\,\mathrm{ppm}$. The uncertainty in the determined Larmor frequency ν_L is $1.6\,\mathrm{ppm}$ for the crystal and $0.06\,\mathrm{ppm}$ for the ionic liquid. The advantages of a lower FWHM and lower uncertainty in the Larmor frequency for EMIM-DCA are caused by the molecular tumbling in the ionic liquid that averages out anisotropic effects, which enables high-precision β-NMR studies.

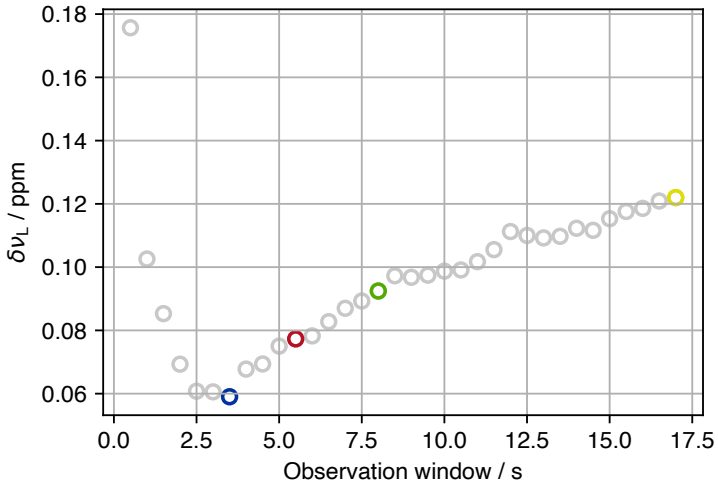

Figure 5.6.: The uncertainty $\delta\nu_\mathrm{L}$ of the Larmor frequency ν_L depending on the observation time window. The data highlighted in red, green and yellow correspond to the three resonances shown in Figure 5.4.

5.2.4. Two-dimensional fitting along frequency and time axes

The approach introduced in the previous section aims to determine an observation time window that offers a compromise between the decreasing amplitude of the signal and the number of considered β events. All events occurring during that time window are integrated to compute the β decay asymmetry. While this method offers the freedom of modifying and systematically optimising the observation window even in post processing, it is still a compromise that comes with two inherent drawbacks. First, it considers only a single time bin per frequency step and integrates over the corresponding β events, which will inevitably discard the relaxation of the signal during that time bin. A one-dimensional fit thus does not represent the signal comprehensively. Second, all β events that do not fall into the observation time window are discarded, therefore removing large proportions of the data set and thus valuable information. Especially in the case of short relaxation times, this results in utilising only a fraction of the recorded data.

Presented here is a second approach which bins the time of arrival of the β events recorded with VCS to obtain the asymmetry as a function of time for each frequency step. The method then applies a two-dimensional fit along the frequency and the time axes of a measurement to consider all β events of the entire data set while taking the relaxation of the signal into account. It then allows to extract additional information on the β-NMR spectrum, such as the relaxation curves or the expected amplitude over time. To illustrate this approach, Figure 5.9 shows a spectrum of ^{47}K in EMIM-DCA. This is the same data set as in the previous section with frequency steps of $25\,\mathrm{Hz}$ and with the time of arrival of the β events being binned in steps of $0.2\,\mathrm{s}$. Note that this bin width of $0.2\,\mathrm{s}$ is taken only for the purpose of a more intuitive visualisation for this thesis, while the fit itself may be executed with smaller bin widths.

Two-dimensional fitting model

Several contributions need to be taken into account to model the change in β decay asymmetry for β-NMR resonances [63]. This model is simplified with the assumption that all polarised nuclei are implanted at the time $t = 0$. The first part to be included in the fitting function is the spin lattice relaxation that represents the ensemble of nuclear spins returning to thermal equilibrium conditions. It is described by an exponential function with the time constant T_1, see Section 3.1.2, and occurs evenly irrespective of the rf frequency ν of the applied B_1 field . An additional time constant T_L needs to be considered as the applied frequency ν approaches the Larmor frequency ν_L of the nuclei. It expresses that the β decay asymmetry relaxes more rapidly and is

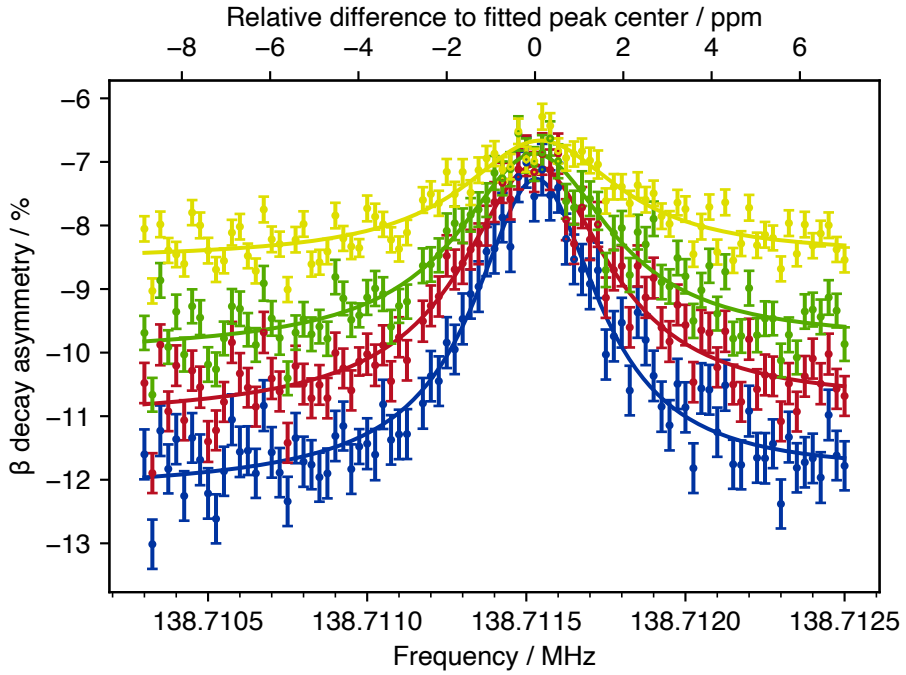

Figure 5.7.: The β decay asymmetry of the measurement from Figure 5.5 is shown again with an additional observation window of $0\,\mathrm{s}$ to $3.5\,\mathrm{s}$ (blue) which offered the lowest uncertainty $\delta\nu_\mathrm{L}$ in the fitted Larmor frequency ν_L.

effectively being 'destroyed' in the resonance case. A Lorentzian function scales this time constant depending on the applied frequency ν to represent the line shape of the β-NMR resonance, thus resulting in the biggest contribution of T_L for $\nu = \nu_\mathrm{L}$ and basically no contribution for $\nu \ll \nu_\mathrm{L}$ and $\nu \gg \nu_\mathrm{L}$. The final component to describe the data is a constant that reflects the instrumental β decay asymmetry to which the signal converges for $t \to \infty$. Following these deliberations, the two-dimensional β-NMR spectra can be described with

$$A(\nu, t) = a e^{-t\left(\frac{1}{T_1} + \frac{w^2}{(\nu-\nu_\mathrm{L})^2+w^2}\frac{1}{T_\mathrm{L}}\right)} + b. \tag{5.2}$$

Here, t is the time, a is the initial β decay asymmetry generated by optical pumping, equivalent to the change asymmetry from $t = 0$ to $t \to \infty$, and T_1 is the time constant of the spin-lattice relaxation characterising the interaction of the nuclear spins with their immediate environment. w is the width of the Lorentzian function that describes the contribution of the time constant T_L depending on the difference between the applied frequency ν and the Larmor frequency ν_L, while the constant b represents the instrumental β decay asymmetry. Summing the two time constants T_1 and T_L yields the time constant $T_\mathrm{on} = (1/T_1 + 1/T_\mathrm{L})^{-1}$ which describes the relaxation in the resonance case of $\nu = \nu_\mathrm{L}$. It is important to ensure that the bin width of the time axis is smaller than the expected time constants. The fitting function is implemented in a Python programme using the LMFIT package [83]. To obtain the statistical uncertainties, the uncertainties from the fits are multiplied with $\sqrt{\chi^2_\mathrm{red}}$. It is worth noting that the fitting routine is only applied to β events that were recorded after the implantation of the isotope beam into the sample had stopped, i.e. when the beam gate is closed or ISCOOL is closed in the case of working with bunched beams. This avoids processing data that is a convolution of β particles emitted from newly implanted, polarised nuclei and those that have already relaxed. In the case of β-NMR with crystals that have a long relaxation time, it may occur that previous isotope bunches contribute to

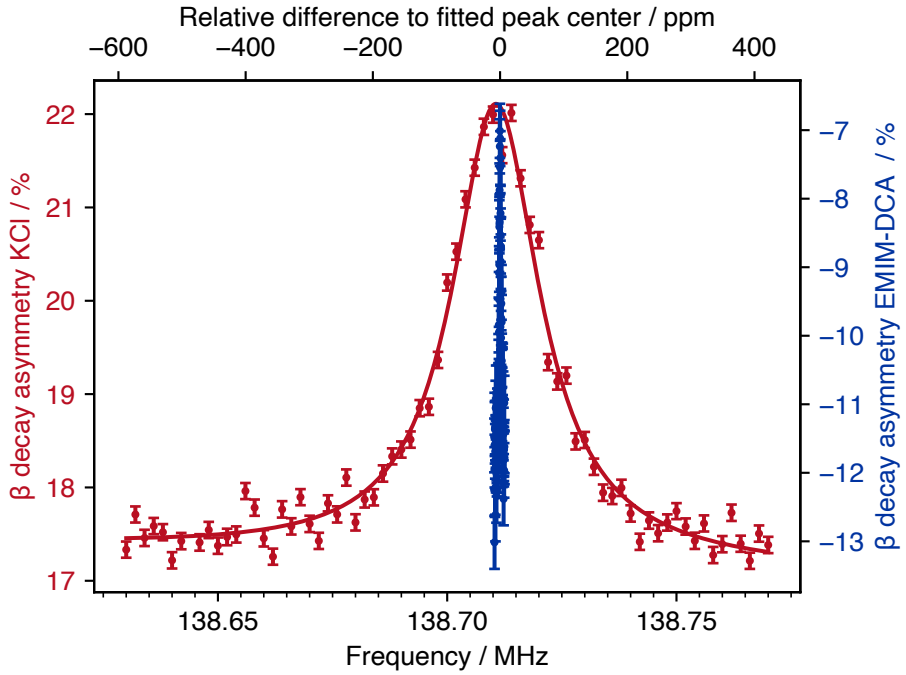

Figure 5.8.: Comparison of a ^{47}K β-NMR resonance in a KCl crystal and the ionic liquid EMIM-DCA during the May 2022 beam time. The resonance in the crystal has a FWHM of $167(6)\,\mathrm{ppm}$ whereas EMIM-DCA has a FWHM of $3.4(2)\,\mathrm{ppm}$.

the recorded signal. This can lead to a change in the baseline asymmetry that can then no longer be described only by the constant b but may require additional terms to reflect this effect in the fitting function.

The two-dimensional fit of the ^{47}K implanted into EMIM-DCA data from Figure 5.9 is depicted in Figure 5.10. As seen here, the residuals of the fit show no structure, indicating that the two-dimensional fit based on Equation (5.2) represents the data set appropriately including the T_1 relaxation and the faster relaxation around the Larmor frequency ν_L. This is also underlined by $\chi^2_\mathrm{red} = 1.03$. An additional example of a β-NMR resonance of ^{47}K in a KCl crystal is on display in Figure 5.11 to illustrate the fitting result in the case of a longer T_1 relaxation. No changes to the fit routine were made apart from adapting the initial fit parameters. The behaviour of the β decay asymmetry is again represented appropriately by the fit with $\chi^2_\mathrm{red} = 1.16$.

Comparison of the one-dimensional and two-dimensional fits

In order to benchmark the two-dimensional fits against their one-dimensional counterparts, the fit results for χ^2_red and the determined Larmor frequencies ν_L are given for ^{47}K in EMIM-DCA in Table 5.1 and for ^{47}K in KCl in Table 5.2. The one-dimensional fits along the frequency axis were executed with observation time windows selected according to Section 5.2.3 and the two-dimensional fits along the frequency and the time axes were conducted as presented in this Section.

In the case of ^{47}K in EMIM-DCA (Table 5.1), the two approaches are in agreement with the deviations between them being smaller than the 1σ uncertainties for most measurements. A lower average χ^2_red and a median uncertainty in the Larmor frequency of $18\,\mathrm{Hz}$ $(0.13\,\mathrm{ppm})$ show benefits of the two-dimensional fits compared to their one-dimensional counterpart that have a median uncertainty of $24\,\mathrm{Hz}$ $(0.17\,\mathrm{ppm})$. Similar differences of up to 1σ are found between the two approaches for β-NMR measurements of ^{47}K in KCl, as listed in Table 5.2. While the one-dimensional fits have a χ^2_red ranging from 1.08 to 5.05 with a median of

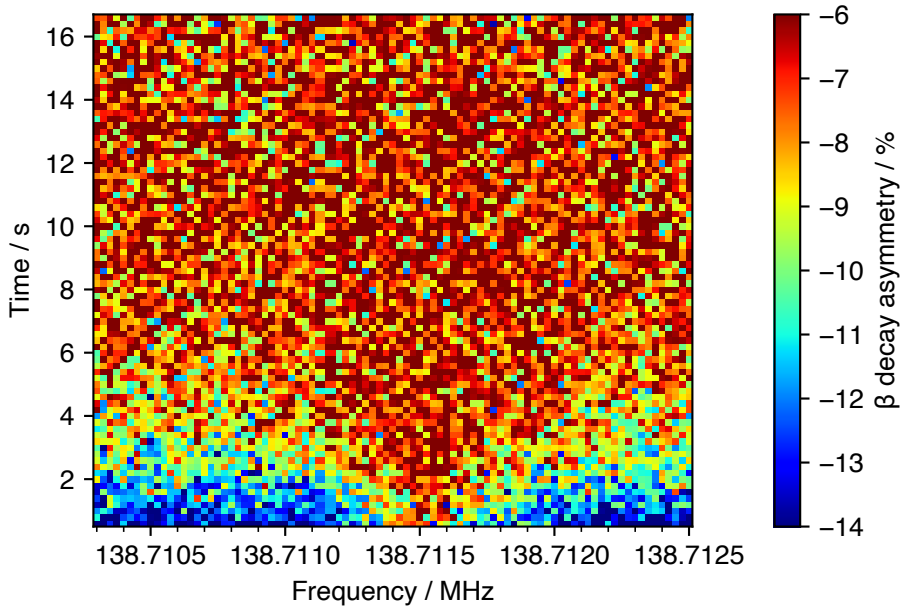

Figure 5.9.: A two-dimensional representation of a β-NMR resonance as a function of frequency and time. Shown here is a measurement of ^{47}K in the ionic liquid EMIM-DCA with frequency steps of $25\,\mathrm{Hz}$ and time bins with a duration of $0.2\,\mathrm{s}$.

2.04, the two-dimensional routine offers significantly more consistent results with a median χ^2_{red} of 1.1. This is also expressed in the median uncertainty which is $117\,\mathrm{Hz}$ $(0.8\,\mathrm{ppm})$ for the two-dimensional fits as opposed to $223\,\mathrm{Hz}$ $(1.6\,\mathrm{ppm})$ for the one-dimensional fits. The two-dimensional approach is hence favourable as it leads to a higher consistency in fitting the β-NMR resonances and lower uncertainties. The differences between the two approaches can be explained with the ability of the two-dimensional fits to reproduce the line shape of the β decay asymmetry using both its frequency and time dependency. This aspect is discussed in more detail later on.

Three-dimensional visualisation

In order to gain a better understanding of the two-dimensional fits and their line shape, they are now visualised in three dimensions, with the β decay asymmetry as a function of the applied frequency ν and the time t. Figure 5.12 shows such representation of the data sets from Figures 5.10 and 5.11 for ^{47}K implanted into EMIM-DCA and KCl. While only the β events recorded after the isotope beam implantation had stopped are considered for the fit, here $0.6\,\mathrm{s}$ for EMIM-DCA and $3\,\mathrm{s}$ for KCl, this three-dimensional plot illustrates the expected β decay asymmetry from $0.1\,\mathrm{s}$ to $17\,\mathrm{s}$. The wire mesh in the form of black lines across the surface plot serves as a guidance for the viewer. It indicates the course of the fit along the time axis for the Larmor frequency ν_{L} and along the frequency axis for $t = 0.5\,\mathrm{s}$, $t = 1\,\mathrm{s}$ as well as t being one of the ticks of the time axis.

The line shape is first similar to a Lorentzian function, see Figure 5.12, when the applied rf interacts with the nuclear spins and causes a faster relaxation in the resonance case ($\nu \approx \nu_{\mathrm{L}}$). As the polarisation is being 'destroyed' by the rf, the β decay asymmetry converges towards the instrumental asymmetry b (see Equation (5.2)) when the nuclear spins have relaxed and the resonance broadens. This has an effect on the line shape, which can then be described as a saturated Lorentzian that establishes a plateau. While the background ($\nu \ll \nu_{\mathrm{L}}$ and $\nu \gg \nu_{\mathrm{L}}$) relaxes with T_1 and converges towards b, the resonance continues to broaden and the plateau becomes more pronounced. The change in β decay asymmetry across this plateau is

Table 5.1.: Comparison of χ^2_{red} and the Larmor frequencies ν_{L} obtained with the one-dimensional fits and the two-dimensional fits for ^{47}K in EMIM-DCA.

Timestamp	SampleID	$\chi^2_{\mathrm{red,1d}}$	ν_{1d} / Hz	$\chi^2_{\mathrm{red,2d}}$	ν_{2d} / Hz
20220522-011603	EP1_K47_NMR_5	1.02	138 711 585(17)	1.02	138 711 540(14)
20220522-025524	EP1_K47_NMR_7	1.02	138 711 592(33)	1.00	138 711 608(44)
20220522-032022	EP1_K47_NMR_8	1.04	138 711 527(25)	1.02	138 711 522(24)
20220522-034518	EP1_K47_NMR_9	1.25	138 711 558(30)	1.03	138 711 540(23)
20220522-045844	EP1_K47_NMR_13	1.14	138 711 551(22)	1.02	138 711 538(17)
20220522-062619	EP1_K47_NMR_14	1.09	138 711 501(20)	1.01	138 711 526(15)
20220523-075809	EP2_K47_NMR_1	1.17	138 711 538(13)	1.04	138 711 541(9)
20220523-090149	EP2_K47_NMR_2	1.14	138 711 530(8)	1.03	138 711 529(7)
20220714-223719	EP1_NMR_008	1.05	138 710 533(29)	1.01	138 710 522(26)
20220715-000047	EP1_NMR_009	1.17	138 710 582(48)	1.00	138 710 524(41)
20220715-002510	EP1_NMR_010	1.22	138 710 591(40)	0.97	138 710 604(30)
20220715-005209	EP1_NMR_011	1.89	138 710 528(45)	1.05	138 710 558(46)
20220715-011631	EP1_NMR_014	1.26	138 710 571(20)	1.05	138 710 571(19)
20220715-025208	EP1_NMR_015	1.17	138 710 607(21)	1.06	138 710 630(21)
20221123-061849	K47_mica_E1_NMR001	1.08	138 710 674(28)	1.06	138 710 707(19)
20221123-063419	K47_mica_E1_NMR003	1.73	138 710 658(24)	1.01	138 710 676(12)
20221123-065249	K47_mica_E1_NMR004	1.33	138 710 592(10)	1.13	138 710 626(8)

Table 5.2.: Comparison of χ^2_{red} and the Larmor frequencies ν_{L} obtained with the one-dimensional fits and the two-dimensional fits for ^{47}K in KCl.

Timestamp	SampleID	$\chi^2_{\mathrm{red,1d}}$	ν_{1d} / Hz	$\chi^2_{\mathrm{red,2d}}$	ν_{2d} / Hz
20220521-190257	KCl_K47_NMR24	5.05	138 710 635(223)	1.16	138 710 477(78)
20220521-195430	KCl_K47_NMR25	1.08	138 710 666(187)	1.11	138 710 309(117)
20220521-202957	KCl_K47_NMR26	3.22	138 710 421(236)	1.10	138 710 592(115)
20220521-204508	KCl_K47_NMR27	1.95	138 710 197(213)	1.12	138 710 402(111)
20220521-210021	KCl_K47_NMR28	1.19	138 710 821(150)	1.08	138 710 636(121)
20220521-211558	KCl_K47_NMR29	3.46	138 710 589(331)	1.07	138 710 538(126)
20220521-213107	KCl_K47_NMR30	2.04	138 710 940(306)	1.06	138 710 628(225)

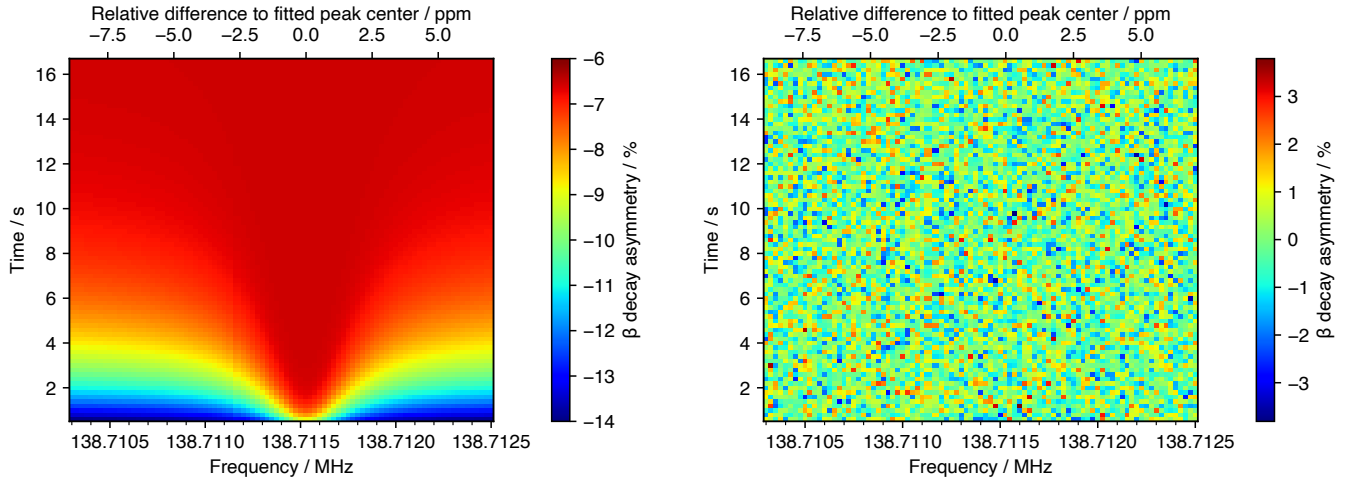

(a) Two-dimensional fit.

(b) Residuals of the fit.

Figure 5.10.: Two-dimensional fit (a) and the corresponding residuals (b) of the β-NMR resonance of ^{47}K in EMIM-DCA shown in Figure 5.9 as a function of frequency and time.

negligible. It is essential to take this line shape into account when analysing the two-dimensional fits of the β-NMR resonances. To obtain a better understanding of the line shape, the following Sections assess it in more detail by considering projections of the fit along the time and the frequency axes, similar to the wire mesh indicated in Figure 5.12. These projections then enable a more intuitive evaluation of the parameters of the β-NMR resonance, such as the relaxation, the amplitude and the FWHM.

Relaxation times

Projecting the two-dimensional fits along the time axis for constant frequencies gives direct access to the relaxation curves of the acquired β-NMR spectra. The two cases considered here are the relaxation 'off resonance' ($\nu \ll \nu_\mathrm{L}$ and $\nu \gg \nu_\mathrm{L}$) and 'on resonance' ($\nu = \nu_\mathrm{L}$), whose corresponding time constants T_1 and $T_\mathrm{on} = (1/T_1 + 1/T_\mathrm{L})^{-1}$ can be obtained directly from the fitting parameters, see Equation (5.2). As mentioned, only the β events detected after the implantation into the sample has stopped are considered for the fits. It is hence beneficial to work with bunched isotope beams to ensure a simultaneous implantation of all nuclei into the sample. If this is done, all β events can be taken into account for the fit to yield a more precise determination of the relaxation.

Figure 5.13 shows the relaxation curves on and off resonance for ^{47}K in EMIM-DCA and KCl, with the shaded areas in the plots illustrating the 1σ uncertainties. Seen here are clear differences in the relaxation depending on the host of ^{47}K. The relaxation time off resonance is significantly shorter for EMIM-DCA ($T_1 = 3.0(1)\,\mathrm{s}$) than for the KCl crystal ($T_1 = 22.7(4)\,\mathrm{s}$). In the resonance case of $\nu = \nu_\mathrm{L}$, the additional contributions to the time constant T_1 for EMIM-DCA and KCl take values of $T_\mathrm{L} = 0.51(7)\,\mathrm{s}$ and $T_\mathrm{L} = 0.57(11)\,\mathrm{s}$, respectively. This results in the constants $T_\mathrm{on} = (1/T_1 + 1/T_\mathrm{L})^{-1} = 0.43(5)\,\mathrm{s}$ for EMIM-DCA and $T_\mathrm{on} = 0.56(10)\,\mathrm{s}$ for KCl describing the relaxation on resonance. It is then computed at what time $t_{0.98}$ the resonances are saturated to a factor of 0.98, i.e. $A(\nu_\mathrm{L}, t_{0.98}) = 0.98A(\nu_\mathrm{L}, t = 0)$. This is the case at $t_{0.98} = 1.7(2)\,\mathrm{s}$ for EMIM-DCA and $t_{0.98} = 2.2(4)\,\mathrm{s}$ for KCl. The change of the β decay asymmetry is negligible for $t > t_{0.98}$, as seen in Figure 5.13, meaning that effectively the entire nuclear spin polarisation has been destroyed and the resonance is saturated. This is equivalent to the β decay asymmetry reaching a plateau in the three dimensional representation in Figure 5.12.

Another observable that can be extracted from the two-dimensional fits is the amplitude of the β-NMR resonances, which can be computed as the difference of the relaxation curves on and off resonance with

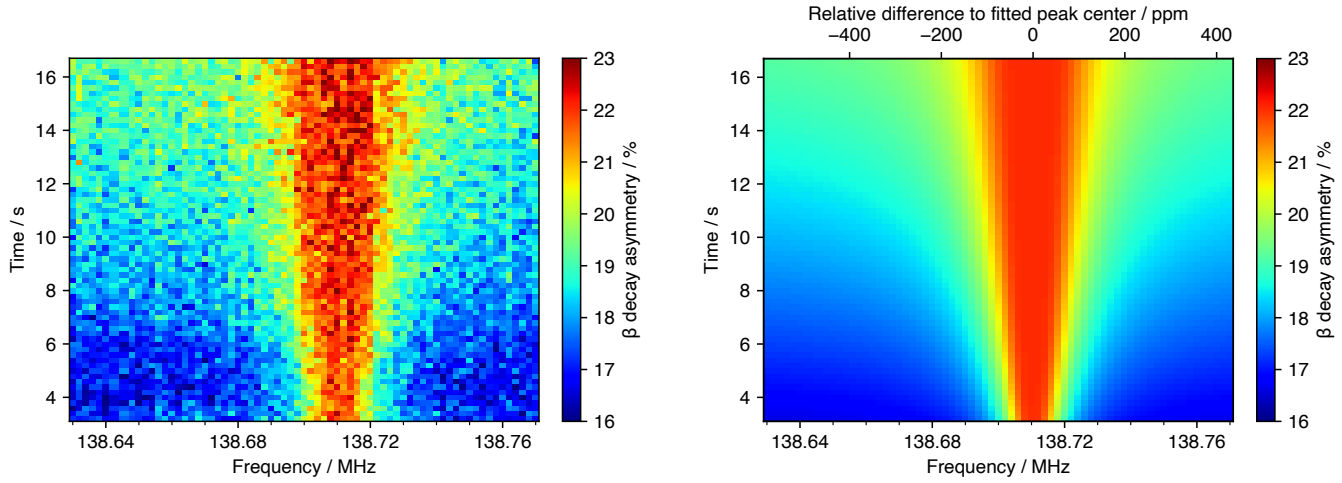

(a) Two-dimensional data.

(b) Two-dimensional fit.

Figure 5.11.: A two-dimensional β-NMR measurement of ^{47}K implanted into a KCl crystal (a) and the corresponding fit (b) as a function of frequency and time.

their time constants T_{on} and T_1. The amplitude of the resonances is thus also time-dependent, as shown in Figure 5.14 for the measurements of ^{47}K in EMIM-DCA and KCl. These plots are helpful to determine e.g. the maximum amplitude that can be observed for a β-NMR resonance. Being aware of the initial β decay asymmetry generated through optical pumping, cf. parameter a in Equation (5.2), this knowledge can be utilised to optimise the rf amplitude, see Section 5.3.1. The two-dimensional fits thus add valuable information compared to their one-dimensional counterpart by yielding the relaxation times of the β-NMR measurements as well as the amplitude of the signal over time.

Line shape

As seen in the three-dimensional representations in Figure 5.12, the line shape of the β-NMR resonances changes over time. In order to assess the evolution of the line shape and judge how representative it is of the underlying data, projections of the two-dimensional fits are now evaluated along the frequency axis for different times t.

Figure 5.15 shows three projections of the β-NMR resonance of ^{47}K in EMIM-DCA and another three for ^{47}K in KCl, with the black lines indicating the amplitude at the half maximum and the shaded areas depicting the relevant 1σ uncertainties. The lowest times of $t = 1.0\,\mathrm{s}$ for EMIM-DCA and $t = 2.1\,\mathrm{s}$ for KCl are depicted since this is when respective β-NMR resonances reach their maximum amplitudes, see Figure 5.14, while the other times t of the projections are chosen to illustrate how the line shape evolves over time. The line shape can initially be approximated as a Lorentzian function when the resonance reaches its maximum amplitude at $t = 1.0\,\mathrm{s}$ and $t = 2.1\,\mathrm{s}$ for EMIM-DCA and KCl, respectively. A substantial broadening of the β-NMR resonance of ^{47}K in EMIM-DCA is observed at $3.0\,\mathrm{s}$. This is consistent with the nuclear spins having effectively relaxed after $t_{0.98} = 1.7(2)\,\mathrm{s}$ in the resonance case, resulting in the plateau to prevail for later points in time. With the background continuing to relax with the time constant T_1, it is apparent that the amplitude of the resonance is significantly diminished after $8.0\,\mathrm{s}$ and the plateau dominates the line shape. For KCl, the maximum amplitude at $t = 2.1\,\mathrm{s}$ again takes a shape close to a Lorentzian function. Given that $t_{0.98} = 2.2(4)\,\mathrm{s}$ for KCl, it is clear that the resonance has saturated for the times $7\,\mathrm{s}$ and $16\,\mathrm{s}$ when severe broadening is visible. The resonance still shows a significant amplitude even after $16\,\mathrm{s}$ though, which is due to the longer T_1 relaxation for KCl compared to EMIM-DCA.

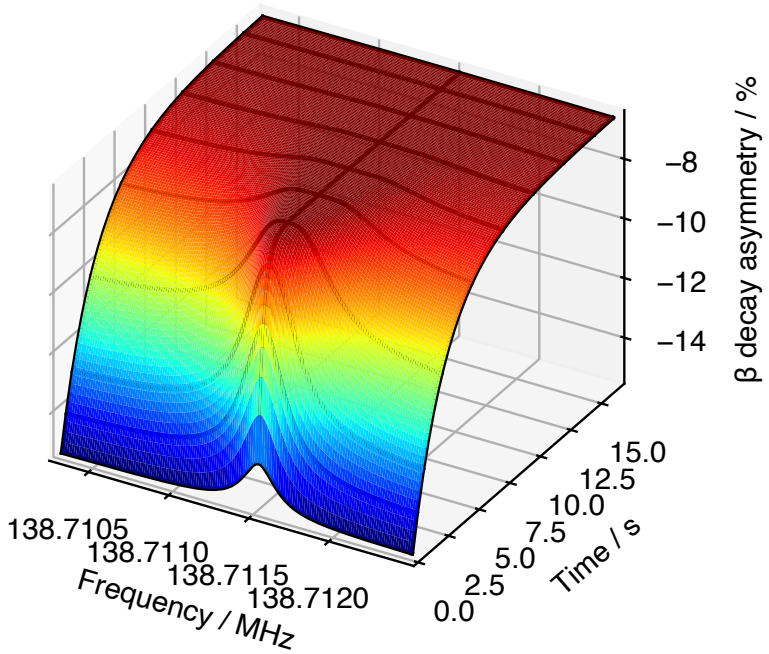

(a) ^{47}K in EMIM-DCA.

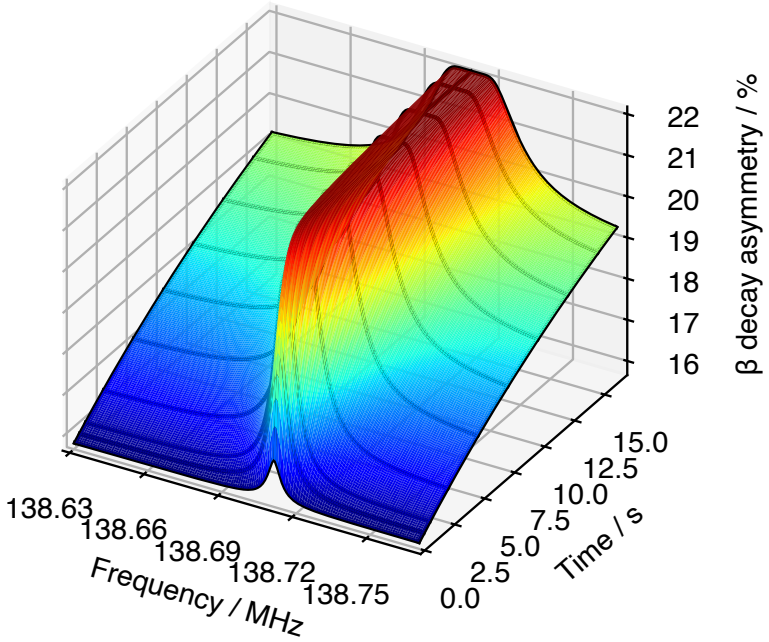

(b) ^{47}K in KCl.

Figure 5.12.: Three-dimensional representations of the fits of the β-NMR measurements of ^{47}K in (a) EMIM-DCA (see Figure 5.10) and (b) KCl (see Figure 5.11), with the β decay asymmetry as a function of frequency and time. The black wire mesh serve as guidance at the determined Larmor frequency ν_{L} and along the time axis.

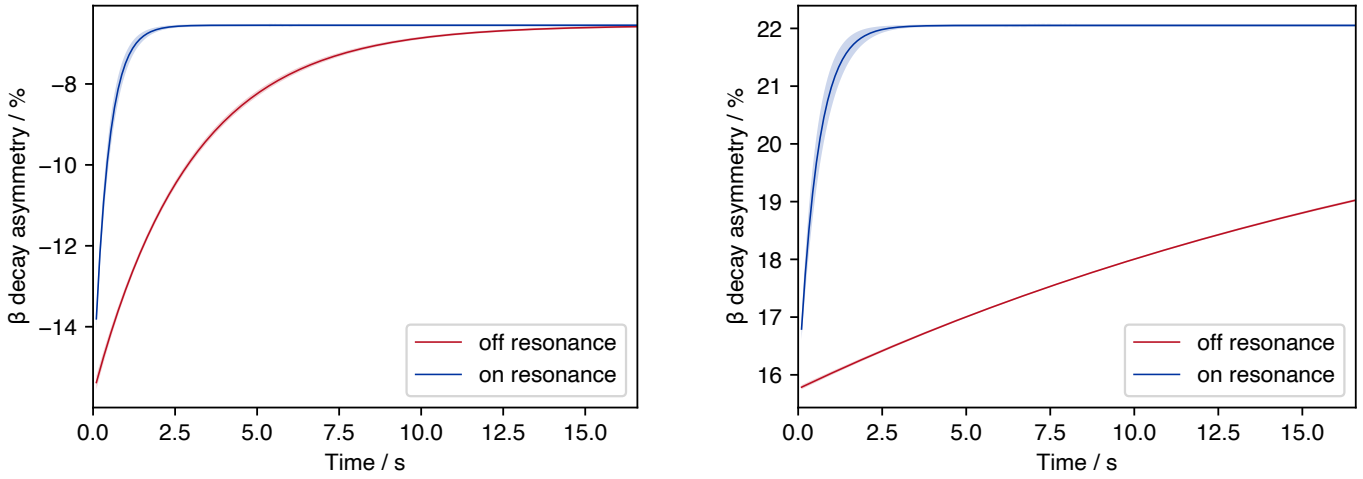

(a) ^{47}K in EMIM-DCA.

(b) ^{47}K in KCl.

Figure 5.13.: The relaxation of the two-dimensional fit of the β-NMR resonance of ^{47}K implanted into (a) EMIM-DCA and (b) KCl from Figures 5.10 and 5.11 evaluated for two different cases: First is the applied frequency being far away from the Larmor frequency (off resonance, $\nu \ll \nu_\mathrm{L}$ and $\nu \gg \nu_\mathrm{L}$) and second is the case of the applied frequency being in resonance with the Larmor frequency (on resonance, $\nu = \nu_\mathrm{L}$). The shaded areas indicate the 1σ uncertainties at the respective time.

A typical property to describe and compare different peaks or resonances is the FWHM. In order to yield a meaningful characterisation of a resonance, the FWHM is required to be constant over time, which is the case e.g. for Gaussian or Lorentzian functions. Fitting a β-NMR spectrum in one dimension, as presented in Section 5.2.3, is done under the assumption that the spectrum takes a Lorentzian line shape. However, as demonstrated above, the line shape of the β-NMR resonances is not constant over time. In return, the FWHM is not constant over time. Briefly introduced here is a method to numerically determine the time-dependent FWHM: First, the half maximum over time is derived as half of the amplitude shown in Figure 5.14. Second, the frequencies at which the two-dimensional fit and the half maximum intersect are obtained over time. These intersections are illustrated with red circles in the projections in Figure 5.15. In order to obtain the uncertainty of the FWHM, the frequencies at the intersections of the uncertainties of the fit and the half maximum are found to infer a lower and an upper boundary of the FWHM. This is shown with blue circles in Figure 5.15. The difference between the intersection and the half maximum to the lower and upper boundary is then taken as the uncertainty of the FWHM. In the example of ^{47}K in EMIM-DCA in Figure 5.15, the FWHM differs from $2.8(1)\,\mathrm{ppm}$ at $t = 1.0\,\mathrm{s}$, $4.8(1)\,\mathrm{ppm}$ at $t = 3.0\,\mathrm{s}$ to $8.2(6)\,\mathrm{ppm}$ at $t = 8.0\,\mathrm{s}$. For KCl, the FWHM is determined to take values of $100(2)\,\mathrm{ppm}$ at $t = 2.1\,\mathrm{s}$, $193(1)\,\mathrm{ppm}$ at $t = 7.0\,\mathrm{s}$ and $298(3)\,\mathrm{ppm}$ at $t = 16.0\,\mathrm{s}$. Figure 5.16 shows how the FWHM evolves over time for these measurements of ^{47}K in EMIM-DCA and KCl. Evidently, the FWHM of the β-NMR spectra monotonically increases over time, which is incompatible with the assumption of a Lorentzian line shape for the one-dimensional fitting approach introduced in Section 5.2.3. Note that the FWHM of the spectrum with the EMIM-DCA host cannot be derived for the whole acquisition duration of $17\,\mathrm{s}$ because the uncertainty of the half maximum and the fit projection will at some point be continuously overlapping as the resonance amplitude decreases.

At this point, it is worth verifying that the line shape of the two-dimensional fits including the broadening of the resonance and the establishment of the plateau represents the measured β decay asymmetry. To do so, the fits of the β-NMR resonances of ^{47}K in EMIM-DCA and in KCl are evaluated for different times t to

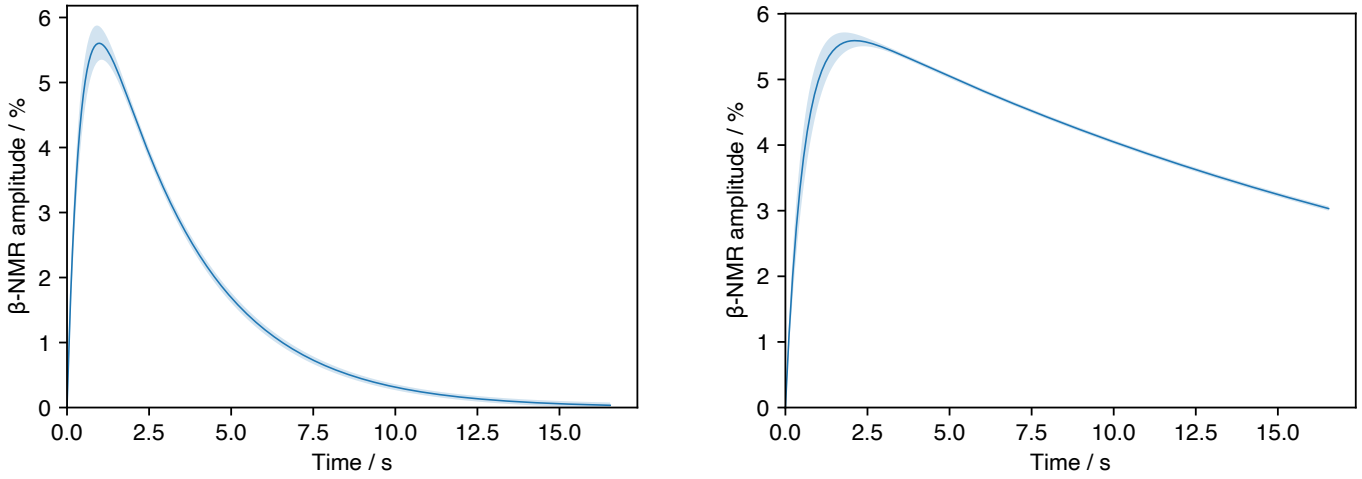

(a) ^{47}K in EMIM-DCA. (b) ^{47}K in KCl.

Figure 5.14.: The amplitude of the β-NMR resonances as a function of time for ^{47}K implanted into (a) EMIM-DCA and (b) KCl computed as the difference of the relaxation on and off resonance from Figure 5.13. The shaded areas indicate the 1σ uncertainties at the respective time.

obtain projections that illustrate the evolution of the line shape. These projections are then plotted together with the measured β decay asymmetry of the $0.2\,\mathrm{s}$-time bin corresponding to the respective evaluation time t. Figures A.1 and A.2 in the Appendix A.1 show the results for EMIM-DCA and KCl at four times t each. As to be expected with $\chi^2_{\mathrm{red}} = 1.03$ for EMIM-DCA, the projections and thus the two-dimensional fit represents the data appropriately along the frequency axis at all times t. It is moreover important to emphasize that the broadening and the plateau becoming more prevailing over time are indeed clearly visible in the measured spectrum. This evolution of the line shape is even more evident in the case of β-NMR of ^{47}K in KCl. While the recorded asymmetry first takes a line shape that is similar to a Lorentzian function at $3.4\,\mathrm{s}$, a saturation is already notable. For later points in time, the plateau and its broadening are palpable. This evolution of the line shape is also observed for the two-dimensional fit, which results in a low χ^2_{red} of 1.16. The illustrations of the projections together with the acquired β decay asymmetry and the obtained values of χ^2_{red} show that the two-dimensional approach of fitting along the frequency and the time axis is able to reproduce the line shape of the measured β-NMR resonances at all times.

The evaluation conducted in this section demonstrates the advantage of the two-dimensional approach over its one-dimensional counterpart. As listed earlier in the comparison of the fitting results of the two methods, Tables 5.1 and 5.2, the two-dimensional approach offers lower uncertainties and yields consistently a χ^2_{red} in the order of 1 for all measurements. This is the result of the fitting function in Equation (5.2) yielding a line shape that enables a profound representation of the β-NMR spectra along the frequency and the time axes, including the relaxation on and off resonance, the time-dependent FWHM and the plateau when the nuclear spin polarisation has relaxed. The in-depth analysis of the two-dimensional approach and its verification with the measured β decay asymmetry furthermore emphasize that it is indispensable to treat these time-dependent signals as such.

Summary

The approach of processing the data in two dimensions brings enhancements in addition to a more precise determination of the Larmor frequency ν_{L}. Unlike in one-dimensional fits, it is not necessary to compromise the signal by manually evaluating and selecting observation time windows. Instead, only a single fit is applied

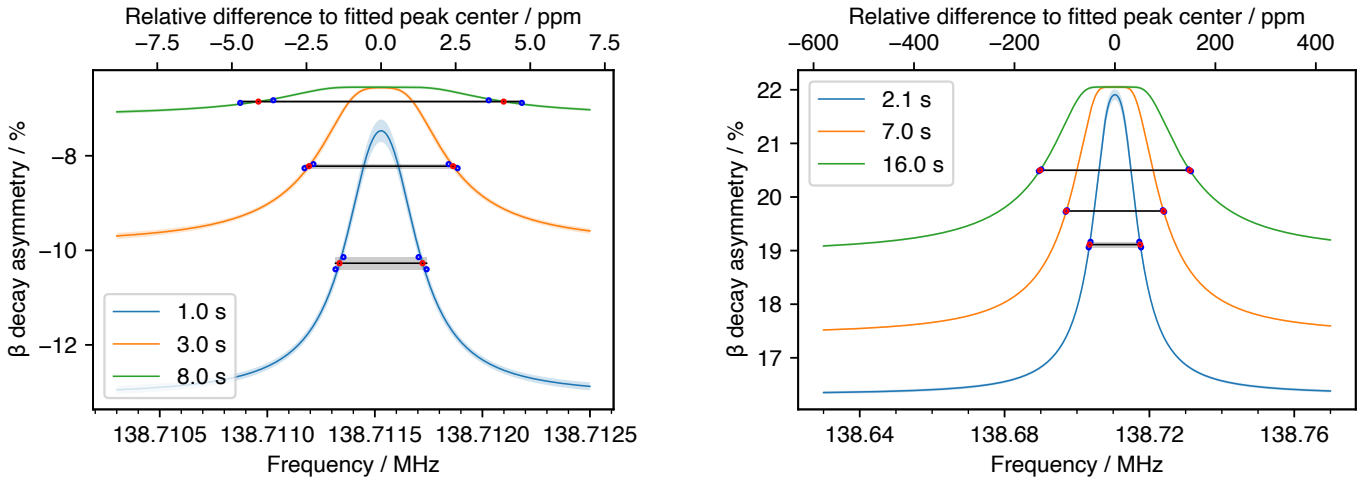

(a) ^{47}K in EMIM-DCA.

(b) ^{47}K in KCl.

Figure 5.15.: Projections of the two-dimensional fits of the β-NMR resonance of ^{47}K implanted into (a) EMIM-DCA and (b) KCl from Figures 5.10 and 5.11 evaluated for different times t. The projections and their respective half maxima are shown with their uncertainties as shaded areas. A more and more pronounced plateau establishes over time nuclear spins relax and the resonance saturates. The intersections of the fit and the half maximum are exploited to numerically determine the FWHM, as indicated with red and blue circles, see text for details.

to the whole data set of a measurement, which renders it less susceptible to errors, easier to execute and more efficient. It yields a consistent, more comprehensive and more complete representation of the β-NMR signal that exploits the full data set with all detected β events and considers the relaxation of the signal. This means that the relaxation constants T_1 off resonance and T_{on} on resonance can be obtained as a by-product for every β-NMR measurement. In return, they allow to determine the amplitude of the spectrum as a function of time. An evaluation of the two-dimensional fit comparing it to the measured β decay asymmetry shows a good agreement with χ^2_{red} in the order of 1. The two-dimensional fits are thus a precise and efficient way of analysing time-resolved β-NMR spectra. Therefore, all β-NMR resonances recorded for this thesis were fitted in two dimensions as a function of frequency and time to prepare for the data analysis in the next section of this thesis.

Future considerations with VCS

The one-dimensional and two-dimensional fitting presented in the above Sections currently utilise only the time of arrival of the β events recorded by VCS. Other pulse properties determined by VCS are not exploited, such as the amplitude of the signal or the integral. These can yield information on the energy of the detected β particles which in return enables advanced options for processing the data. For example, it allows discarding β events depending on their energy and thus depending on their parent nuclei. The thin β detectors that were used for the experiments in this thesis, however, do not allow the β particles to fully deposit their energy into the scintillators. A meaningful energy resolution is thus hindered and the amplitude and integral properties cannot be utilised at this point. When new β detectors are implemented, future experiments will make use of this functionality to push the possibilities of the analysis further.

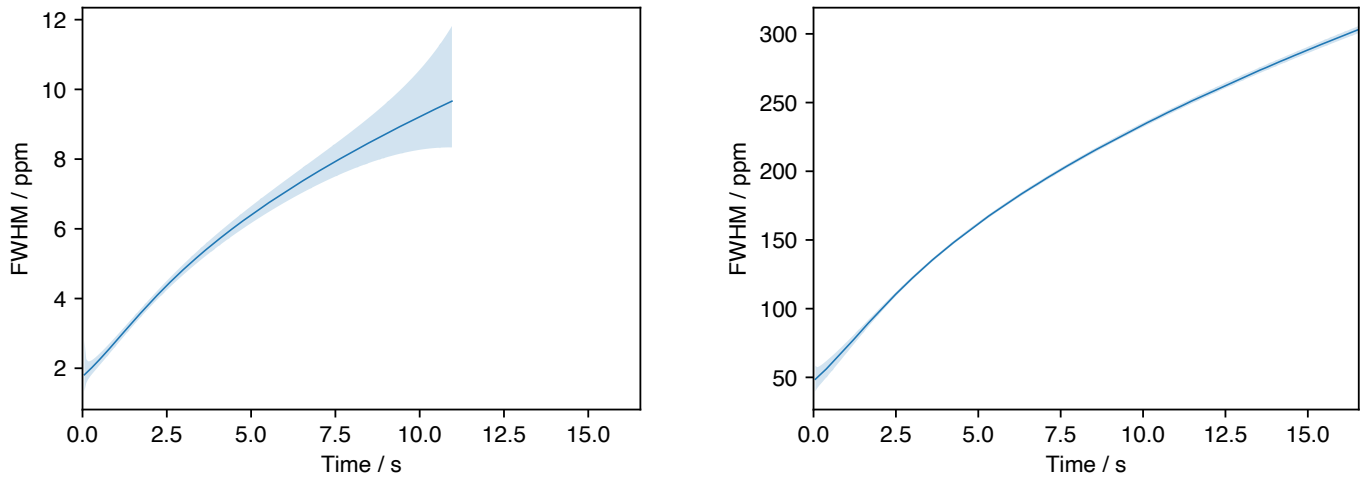

(a) ^{47}K in EMIM-DCA. (b) ^{47}K in KCl.

Figure 5.16.: The FWHM as a function of time determined numerically for ^{47}K implanted into (a) EMIM-DCA and (b) KCl, with the 1σ uncertainties shown as shaded areas.

5.3. Experimental data

Presented in this section is an overview on the data relevant to determine the hyperfine anomaly and the magnetic moment of ^{47}K. First, rf saturation curves of β-NMR measurement of ^{47}K in KCl and EMIM-DCA are discussed. This is followed by the Larmor frequencies of the precision measurements with EMIM-DCA and the corresponding reference frequencies recorded with the ^{2}H probe.

5.3.1. Saturation curves

When the β-NMR spectra of ^{47}K presented in this thesis were recorded in 2022, the two-dimensional fitting routines introduced in Section 5.2.4 did not exist yet. Instead, the spectra were originally fitted during the experiment with the conventional, one-dimensional approach explained in Section 5.2.3. The effects of broadening and saturation of the resonances were accounted for by evaluating saturation curves that show the dependency of the amplitude of the β-NMR resonances and their FWHM on the rf amplitude. In order to acquire such saturation curves, a number of β-NMR spectra with varying rf amplitude were recorded while all other parameters were kept constant, such as the sample and the scanned frequency range. The spectra would then be fitted under the assumption of a Lorentzian line shape. Changes in the determined amplitude and FWHM of the resonances would thus be solely dependent on the rf amplitude. The aim of these saturation curves was to determine the rf amplitude that maximises the amplitude of the β-NMR resonance while minimising its broadening, thereby optimising the conditions for applying a one-dimensional Lorentzian fit.

An example of such saturation curves is shown in Figure 5.17 for measurements of ^{47}K implanted into KCl with rf amplitudes from $5\,\mathrm{mV}$ to $50\,\mathrm{mV}$. While an increase in the rf amplitude first results in an enhancement of the amplitude of the β-NMR resonance, a saturation appears to be occurring at an rf amplitude of $20\,\mathrm{mV}$ when the signal amplitude reaches about $4.5\,\%$. Increasing the rf amplitude further does not yield a higher β-NMR amplitude. On the other hand, the FWHM keeps increasing monotonically. Therefore, the resonances would be considered saturated at an amplitude of $20\,\mathrm{mV}$. All subsequent measurements with this sample would hence apply this setting.

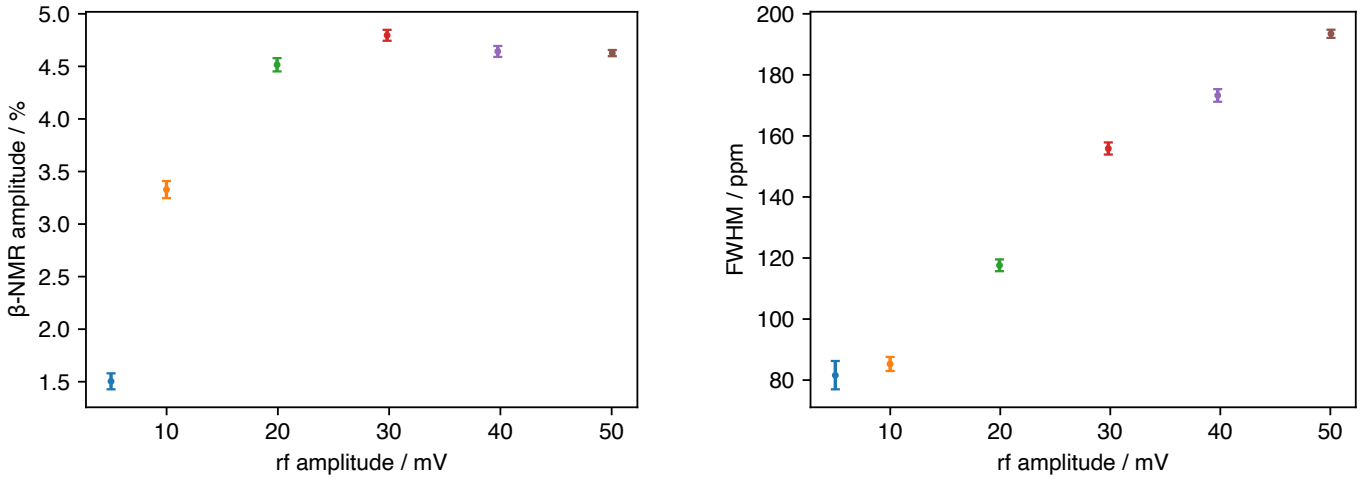

(a) β-NMR amplitude.

(b) FWHM.

Figure 5.17.: Saturation curves of ^{47}K implanted into a KCl crystal with the amplitude and the FWHM of the β-NMR spectrum as a function of the rf amplitude. While the amplitude (a) of the resonance saturates at $20\,\mathrm{mV}$, the FWHM (b) indicates a monotone increase.

However, as presented in Section 5.2.4, the amplitude and the FWHM of the β-NMR resonance vary with time. Figure 5.18 illustrates this time dependency of the amplitude and the FWHM for the saturation measurements of ^{47}K implanted into KCl. In fact, the saturation curves in Figure 5.17 can be obtained from this figure by evaluating the amplitude and the FWHM at a time of $t = 7\,\mathrm{s}$. It is hence not fully correct to state that the rf amplitude of $20\,\mathrm{mV}$ saturates the resonance since this discards the time dependency. Clearly visible in Figure 5.18 is that a higher rf amplitude results in broader resonances irrespective of the time. In addition, the time at which the resonance reaches its maximum amplitude is rf-dependent. This is the case since the β-NMR amplitude is the difference of the asymmetry on and off resonance. While the applied rf field does not alter the T_1 relaxation off resonance, it does affect the relaxation time T_{on} on resonance. A higher rf amplitude results in a faster relaxation and thus a shorter time $t_{0.98}$ until effectively full relaxation on resonance. Consequently, the maximum amplitude of the β-NMR resonance is increased and occurs earlier. The amplitude and the FWHM depicted in Figure 5.17 would thus show the saturation at a different rf amplitude if the evaluation time t was varied. For example, none of the rf amplitudes of $5\,\mathrm{mV}$ to $50\,\mathrm{mV}$ would be considered to saturate the resonance at a time of $t = 2.5\,\mathrm{s}$ whereas all rf amplitudes except for $5\,\mathrm{mV}$ appear to reach the saturation condition at $17\,\mathrm{s}$. It is therefore impossible to assess what rf amplitude is preferable solely based on the evaluation of the amplitude and the FWHM of the resonance.

Another aspect that speaks against the evaluation of the amplitude and the FWHM for one-dimensional fits is the change of the line shape discussed in Section 5.2.4. Since the β decay asymmetry is integrated over the entire observation time window, these windows have a tendency of being longer than $t_{0.98}$, because the low signal amplitude shortly after the implantation is compensated by the higher amplitude at later times. However, the line shape will at this later time already include a plateau, resulting in the Lorentzian function no longer being applicable to fully reproduce the resonance.

The β-NMR resonances that were originally recorded for evaluating the saturation curve based on one-dimensional fits are now considered for the two-dimensional fitting approach. A three-dimensional representation of the results for all six measurements with varying rf amplitude is shown in the Appendix A.2

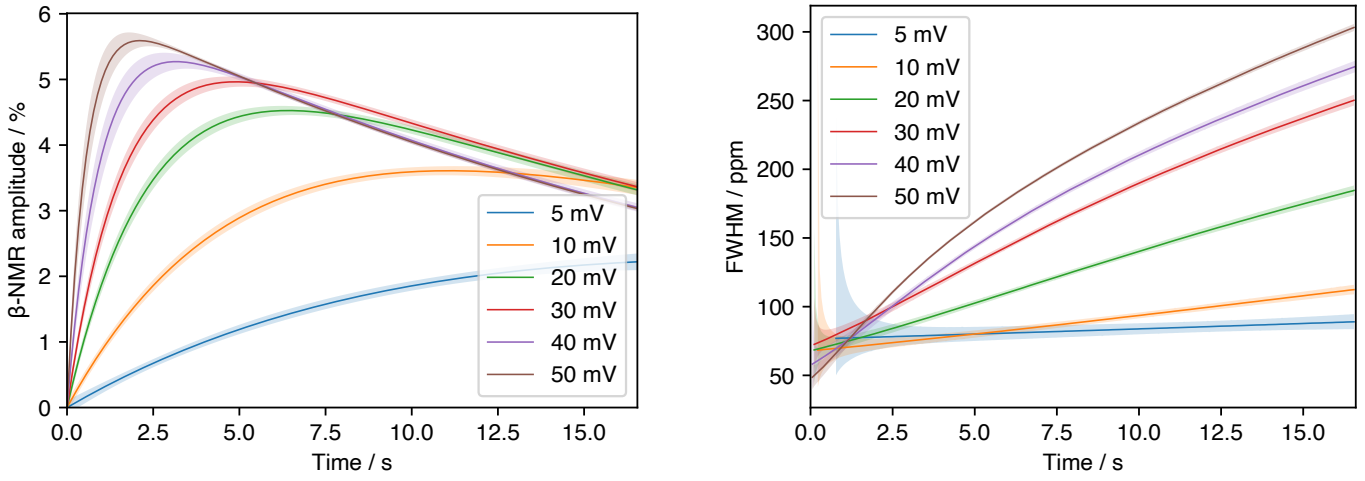

(a) β-NMR amplitude.

(b) FWHM.

Figure 5.18.: The amplitude (a) of the β-NMR resonances and their FWHM as a function of the rf amplitude and the time for measurements of ^{47}K in KCl. It is clearly visible how a higher rf amplitude causes the β-NMR resonances to reach their maximum amplitude earlier.

in Figure A.3. Even though the line shape clearly shows a plateau at higher rf amplitudes, values of χ^2_{red} ranging from 1.06 to 1.16 indicate that the two-dimensional fits allow for an appropriate representation of the measured β decay asymmetry across the entire frequency and time range regardless of the applied rf amplitude. It is therefore not relevant for the fitting approach at what point the resonances are (partially) saturated nor when the plateau establishes.

Next, the six β-NMR measurements recorded with different amplitudes are utilised to investigate if there is nonetheless a tendency for a preferable rf amplitude. The fit parameter relevant for the β-NMR studies is the Larmor frequency ν_{L}. Hence, ν_{L} and its uncertainty $\delta\nu_{\mathrm{L}}$ are evaluated as a function of the applied rf voltage, with the results for the saturation measurements of ^{47}K in KCl shown in Figure 5.19. The Larmor frequencies ν_{L} are comparable for the different rf amplitudes, while a decrease in the uncertainty as a function of the rf amplitude is notable. In the case of an amplitude of $50\,\mathrm{mV}$, this results from the applied frequency having a finer resolution of $2\,\mathrm{kHz}$ as opposed to $5\,\mathrm{kHz}$ for the other four measurements with rf amplitudes of $5\,\mathrm{mV}$ to $40\,\mathrm{mV}$. Moreover, the uncertainties for rf amplitudes of more than $5\,\mathrm{mV}$ are around a factor of two smaller than at $5\,\mathrm{mV}$. The combination of two aspects is responsible for this observation. First, higher rf amplitudes result in enhanced β-NMR amplitudes and cause their maximum amplitude to occur earlier, as seen in Figure 5.18 and Figure A.3. Second, taking into account the decay of the isotope, the number of detected β particles is higher at the beginning of the acquisition than towards its end. In return, the uncertainty of the computed β decay asymmetry is smaller for earlier time bins. It is hence beneficial to shift the time of the maximum amplitude of the β-NMR resonance to the time of the smallest uncertainty in the β decay asymmetry by optimising the rf amplitude and thus increasing the statistical significance of the signal.

Similar to β-NMR measurements implanting ^{47}K into KCl, saturation curves were also recorded for ^{47}K in EMIM-DCA. These are presented in Appendix A.2 together with a brief explanation analogous to the saturation curves of ^{47}K in KCl. With ^{47}K in EMIM-DCA having a T_1 relaxation time that is one order of magnitude smaller than in KCl, it is essential to have a sufficiently high rf amplitude to minimise the relaxation time on resonance described by T_{on} and thus increase the signal amplitude, as seen in Figure A.5, to enhance the statistical significance. Consequently, the uncertainties of the Larmor frequency ν_{L} should be evaluated with

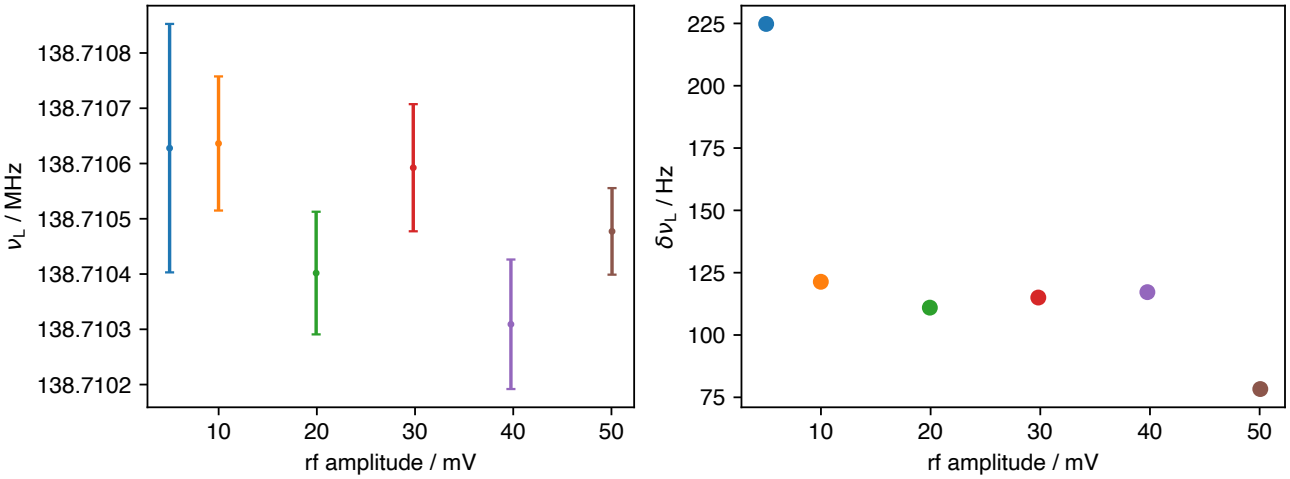

(a) Larmor frequency ν_{L}.

(b) Uncertainty $\delta\nu_{\mathrm{L}}$ of the Larmor frequency.

Figure 5.19.: Larmor frequencies ν_{L} (a) of β-NMR spectra of ^{47}K in KCl as a function of the rf amplitude and (b) their respective uncertainties. The lower statistical significance of the resonance signal at an rf amplitude of $5\,\mathrm{mV}$ results in a larger uncertainty. The spectrum recorded with an rf amplitude of $50\,\mathrm{mV}$ offers a lower uncertainty due to the applied frequency ν having a step size of $2\,\mathrm{kHz}$ rather than $5\,\mathrm{kHz}$ for all other shown spectra.

the two-dimensional fits as a function of the rf amplitude for every sample in future experiments.

5.3.2. β-NMR measurements of ^{47}K in EMIM-DCA

A variety of β-NMR measurements was conducted over the course of three beam times in 2022 to study the isotope ^{47}K in different host materials, i.e. KCl and EMIM-DCA. The acquired spectra were fitted with the two-dimensional approach introduced in Section 5.2.4. EMIM-DCA showed consistently narrow resonances with very small uncertainties in the Larmor frequency ν_{L} of less than $1\,\mathrm{ppm}$. This results from the molecular tumbling in the ionic liquid averaging out anisotropic effects that occur in solid states. Therefore, EMIM-DCA is considered a suitable host for the precision studies of the differential hyperfine anomaly and the magnetic dipole moment of ^{47}K. The respective measurements were fitted in two dimensions according to Section 5.2.4 to yield the Larmor frequency $\nu^{^{47}\mathrm{K},\,4.7\,\mathrm{T},\,\mathrm{EMIM}}$ of ^{47}K in EMIM-DCA in a magnetic field of $B_0 \approx 4.7\,\mathrm{T}$. To precisely determine B_0 at the time of the respective β-NMR scan, FIDs were recorded with the ^{2}H reference probe and processed as described in Section 5.2.2. The determined frequencies ν_{ref} and the carrier frequency $\nu_{\mathrm{carrier}} = 30\,752\,710\,\mathrm{Hz}$ will then give $\nu^{^{2}\mathrm{H},\,\mathrm{D_2O}}$ with Equation (5.1). An uncertainty of $10\,\mathrm{Hz}$ $(0.3\,\mathrm{ppm})$ is considered for ν_{carrier} to take into account possible deviations in the positioning of the ^{2}H probe. Table 5.3 lists the determined Larmor frequencies of the measurements. Further parameters of these β-NMR resonances of ^{47}K in EMIM-DCA are given in the Appendix A.2.3, including the relaxation time constants T_1 off resonance and T_{on} on resonance.

As can be seen in Table 5.3, the Larmor frequencies $\nu^{^{47}\mathrm{K},\,4.7\,\mathrm{T},\,\mathrm{EMIM}}$ acquired during the beam times in July and November are consistent. They show a comparable chemical shift of about $20\,\mathrm{ppm}$ between ^{47}K in EMIM-DCA and in KCl (not presented here), leading to the conclusion that these data sets are reliable. In comparison to that, the Larmor frequencies $\nu^{^{47}\mathrm{K},\,4.7\,\mathrm{T},\,\mathrm{EMIM}}$ acquired in May 2022 deviate by about $1\,\mathrm{kHz}$ $(7\,\mathrm{ppm})$. Furthermore, the chemical shift between EMIM-DCA and KCl is about $-10\,\mathrm{ppm}$ which is not consistent with the measurements in July and November. The reason for this discrepancy is not fully understood and

merits further investigation. One suspicion is that the two rf generators used for the β-NMR measurements and the ^{2}H reference probe were not sharing the same reference clock. For the above reasons, the measurements acquired in May 2022 are not taken into account for the determination of the differential hyperfine anomaly and the magnetic moment in the following sections.

Table 5.3.: The Larmor frequencies $\nu^{^{47}\mathrm{K},\,4.7\,\mathrm{T},\,\mathrm{EMIM}}$ of the β-NMR studies of ^{47}K in EMIM-DCA and the respective reference frequencies $\nu^{^{2}\mathrm{H},\,\mathrm{D_2O}}$ that are considered for the evaluation of the hyperfine anomaly and the magnetic moment of ^{47}K.

Timestamp	SampleID	ν_{ref} / Hz	$\nu^{^{2}\mathrm{H},\,4.7\,\mathrm{T},\,\mathrm{D_2O}}$ / Hz	$\nu^{^{47}\mathrm{K},\,4.7\,\mathrm{T},\,\mathrm{EMIM}}$ / Hz
20220522-011603	EP1_K47_NMR_5	1125(1)	30 751 585(11)	138 711 540(14)
20220522-025524	EP1_K47_NMR_7	1125(1)	30 751 585(11)	138 711 608(44)
20220522-032022	EP1_K47_NMR_8	1125(1)	30 751 585(11)	138 711 522(24)
20220522-034518	EP1_K47_NMR_9	1125(1)	30 751 585(11)	138 711 540(23)
20220522-045844	EP1_K47_NMR_13	1125(1)	30 751 585(11)	138 711 538(17)
20220522-062619	EP1_K47_NMR_14	1125(1)	30 751 585(11)	138 711 526(15)
20220523-075809	EP2_K47_NMR_1	1126(1)	30 751 584(11)	138 711 541(9)
20220523-090149	EP2_K47_NMR_2	1126(1)	30 751 584(11)	138 711 529(7)
20220714-223719	EP1_NMR_008	1102(1)	30 751 608(11)	138 710 522(26)
20220715-000047	EP1_NMR_009	1102(1)	30 751 608(11)	138 710 524(41)
20220715-002510	EP1_NMR_010	1106(1)	30 751 604(11)	138 710 604(30)
20220715-005209	EP1_NMR_011	1106(1)	30 751 604(11)	138 710 558(46)
20220715-011631	EP1_NMR_014	1106(1)	30 751 604(11)	138 710 571(19)
20220715-025208	EP1_NMR_015	1106(1)	30 751 604(11)	138 710 630(21)
20221123-061849	K47_mika_E1_NMR001	1207(1)	30 751 503(11)	138 710 707(19)
20221123-063419	K47_mika_E1_NMR003	1207(1)	30 751 503(11)	138 710 676(12)
20221123-065249	K47_mika_E1_NMR004	1207(1)	30 751 503(11)	138 710 626(8)

5.4. Determining the hyperfine anomaly of ^{47}K

One of the aims of the studies presented in this thesis is to determine the hyperfine anomaly of ^{47}K with great precision based on β-NMR measurements. The required Larmor frequencies $\nu^{^{47}\mathrm{K},\,4.7\,\mathrm{T},\,\mathrm{EMIM}}$ of ^{47}K in EMIM-DCA and the respective reference frequencies $\nu^{^{2}\mathrm{H},\,4.7\,\mathrm{T},\,\mathrm{D_2O}}$ are presented in the previous Section 5.3.2. First, the ratio $R_0^{^{47}\mathrm{K}/^{39}\mathrm{K}}$ of the magnetic moment $\mu_I(^{47}\mathrm{K})$ of ^{47}K and the magnetic moment of a reference isotope, here $\mu_I(^{39}\mathrm{K})$ for stable ^{39}K, is determined. Second, the result is compared to the ratio $R_{\mathrm{A}}^{^{47}\mathrm{K}/^{39}\mathrm{K}}$ of the hyperfine structure parameters $A(^{47}\mathrm{K})$ and $A(^{39}\mathrm{K})$ of the 4s $^{2}\mathrm{S}_{1/2}$ ground state. $A(^{47}\mathrm{K})$ was measured at the COLLAPS experiment at ISOLDE using laser spectroscopy [88] while $A(^{39}\mathrm{K})$ was identified using atomic beam magnetic resonance [7]. The difference between the two ratios then yields the differential hyperfine anomaly of ^{47}K and ^{39}K, as explained in Section 2.3.3.

Following Equation (3.9), the ratio R_0 of two nuclear magnetic dipole moments μ_I and $\mu_I(\mathrm{ref})$ can be written as

$$R_0 = \frac{\mu_I}{\mu_I(\mathrm{ref})} = \frac{\nu_0 I}{\nu_0^{\mathrm{ref}} I^{\mathrm{ref}}} \frac{B_0^{\mathrm{ref}}}{B_0}. \tag{5.3}$$

In the context of this thesis, the corresponding isotopes are ^{47}K and ^{39}K. Consequently, the ratio of interest is

$$R_0^{^{47}\mathrm{K}/^{39}\mathrm{K}} = \frac{\mu_I(^{47}\mathrm{K})}{\mu_I(^{39}\mathrm{K})} = \frac{\nu_0^{^{47}\mathrm{K}} I^{^{47}\mathrm{K}}}{\nu_0^{^{39}\mathrm{K}} I^{^{39}\mathrm{K}}} \frac{B_0^{^{39}\mathrm{K}}}{B_0^{^{47}\mathrm{K}}}, \tag{5.4}$$

with $\nu_0^{^{47}\mathrm{K}}$ and $\nu_0^{^{39}\mathrm{K}}$ being the Larmor frequencies of ^{47}K and ^{39}K in the respective magnetic fields $B_0^{^{47}\mathrm{K}}$ and $B_0^{^{39}\mathrm{K}}$. While the fields are known to be $B_0^{^{47}\mathrm{K}} \approx 4.7\,\mathrm{T}$ and $B_0^{^{39}\mathrm{K}} \approx 1.8\,\mathrm{T}$, it is crucial to determine them with great precision at the time of the β-NMR measurement. As explained in Section 5.2.2, this is done with ^{2}H reference probes that acquire the Larmor frequencies $\nu_0^{^{2}\mathrm{H},\,4.7\,\mathrm{T}}$ and $\nu_0^{^{2}\mathrm{H},\,1.8\,\mathrm{T}}$. Rearranging Equation (3.9) then yields the magnetic fields $B_0^{^{47}\mathrm{K}}$ and $B_0^{^{39}\mathrm{K}}$ via

$$B_0^{^{47}\mathrm{K}} = \frac{\nu_0^{^{2}\mathrm{H},\,4.7\,\mathrm{T}} I^{^{2}\mathrm{H}} h}{\mu_I^{^{2}\mathrm{H}}} \text{ and} \tag{5.5}$$

$$B_0^{^{39}\mathrm{K}} = \frac{\nu_0^{^{2}\mathrm{H},\,1.8\,\mathrm{T}} I^{^{2}\mathrm{H}} h}{\mu_I^{^{2}\mathrm{H}}}. \tag{5.6}$$

Substituting these expressions into Equation (5.4) gives

$$\begin{aligned} R_0^{^{47}\mathrm{K}/^{39}\mathrm{K}} &= \frac{\nu_0^{^{47}\mathrm{K}} I^{^{47}\mathrm{K}}}{\nu_0^{^{39}\mathrm{K}} I^{^{39}\mathrm{K}}} \frac{\nu_0^{^{2}\mathrm{H},\,1.8\,\mathrm{T}} \cancel{I^{^{2}\mathrm{H}} h}}{\cancel{\mu_I^{^{2}\mathrm{H}}}} \frac{\cancel{\mu_I^{^{2}\mathrm{H}}}}{\nu_0^{^{2}\mathrm{H},\,4.7\,\mathrm{T}} \cancel{I^{^{2}\mathrm{H}} h}} \\ &= \underbrace{\frac{\nu_0^{^{47}\mathrm{K}}}{\nu_0^{^{2}\mathrm{H},\,4.7\,\mathrm{T}}}}_{:=\zeta} \underbrace{\frac{\nu_0^{^{2}\mathrm{H},\,1.8\,\mathrm{T}}}{\nu_0^{^{39}\mathrm{K}}}}_{:=1/\xi} \frac{I^{^{47}\mathrm{K}}}{I^{^{39}\mathrm{K}}}, \end{aligned} \tag{5.7}$$

where the factor ζ represents the ratio of the Larmor frequencies of ^{47}K and the corresponding ^{2}H reference probe and ξ is the ratio of the Larmor frequencies of ^{39}K and its ^{2}H reference. It is required to correct the measured Larmor frequencies for the magnetic susceptibility and the NMR shielding of the nuclei in their respective environment to obtain these Larmor frequencies ν_0, as explained in Section 3.1.3. To be considered for the measured Larmor frequency $\nu^{^{47}\mathrm{K},\,4.7\,\mathrm{T},\,\mathrm{EMIM}}$ of ^{47}K in EMIM-DCA are the orientation of the sample at an angle of $45°$ with respect to B_0 (see Section 4.3.1) for the magnetic susceptibility correction and the shielding of the K nuclei in EMIM-DCA. The reference probe is oriented perpendicular to the magnetic field and its Larmor frequency $\nu^{^{2}\mathrm{H},\,4.7\,\mathrm{T},\,\mathrm{D_2O}}$ needs furthermore to be corrected for the ^{2}H nuclei being hosted in D_2O. It follows from Equation (3.12) that

$$\zeta = \frac{\nu^{^{47}\mathrm{K},\,4.7\,\mathrm{T},\,\mathrm{EMIM}}}{\nu^{^{2}\mathrm{H},\,4.7\,\mathrm{T},\,\mathrm{D_2O}}} \frac{\left[1 + (1/3 - \alpha_\perp)\kappa^{\mathrm{D_2O}}\right]}{1 + \underbrace{(1/3 - \alpha_{45°})\kappa^{\mathrm{EMIM}}}_{:=N}} \frac{\left(1 - \sigma^{^{2}\mathrm{H},\,\mathrm{D_2O}}\right)}{\left(1 - \sigma^{^{\mathrm{K},\,\mathrm{EMIM}}}\right)}, \tag{5.8}$$

where $\alpha_\perp$ is the shape factor of a perpendicular orientation of the sample to B_0, $\kappa^{\mathrm{D_2O}}$ and κ^{EMIM} are the volume magnetic susceptibilities of D_2O and EMIM-DCA. $\left(1 - \sigma^{^{2}\mathrm{H},\,\mathrm{D_2O}}\right)$ and $\left(1 - \sigma^{^{\mathrm{K},\,\mathrm{EMIM}}}\right)$ correct for the NMR shielding of ^{2}H in D_2O and K in EMIM-DCA. The term $N \coloneqq (1/3 - \alpha_{45°})\kappa^{\mathrm{EMIM}}$ with the shape factor $\alpha_{45°}$ of the sample being oriented at an angle of $45°$ to B_0 and the volume magnetic susceptibility κ^{EMIM} of EMIM-DCA was simulated in CST Studio. Analogously to ζ follow the corrections for ξ with

$$\xi = \underbrace{\frac{\nu^{^{39}\mathrm{K},\,1.8\,\mathrm{T},\,\mathrm{H_2O}}}{\nu^{^{2}\mathrm{H},\,1.8\,\mathrm{T},\,\mathrm{D_2O}}}}_{:=S} \frac{\left[1+(1/3-\alpha_\parallel)\kappa^{\mathrm{D_2O}}\right]}{\left[1+(1/3-\alpha_\parallel)\kappa^{\mathrm{H_2O}}\right]} \frac{\left(1-\sigma^{^{2}\mathrm{H},\,\mathrm{D_2O}}\right)}{\left(1-\sigma^{\mathrm{K},\,\mathrm{H_2O}}\right)}. \tag{5.9}$$

The shape factor $\alpha_\parallel$ indicates that both samples were oriented along the magnetic field B_0. $\kappa^{\mathrm{D_2O}}$ and $\kappa^{\mathrm{H_2O}}$ represent the volume susceptibility of D_2O and H_2O, while $\sigma^{^{2}\mathrm{H},\,\mathrm{D_2O}}$ and $\sigma^{\mathrm{K},\,\mathrm{H_2O}}$ are the NMR shielding of ^{2}H in D_2O and K in H_2O, respectively. The frequency ratio $\nu^{^{39}\mathrm{K},\,\mathrm{H_2O}}/\nu^{^{2}\mathrm{H},\,1.8\,\mathrm{T},\,\mathrm{D_2O}} := S$ is taken from literature [101]. It is then possible to insert the corrected frequency ratios ζ from (5.8) and ξ from (5.9) into Equation (5.7) to obtain

$$R_0^{^{47}\mathrm{K}/^{39}\mathrm{K}} = \frac{\nu^{^{47}\mathrm{K},\,4.7\,\mathrm{T},\,\mathrm{EMIM}}}{\nu^{^{2}\mathrm{H},\,4.7\,\mathrm{T},\,\mathrm{D_2O}}} \frac{1}{S} \frac{\left[1+(1/3-\alpha_\perp)\kappa^{\mathrm{D_2O}}\right]}{1+N} \frac{\cancel{\left(1-\sigma^{^{2}\mathrm{H},\,\mathrm{D_2O}}\right)}}{\left(1-\sigma^{\mathrm{K},\,\mathrm{EMIM}}\right)} \frac{\left[1+(1/3-\alpha_\parallel)\kappa^{\mathrm{H_2O}}\right]}{\left[1+(1/3-\alpha_\parallel)\kappa^{\mathrm{D_2O}}\right]} \frac{\left(1-\sigma^{\mathrm{K},\,\mathrm{H_2O}}\right)}{\cancel{\left(1-\sigma^{^{2}\mathrm{H},\,\mathrm{D_2O}}\right)}} \frac{I^{^{47}\mathrm{K}}}{I^{^{39}\mathrm{K}}} \tag{5.10}$$

$$R_0^{^{47}\mathrm{K}/^{39}\mathrm{K}} = \frac{\nu^{^{47}\mathrm{K},\,4.7\,\mathrm{T},\,\mathrm{EMIM}}}{\nu^{^{2}\mathrm{H},\,4.7\,\mathrm{T},\,\mathrm{D_2O}}} \frac{1}{S} \frac{\left[1+(1/3-\alpha_\perp)\kappa^{\mathrm{D_2O}}\right]}{1+N} \frac{\left[1+(1/3-\alpha_\parallel)\kappa^{\mathrm{H_2O}}\right]}{\left[1+(1/3-\alpha_\parallel)\kappa^{\mathrm{D_2O}}\right]} \frac{\left(1-\sigma^{\mathrm{K},\,\mathrm{H_2O}}\right)}{\left(1-\sigma^{\mathrm{K},\,\mathrm{EMIM}}\right)} \frac{I^{^{47}\mathrm{K}}}{I^{^{39}\mathrm{K}}}. \tag{5.11}$$

This ratio is then computed for all Larmor frequencies $\nu^{^{47}\mathrm{K},\,4.7\,\mathrm{T},\,\mathrm{EMIM}}$ and $\nu^{^{2}\mathrm{H},\,4.7\,\mathrm{T},\,\mathrm{D_2O}}$ listed in Section 5.3.2 with the following parameters: $S = 0.303\,984\,85(9)$ from [101], $\alpha_\perp = 1/2$ and $\alpha_\parallel = 0$ from [54, 6], $\kappa^{\mathrm{D_2O}} = -8.866\,\mathrm{ppm}$ from [48] and $\kappa^{\mathrm{H_2O}} = -9.035\,\mathrm{ppm}$ from [2]. The nuclear spins of the isotopes are $I^{^{47}\mathrm{K}} = 1/2$ and $I^{^{39}\mathrm{K}} = 3/2$. CST Studio was used to simulate the susceptibility correction of EMIM-DCA on the mica sheet at an angle of $45°$ with respect to B_0 and thus obtain the parameter $N = 1.1(1)\,\mathrm{ppm}$. The NMR shielding $\sigma^{\mathrm{K},\,\mathrm{H_2O}} = 1285(12)\,\mathrm{ppm}$ of K in H_2O and $\sigma^{\mathrm{K},\,\mathrm{EMIM}} = 1247(10)\,\mathrm{ppm}$ of K in EMIM-DCA were determined with molecular dynamics simulations by collaborators [56].

Consequently, the mean of all individual computations yields the final ratio $\mu_I(^{47}\mathrm{K})/\mu_I(^{39}\mathrm{K})$ based on the β-NMR measurements:

$$R_0^{^{47}\mathrm{K}/^{39}\mathrm{K}} = \frac{\mu_I(^{47}\mathrm{K})}{\mu_I(^{39}\mathrm{K})} = 4.945\,99(8). \tag{5.12}$$

This ratio of magnetic moments based on the Larmor frequencies of the nuclei is then compared to a different ansatz. As explained in Section 2.3.3, a magnetic moment μ_I can also be determined based on the hyperfine structure constants A with respect to the magnetic moment $\mu_I(\mathrm{ref})$ of a reference isotope, confer Equation (2.18). Analogue to Equation (5.4), this approach gives

$$R_\mathrm{A}^{^{47}\mathrm{K}/^{39}\mathrm{K}} = \frac{\mu_I(^{47}\mathrm{K})}{\mu_I(^{39}\mathrm{K})} = \frac{A^{^{47}\mathrm{K}} I^{^{47}\mathrm{K}}}{A^{^{39}\mathrm{K}} I^{^{39}\mathrm{K}}}. \tag{5.13}$$

$A^{^{47}\mathrm{K}}$ and $A^{^{39}\mathrm{K}}$ are the hyperfine structure constants of the 4s $^2S_{1/2}$ ground state. Their values $A(^{47}\mathrm{K}) = 3413.2(3)\,\mathrm{MHz}$ and $A(^{39}\mathrm{K}) = 230.859\,860\,1(7)\,\mathrm{MHz}$ are obtained from references [88] and [7]. This yields the ratio

$$R_\mathrm{A}^{^{47}\mathrm{K}/^{39}\mathrm{K}} = \frac{\mu_I(^{47}\mathrm{K})}{\mu_I(^{39}\mathrm{K})} = 4.9282(4). \tag{5.14}$$

Computing the difference between $R_0^{^{47}\mathrm{K}/^{39}\mathrm{K}}$ and $R_\mathrm{A}^{^{47}\mathrm{K}/^{39}\mathrm{K}}$ yields

$$^{39}\Delta^{47} = \frac{R_0^{^{47}\mathrm{K}/^{39}\mathrm{K}}}{R_\mathrm{A}^{^{47}\mathrm{K}/^{39}\mathrm{K}}} - 1 = 0.360(9)\,\%. \tag{5.15}$$

The ratio of the magnetic moments $\mu_I\left(^{47}\mathrm{K}\right)/\mu_I\left(^{39}\mathrm{K}\right)$ computed based on the β-NMR measurements and the laser spectroscopy measurements thus indicate a differential hyperfine anomaly of $^{39}\Delta^{47} = 0.360(9)\,\%$ between the two isotopes ^{47}K and ^{39}K. An interpretation of this result follows in Chapter 6.

5.5. Determining the magnetic dipole moment of ^{47}K

In addition to the differential hyperfine anomaly presented in the previous section, the β-NMR studies of ^{47}K in EMIM-DCA can also be exploited to determine the magnetic dipole moment $\mu_I(^{47}\mathrm{K})$ with great precision. To do so, $\mu_I(^{47}\mathrm{K})$ is put into relation with the magnetic dipole moment of another reference isotope, here ^{2}H. This isotope is selected since all β-NMR spectra of ^{47}K already have corresponding NMR measurements with the ^{2}H reference probe that were originally recorded to obtain the magnetic field B_0, see Section 4.3.2. From Equation (5.3) follows

$$R_0^{^{47}\mathrm{K}/^2\mathrm{H}} = \frac{\mu_I(^{47}\mathrm{K})}{\mu_I(^2\mathrm{H})} = \frac{\nu_0^{^{47}\mathrm{K}}}{\nu_0^{^2\mathrm{H}}}\frac{I^{^{47}\mathrm{K}}}{I^{^2\mathrm{H}}}\frac{B_0^{^2\mathrm{H}}}{B_0^{^{47}\mathrm{K}}}. \tag{5.16}$$

The ratio $\nu_0^{^{47}\mathrm{K}}/\nu_0^{^2\mathrm{H}}$ is already known as ζ from Equation (5.8). Furthermore, the β-NMR measurements of ^{47}K and the NMR measurements of ^{2}H were recorded in the same field at effectively the same time, hence $B_0^{^2\mathrm{H}} = B_0^{^{47}\mathrm{K}}$. Rearranging Equation (5.16) thus leads to the simple expression

$$\mu_I(^{47}\mathrm{K}) = \zeta\frac{I^{^{47}\mathrm{K}}}{I^{^2\mathrm{H}}}\mu_I(^2\mathrm{H}). \tag{5.17}$$

With literature values of $I^{^{47}\mathrm{K}} = 1/2$, $I^{^2\mathrm{H}} = 1$ and $\mu_I(^2\mathrm{H}) = 0.857\,438\,233\,8(22)\mu_\mathrm{N}$ [113], it is finally possible to obtain

$$\mu_I(^{47}\mathrm{K}) = 1.936\,182(19)\mu_\mathrm{N}. \tag{5.18}$$

The β-NMR studies of ^{47}K thus enabled the determination of $\mu_I(^{47}\mathrm{K}) = 1.936\,182(19)\mu_\mathrm{N}$ with an uncertainty of $10\,\mathrm{ppm}$.

6. Discussion

This chapter gives a brief comparison of the magnetic moment $\mu_I(^{47}\mathrm{K})$ and the differential hyperfine anomaly $^{39}\Delta^{47}$ determined based on the β-NMR measurements to literature values. The data analysis is then concluded by discussing how the differential hyperfine anomaly be exploited to obtain new information on the nuclei. In particular, it will be described how to derive the ratio of the spin contribution and the orbital contribution to the magnetic moment [9].

The magnetic moment of ^{47}K was determined to be $\mu_I = 1.936\,182(19)\mu_\mathrm{N}$, with an uncertainty of $10\,\mathrm{ppm}$. This uncertainty is an improvement by two orders of magnitude with respect to the literature value of $1.9292(58)\mu_\mathrm{N}$ that was measured with laser spectroscopy [88].

In addition, the β-NMR studies yielded a differential magnetic hyperfine anomaly of $^{39}\Delta^{47} = 0.360(9)\,\%$, see Section 5.4, which is in very good agreement with the previous measurements from the COLLAPS experiment that determined $^{39}\Delta^{47} = 0.28(16)\,\%$ [88]. It improves the uncertainty by one order of magnitude. The uncertainty in the value determined in this thesis mostly results from the literature values of the hyperfine structure parameters A, while the uncertainty from the β-NMR measurements is in the range of several ppm.

This differential hyperfine anomaly $^{39}\Delta^{47}$ is now exploited in combination with state-of-the-art nuclear and atomic theory to obtain new information on the spin and orbital angular momentum contributions to the magnetic dipole moment of the nucleus [9]. Hartree-Fock approximations are applied by atomic theory collaborators (J. Ginges and B. Roberts, University of Queensland, Brisbane) to obtain the atomic wave functions for Equations (2.29) and (2.30). The nuclear magnetisation distribution and the spin asymmetries, see Section 2.3.2, are calculated with Density Functional Theory (DFT) by nuclear theory collaborators (groups of J. Dobaczewski, University of York, and M. Kortelainen, University of Jyvaskyla) [102, 15, 31] for the isotopes ^{39}K and ^{47}K [9]. Individual contributions from the spin and the orbital angular momentum of the proton and the spin contribution of the neutron were obtained. The magnetic moments of the two isotopes, their differential hyperfine anomaly and the quadrupole moment ^{39}K based on these DFT calculations are listed in Table 6.1 together with the experimental values [88, 108]. As seen here, the calculations yield a good agreement for the quadrupole moment Q. However, the magnetic moments obtained with DFT for the two isotopes do not show an agreement with the experimental results. In the case of ^{39}K for example, the magnetic moment has two large contributions from the spin and the orbital angular momentum, which should cancel out and result in a small magnetic moment [108]. Only small uncertainties in either of the contributions thus results in large deviations for the magnetic moment from the observed values. The values obtained for the magnetic moment with DFT are more comparable to those of the single particle model, which are also listed in Table 6.1 for reference. Moreover, the differential hyperfine anomaly based on the DFT calculations is significantly too large.

To investigate these discrepancies, it is now assumed that the orbital angular momentum contributions $\langle L_\pi \rangle_\mathrm{DFT}$ to the magnetic moments obtained from the DFT calculations are correct since these isotopes have simple configurations that are doubly-magic with one proton hole. The spin contributions $\langle s_\pi \rangle_\mathrm{DFT}$ of ^{39}K and ^{47}K are then scaled to meet the experimental magnetic moments, see last column in Table 6.1. This in return

Table 6.1.: The experimental magnetic moments, the hyperfine anomaly and the quadrupole moment compared to calculations based on the single particle model and DFT. The last column lists the values based on the scaled contributions from the DFT. For details, see text.

	Experiment	Single Particle	DFT	Scaled
$\mu_I(^{39}\mathrm{K})$ / μ_N	0.391 470(8)	0.1243	0.1259	0.391 470
$\mu_I(^{47}\mathrm{K})$ / μ_N	1.936 182(19)	2.7928	2.6630	1.936 182
$^{39}\Delta^{47}$ / %	0.360(9)	1.425	1.269	0.372
$Q(^{39}\mathrm{K})$ / b	0.0585(6)	0.0562	0.0546	

also results in a significantly better agreement of the differential hyperfine anomaly that differs only 1.3 σ from the experimental value.

As a next step, the spin contribution $\langle S_\pi \rangle_\mathrm{DFT}$ and the orbital contribution $\langle L_\pi \rangle_\mathrm{DFT}$ of the protons are both scaled under the constraint that their combination yields the magnetic moment of the respective isotope, confer Equation (2.4). The very small spin contribution from the neutrons is not scaled and will be considered negligible. In the single particle model, the orbital angular momentum contributions from $s_{1/2}$ protons are zero. However, in the DFT calculations other nucleons can contribute to the magnetic moment, giving a small, non-zero orbital contribution. This results in an infinite number of scaled spin contributions $\langle S_\pi \rangle / \langle S_\pi \rangle_\mathrm{DFT}$ that with their associated scaled orbital contribution $\langle L_\pi \rangle / \langle L_\pi \rangle_\mathrm{DFT}$ reproduce the magnetic moments. Figure 6.1 shows some of these combinations: The two x-axes represent the relative spin contribution (lower axis) and the associated relative orbital contribution (upper axis) of ^{39}K that together reproduce the magnetic moment of ^{39}K. Conversely, the two y-axes represent the relative spin contribution (left axis) and the associated relative orbital contribution (right axis) of ^{47}K that together reproduce the magnetic moment of ^{47}K. Shown in blue and red are the unscaled DFT results $\langle L_\pi \rangle / \langle L_\pi \rangle_\mathrm{DFT} = 1$ of the orbital contributions and the associated scaled values $\langle S_\pi \rangle / \langle S_\pi \rangle_\mathrm{DFT}$ of the spin contributions.

Similar to the magnetic moment, the Bohr-Weisskopf effect is dependent on contributions from the spin and the orbital angular momentum, as seen in Equations (2.27) and (2.28). However, the dependency is different compared to that of the magnetic moment, confer Equation (2.4). The differential hyperfine anomaly can thus serve as an additional constraint on the possible combinations of $\langle S_\pi \rangle / \langle S_\pi \rangle_\mathrm{DFT}$ and $\langle L_\pi \rangle / \langle L_\pi \rangle_\mathrm{DFT}$. These combinations of the spin and orbital contribution now have to reproduce not only the corresponding magnetic moments but also the differential hyperfine anomaly $^{39}\Delta^{47}$ linking the two isotopes. If this constraint is considered, the number of possible combinations of $\langle S_\pi \rangle / \langle S_\pi \rangle_\mathrm{DFT}$ and $\langle L_\pi \rangle / \langle L_\pi \rangle_\mathrm{DFT}$ for the two isotopes is significantly reduced. The black band in Figure 6.1 shows the spin contributions of ^{39}K with their associated orbital contributions and the spin contributions of ^{47}K with their associated orbital contribution that reproduce the experimental differential hyperfine anomaly of $^{39}\Delta^{47} = 0.360(9)\,\%$.

The orbital angular momentum contributions $\langle L_\pi \rangle_\mathrm{DFT}$ to the magnetic moments are again considered to be correct due to the isotopes having a doubly-magic configuration with one proton hole. Therefore, relative orbital contributions $\langle L_\pi \rangle / \langle L_\pi \rangle_\mathrm{DFT}$ far from one are unlikely. Consequently, the spin contribution of ^{47}K needs to be reduced to around $74\,\%$ of $\langle S_\pi \rangle_\mathrm{DFT}$ to reproduce the magnetic moments and the differential hyperfine anomaly, as seen in Figure 2.1. Small deviations from this $74\,\%$ contribution would require large changes in the orbital contribution, as seen in the corresponding axis on the right, to still correctly reproduce the differential hyperfine anomaly. At the same time, if the relative orbital contribution of ^{39}K is slightly different from one, the orbital contribution of ^{47}K also requires large changes.

The above behaviour implies that the discrepancies of the magnetic moments and the hyperfine anomaly

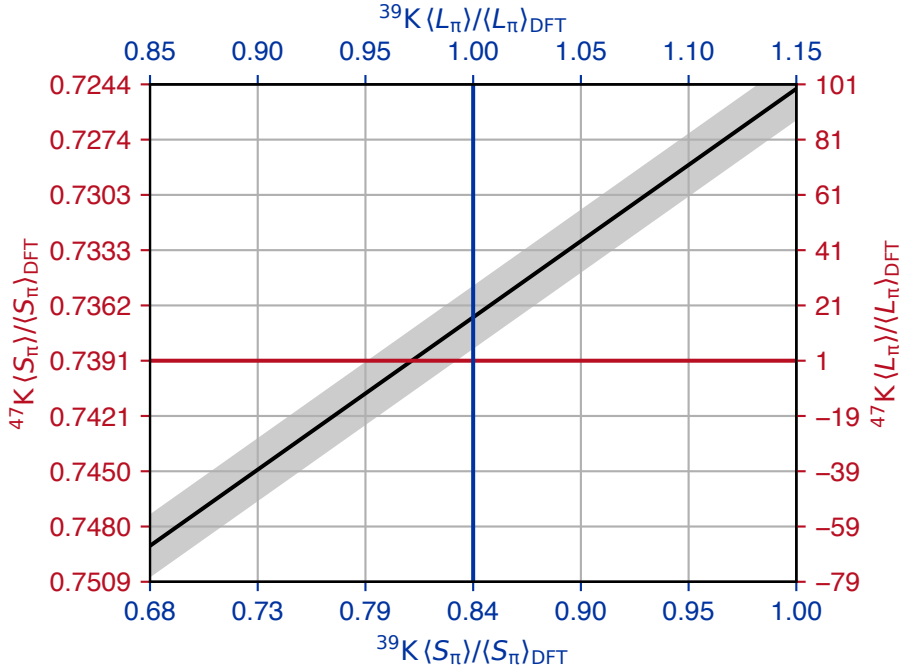

Figure 6.1.: The two x-axes show the scaled spin and orbital contributions of ^{39}K that reproduce the magnetic moment of ^{39}K. Conversely, the two y-axes indicate the scaled contributions of ^{47}K that reproduce the magnetic moment of ^{47}K. The grid serves as guidance to see the associated spin and orbital contributions of the respective isotope. The blue and the red line indicate the unscaled DFT results $\langle L_\pi \rangle / \langle L_\pi \rangle_{\mathrm{DFT}} = 1$ of the orbital contributions and the corresponding scaled values $\langle S_\pi \rangle / \langle S_\pi \rangle_{\mathrm{DFT}}$ of the spin contributions. Shown in black is the combination of the contributions of ^{39}K and ^{47}K that when linked reproduce the differential hyperfine anomaly $^{39}\Delta^{47}$ presented in this thesis.

arise from spin-like contributions. In return, this speaks in favour of the theoretical description of the nucleus missing a spin-like term. The deliberations in this section can thus serve as an input to nuclear theory to improve the ability of nuclear structure models to predict the magnetic moment [9].

7. Summary and Outlook

This thesis presented technical developments at VITO, the β-NMR setup at the ISOLDE facility, with the aim of enabling precision-studies of the hyperfine anomaly. It also demonstrated a proof-of-principle experiment for such studies.

Preparatory work for these measurements included the installation of a $4.7\,\mathrm{T}$ superconducting magnet and a pair of new β detectors. A crucial component in the scope of these upgrades, and also a main part of this thesis, was a new data acquisition system (DAQ) that provides the user with full flexibility and comprehensive features during and after the experiment. The implemented system is called VCS. It is a fully-digital DAQ that also controls all measurement hardware necessary to record hyperfine structure scans, T_1 scans and β-NMR scans. At its core is an FPGA-based oscilloscope that handles signals which require a high time-resolution. The FPGA not only receives and sends trigger signals from and to ISOLDE, but also processes the detected β particles with a temporal resolution of $8\,\mathrm{ns}$. Each registered event is characterised in real time on the FPGA through a selection of properties, including the time of arrival, amplitude and the integral. Only these properties are then streamed to the host computer, where they are saved and provide a live view of the incoming data. This approach allows for an in-depth data analysis since all relevant information on each individual β event is available even in post-processing. For example, it is possible to select events based on the integral of the signal and thus the energy of the β particle.

A comprehensive analysis approach that exploits the time of arrival of each β event registered with VCS are the two-dimensional fits introduced in this thesis. They consider not only the frequency dependency of the β-NMR spectra but also take into account the time dependency of the signal. To achieve this, the fitting model comprises two time constants, one for the T_1 relaxation and another one for the faster relaxation in the resonance case. This second time constant is dependent on the applied frequency ν with a Lorentzian function. $\chi^2_{\mathrm{red}} \approx 1$ was obtained for the evaluation of all data sets. The two-dimensional fits thus show an excellent agreement with the measured β decay asymmetry. This is remarkable since the line shape of the resonances changes over time. The broadening as well as the plateau occurring when the resonance is saturated are reproduced properly by the two-dimensional fits, regardless of the type of the sample or the relaxation time of the signal. Consequently, it could be demonstrated that it is beneficial to increase the rf amplitude and thus the B_1 field for the β-NMR measurements, which enhances the statistical significance of the resonance, even if a saturation occurs. The two-dimensional fits yield an improved precision in the Larmor frequency compared to one-dimensional fits that consider only the frequency dependency. Moreover, the presented approach yields complementary information on the β-NMR studies. For example, it is possible to directly extract the T_1 relaxation constant and the initial value of the β decay asymmetry after the polarisation. Future experiments will therefore benefit from the two-dimensional fits due to their more precise, comprehensive and complete representation of the acquired β decay symmetry.

The upgraded VITO beam line including VCS was then commissioned with β-NMR studies of ^{47}K ($I = 1/2$, $t_{1/2} = 17.5\,\mathrm{s}$) implanted into KCl crystals and the ionic liquid EMIM-DCA. It was the first time that K was spin-polarised at VITO through optical pumping. The Larmor frequencies of the ^{47}K in EMIM-DCA measurements were consistent, with uncertainties of typically less than $0.3\,\mathrm{ppm}$. The magnetic moment $\mu_I(^{47}\mathrm{K}) = 1.936\,182(19)\mu_\mathrm{N}$ presented here is two orders of magnitude more precise than the literature value

[88]. It could thereby be verified that the VITO beamline in its upgraded form will be able to perform the high-precision β-NMR studies required to determine differential hyperfine anomalies.

The differential hyperfine anomaly $^{39}\Delta^{47} = 0.360(9)\,\%$ of ^{47}K with respect to the reference isotope ^{39}K was derived based on the data recorded during the commissioning experiments. Its uncertainty is one order of magnitude smaller than that of the literature value [88]. Next, it was presented how the differential hyperfine anomaly can be exploited to derive the ratio of the spin contribution and the orbital contribution to the magnetic moment. The distribution of magnetisation in the nucleus was obtained by collaborators using Hartree-Fock calculations and DFT. It is then used to determine combinations of spin and orbital contribution that result in a correct reproduction of the experimental values of the magnetic moments of ^{39}K and ^{47}K. In addition, the differential hyperfine anomaly $^{39}\Delta^{47}$ also needs to be reproduced by the respective combinations of spin and orbital contribution. This constraint results in a significant reduction of the possible combinations, all of which require the spin contribution to be scaled down with respect to the DFT result in order to reproduce the two magnetic moments and the differential hyperfine anomaly. Hence, it is probable that missing terms in the theoretical description of the nucleus behave like the spin contribution to the magnetic moment. This information can help to improve the ability of nuclear structure models to predict magnetic moments. Here, the sensitivity of the differential hyperfine anomaly to the composition of the magnetic moment is illustrated.

More studies of the differential hyperfine anomaly are foreseen at the VITO beamline in the future. The first experiment is planned with ^{11}Be [10] to determine the magnetic moment of ^{11}Be with ppm-precision. In combination with equally precise hyperfine A factors [110, 115], it will be possible to derive the differential hyperfine anomaly $^{9}\Delta^{11}$ between ^{9}Be and ^{11}Be with great precision and thus investigate the nuclear structure of these isotopes. The uncertainty in $^{39}\Delta^{47}$ determined in this thesis predominantly results from the uncertainty in the hyperfine structure parameters A, while the uncertainty from the β-NMR studies is in comparison negligible. Therefore, it is essential to measure the A parameters with greater precision. With this objective, the VITO setup will be adapted to enable measuring the hyperfine structure A parameters with laser-rf double excitations in the near future.

The work presented here also prepared for another experiment named DeVITO, which extends the VITO beamline at ISOLDE by adding γ ray detectors and neutron time-of-flight detectors. This allows to acquire β-γ-neutron coincidences of spin-polarised beams, with the aim of firmly assigning spins and parities of the involved excited states. Further measurements that are currently being prepared at VITO include β-NMR studies of ^{8}Li. It is planned to investigate the diffusion of Li ions, which are a promising candidate for electrolytes in future solid-state batteries [94]. The two-dimensional fitting approach presented in this thesis will greatly facilitate these measurements by yielding the relaxation times for every β-NMR spectrum in addition to a precise Larmor frequency.

A. Appendix

This appendix provides supplementary figures that contribute to the understanding of the two-dimensional approach of fitting β-NMR resonances that was developed in Section 5.2.4.

A.1. Evaluation of the line shape of the two-dimensional β-NMR fits

In order to evaluate how representative the line shape of the two-dimensional fits of the β-NMR resonances is to the acquired β decay asymmetry, projections of the fit along the frequency axis are presented for different times t together with the corresponding $0.2\,\mathrm{s}$-time bin of the data. This is presented for β-NMR measurements of ^{47}K in EMIM-DCA in Figure A.1 and for ^{47}K in KCl in Figure A.2. The frequency axis was not re-binned for this representation. It is evident that the line shape of the two-dimensional fits reproduces the measured β decay asymmetry appropriately over all frequencies and at all times, including the broadening and the establishment of a plateau when the resonance saturates. More information on this is found in Section 5.2.4.

A.2. Evaluation of saturation curves

Presented here is supplementary material for a better understanding of the influence of the rf amplitude of the B_1 field on the β-NMR measurements of ^{47}K implanted into KCl and EMIM-DCA, as discussed in Section 5.3.1.

A.2.1. Three-dimensional visualisation of saturation measurements for ^{47}K in KCl and EMIM-DCA

The three-dimensional representations of the measurements of ^{47}K in KCl, seen in Figure A.3, and in EMIM-DCA, seen in Figure A.4, illustrate the influence of the rf amplitude on the amplitude and the width of the β-NMR resonances. Stated with the rf amplitude is furthermore the χ^2_{red} of each respective fit.

A.2.2. Saturation curves of ^{47}K in EMIM-DCA

Analogous to the saturation measurements of ^{47}K in KCl, β-NMR resonances with varying rf amplitude were also recorded for ^{47}K in EMIM-DCA. Three-dimensional visualisations of the corresponding fits are shown in Figure A.4. The amplitudes of the β-NMR resonances and their FWHM as a function of the time and the applied rf amplitude are depicted in Figure A.5. Seen here is that the amplitude of the β-NMR resonance diminishes faster compared to the measurements of ^{47}K in KCl. This is the case because ^{47}K in EMIM-DCA has a shorter T_1 relaxation off resonance that is more comparable to the relaxation T_{on} on resonance. It is in return beneficial to increase the rf amplitude in order to shorten T_{on} and thus enhance the amplitude of the resonance.

Figure A.6 shows the Larmor frequency ν_{L} and the corresponding uncertainty $\delta\nu_{\mathrm{L}}$ of the saturation measurements. The value of ν_{L} corresponding to the rf amplitude of $25\,\mathrm{mV}$ differs significantly and indicates the highest uncertainty. This results from a relatively low β-NMR amplitude, which is around a factor of two smaller compared to the resonance recorded with an rf amplitude of $50\,\mathrm{mV}$, as seen in Figure A.5.

Table A.1.: Additional fitting parameters of the β-NMR measurements of ^{47}K in EMIM-DCA.

Timestamp	SampleID	χ^2_{red}	Step size / Hz	T_1 / s	T_{on} / s
20220522-011603	EP1_K47_NMR_5	1.02	20	4.1(2)	0.6(1)
20220522-025524	EP1_K47_NMR_7	1.00	50	3.4(3)	1.6(2)
20220522-032022	EP1_K47_NMR_8	1.02	50	2.5(2)	0.8(1)
20220522-034518	EP1_K47_NMR_9	1.03	50	2.7(2)	0.7(1)
20220522-045844	EP1_K47_NMR_13	1.02	25	3.0(2)	0.9(1)
20220522-062619	EP1_K47_NMR_14	1.01	50	2.6(1)	1.1(1)
20220523-075809	EP2_K47_NMR_1	1.04	25	3.0(1)	0.6(1)
20220523-090149	EP2_K47_NMR_2	1.03	25	3.0(1)	0.4(1)
20220714-223719	EP1_NMR_008	1.01	100	2.0(1)	0.8(1)
20220715-000047	EP1_NMR_009	1.00	100	2.1(1)	0.7(2)
20220715-002510	EP1_NMR_010	0.97	100	2.1(1)	0.7(2)
20220715-005209	EP1_NMR_011	1.05	100	2.8(3)	0.9(2)
20220715-011631	EP1_NMR_014	1.05	100	2.1(1)	0.8(1)
20220715-025208	EP1_NMR_015	1.06	100	2.3(1)	1.0(1)
20221123-061849	K47_mika_E1_NMR001	1.06	139	4.6(5)	0.4(1)
20221123-063419	K47_mika_E1_NMR003	1.01	100	4.5(3)	0.5(1)
20221123-065249	K47_mika_E1_NMR004	1.13	100	4.3(1)	1.4(1)

In combination with the maximum amplitude occurring later when fewer β particles are detected and the uncertainty in the determined β decay asymmetry is larger, the statistical significance of the β-NMR resonance is reduced. Applying a sufficient rf amplitude is therefore particularly important for measurements with short T_1 relaxation times, such as ^{47}K in EMIM-DCA.

A.2.3. Additional parameters of the β-NMR spectra of ^{47}K in EMIM-DCA

Additional parameters of the two-dimensional fits of the β-NMR measurements implanting ^{47}K into EMIM-DCA are listed in Table A.1. These include the relaxation constants χ^2_{red}, the step size of the applied frequency ν as well as the time constants T_1 and T_{on} of the data sets that are considered for the precision studies of the hyperfine anomaly and the magnetic moment of ^{47}K.

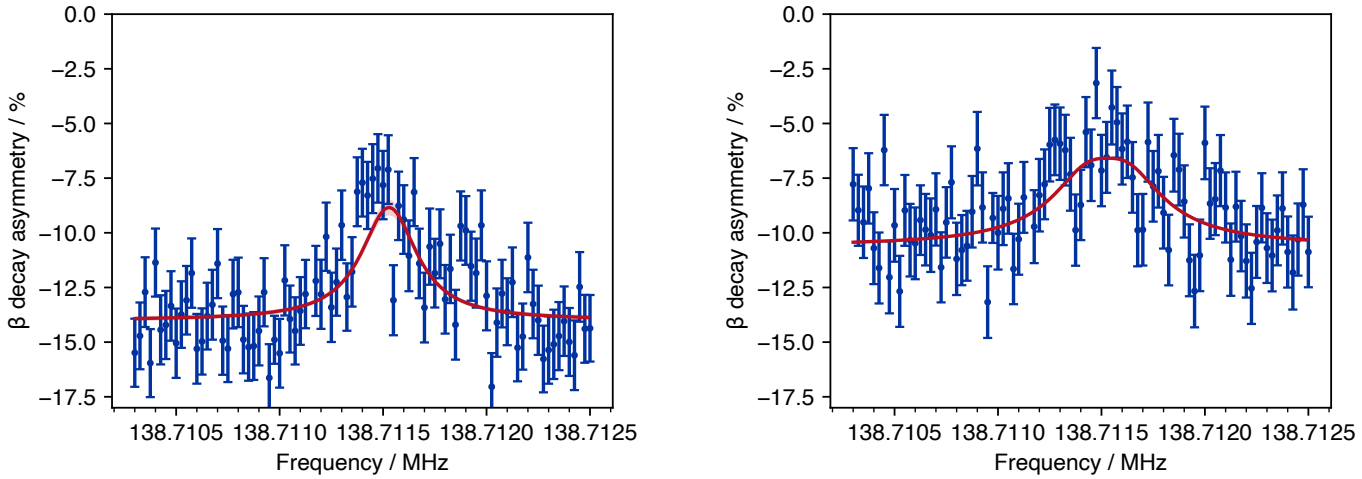

(a) $t = 0.6\,\mathrm{s}$.

(b) $t = 2.4\,\mathrm{s}$.

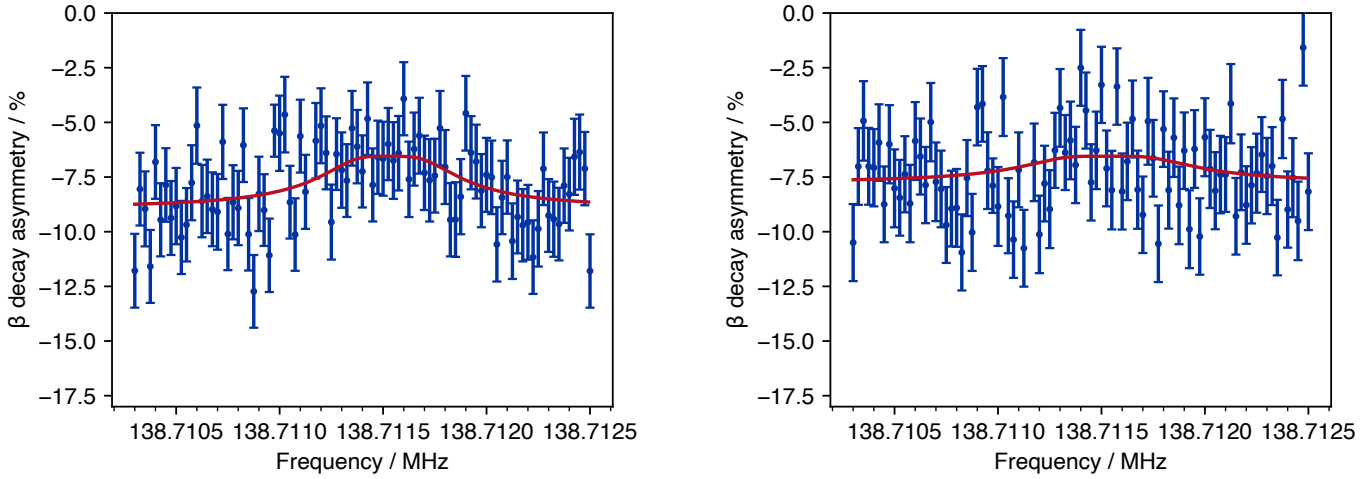

(c) $t = 4.0\,\mathrm{s}$.

(d) $t = 6.0\,\mathrm{s}$.

Figure A.1.: Projection of the two-dimensional fit of the β-NMR resonance of ^{47}K in EMIM-DCA along the frequency axis for different times t. The measured β decay asymmetry corresponding to this time (bin width $0.2\,\mathrm{s}$) is shown as well.

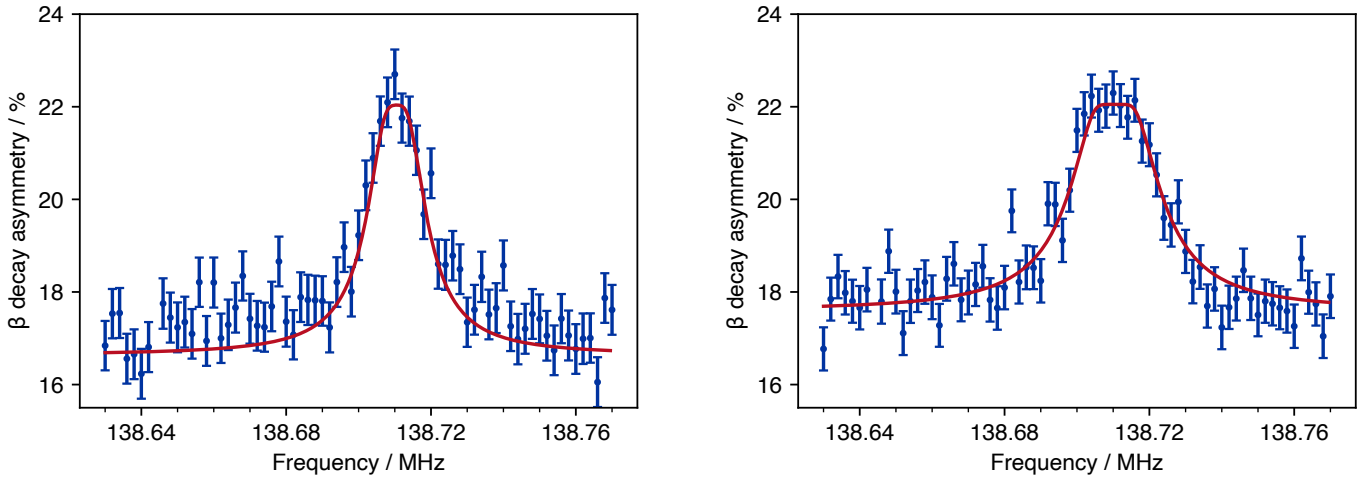

(a) $t = 3.4\,\mathrm{s}$.

(b) $t = 7.8\,\mathrm{s}$.

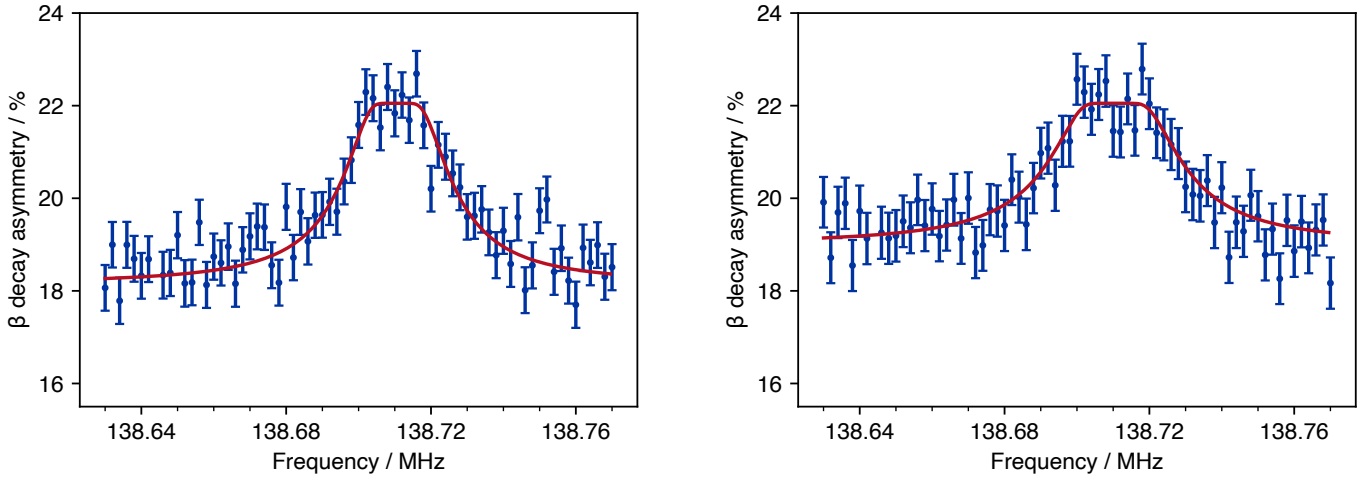

(c) $t = 10.8\,\mathrm{s}$.

(d) $t = 16.4\,\mathrm{s}$.

Figure A.2.: Projection of the two-dimensional fit of the β-NMR resonance of ^{47}K in KCl along the frequency axis for different times t. The measured β decay asymmetry corresponding to this time (bin width $0.2\,\mathrm{s}$) is shown as well.

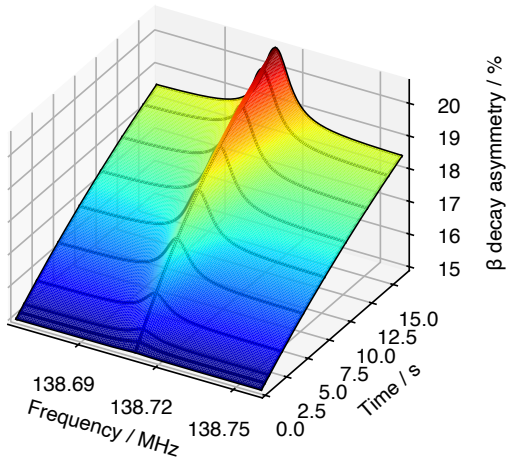

(a) $5\,\mathrm{mV}$, $\chi^2_{\mathrm{red}} = 1.06$.

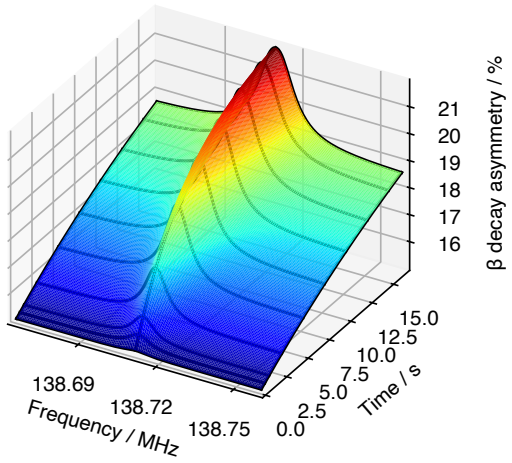

(b) $10\,\mathrm{mV}$, $\chi^2_{\mathrm{red}} = 1.08$.

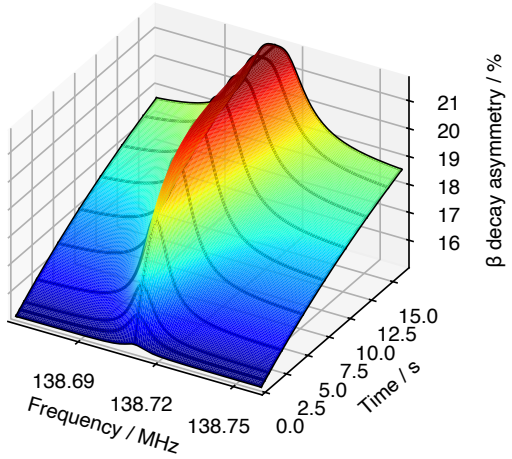

(c) $20\,\mathrm{mV}$, $\chi^2_{\mathrm{red}} = 1.12$.

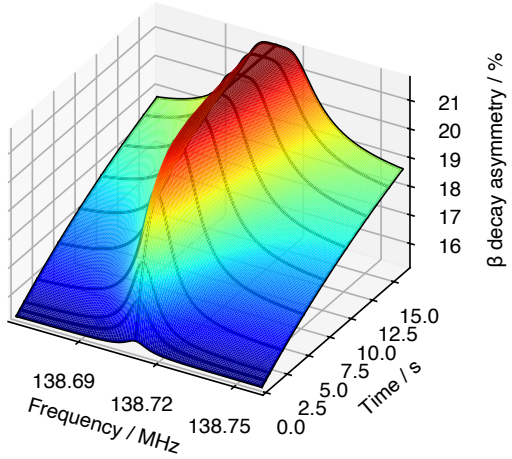

(d) $30\,\mathrm{mV}$, $\chi^2_{\mathrm{red}} = 1.10$.

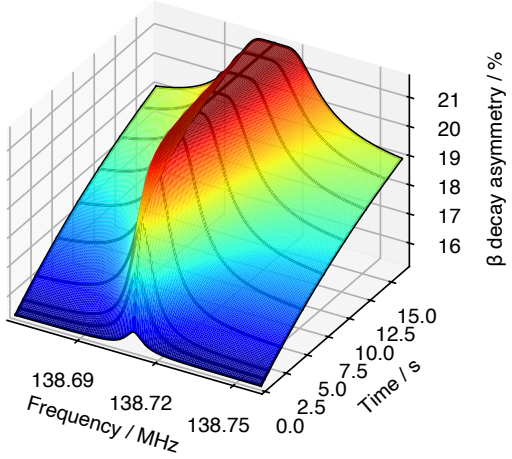

(e) $40\,\mathrm{mV}$, $\chi^2_{\mathrm{red}} = 1.11$.

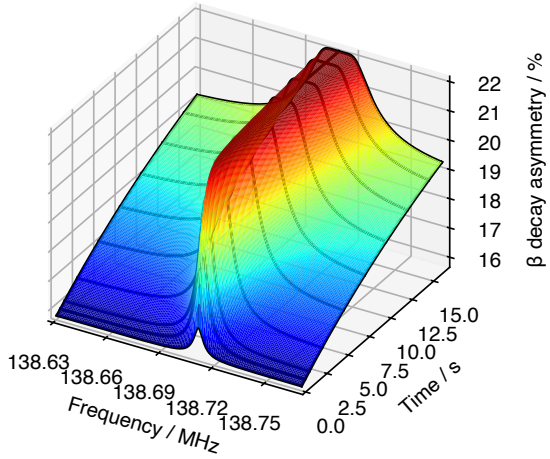

(f) $50\,\mathrm{mV}$, $\chi^2_{\mathrm{red}} = 1.16$.

Figure A.3.: Three-dimensional representations of the fits of the β-NMR measurements of ^{47}K in KCl recorded with different rf amplitudes of $5\,\mathrm{mV}$ to $50\,\mathrm{mV}$. Given is also the χ^2_{red} of the respective fit. It is clearly visible how a higher rf amplitude results in a faster relaxation in the resonance case and in return an earlier saturation and a higher statistical significance of the resonance as well as a more pronounced plateau.

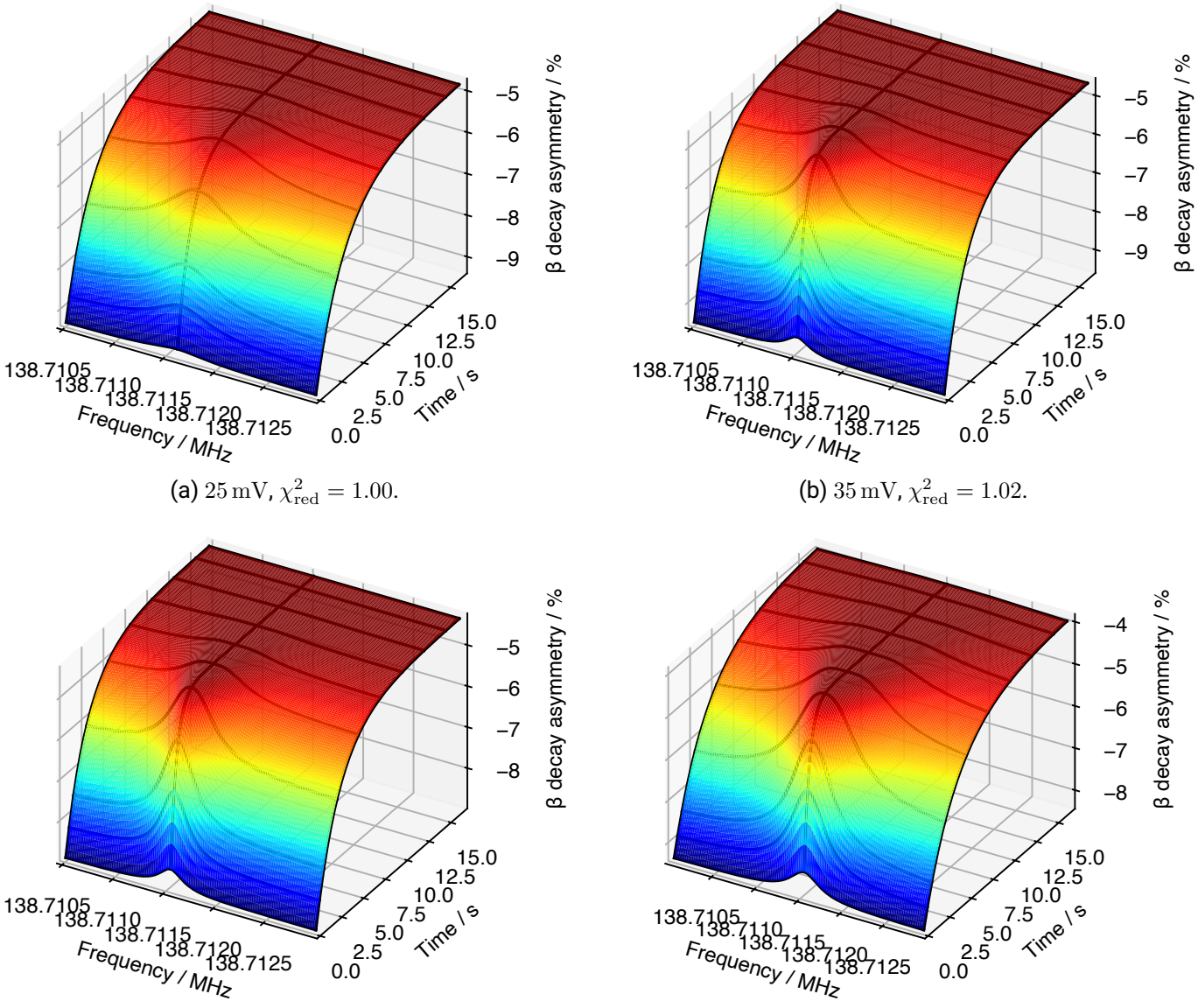

(a) $25\,\mathrm{mV}$, $\chi^2_{\mathrm{red}} = 1.00$.

(b) $35\,\mathrm{mV}$, $\chi^2_{\mathrm{red}} = 1.02$.

(c) $42\,\mathrm{mV}$, $\chi^2_{\mathrm{red}} = 1.03$.

(d) $50\,\mathrm{mV}$, $\chi^2_{\mathrm{red}} = 1.02$.

Figure A.4.: Three-dimensional representations of the fits of the β-NMR measurements of ^{47}K in EMIM-DCA recorded with different rf amplitudes of $25\,\mathrm{mV}$ to $50\,\mathrm{mV}$. Given is also the χ^2_{red} of the respective fit. A higher rf amplitude causes a faster relaxation in the resonance case and an enhanced statistical significance.

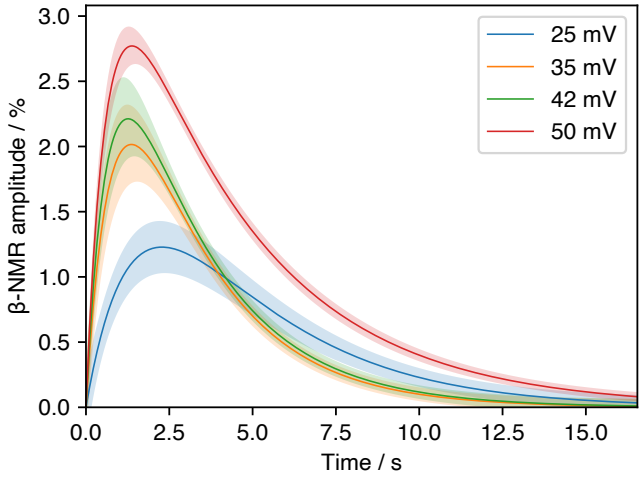

(a) Amplitude of the fitted peaks.

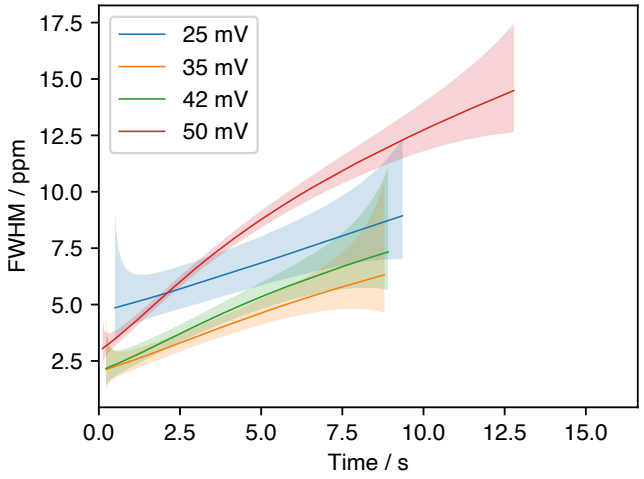

(b) FWHM of the fitted peak.

Figure A.5.: The amplitude (a) of the β-NMR resonances and (b) their FWHM as a function of the rf amplitude and the time for measurements of ^{47}K in EMIM-DCA.

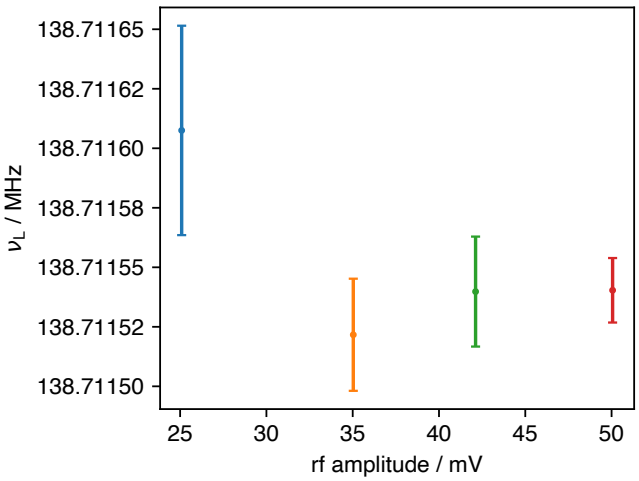

(a) ν_{L} as a function of the rf amplitude.

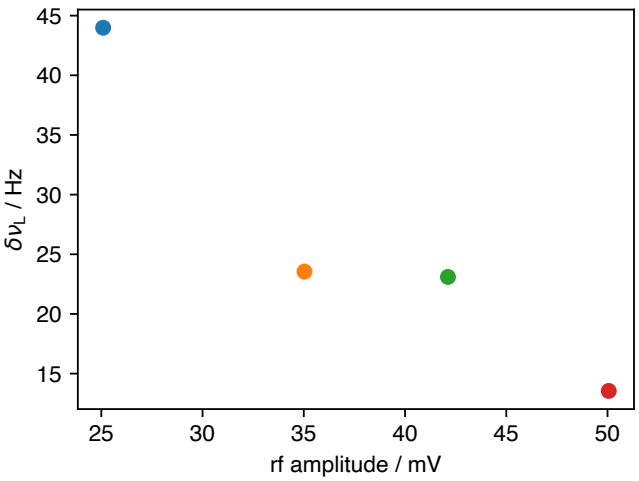

(b) $\delta\nu_{\mathrm{L}}$ as a function of the rf amplitude.

Figure A.6.: Larmor frequencies ν_{L} (a) of β-NMR spectra of ^{47}K in EMIM-DCA as a function of the rf amplitude and (b) their respective uncertainties. The lower uncertainty at an rf amplitude of $50\,\mathrm{mV}$ is also partially caused by higher rf resolution of $20\,\mathrm{Hz}$ as opposed to $50\,\mathrm{Hz}$ for the other measurements.

Bibliography

[1] A Abragam. *The Principles of Nuclear Magnetism*. Clarendon Press, 1961. ISBN: 9780198520146.

[2] G. P. Arrighini, M. Maestro, and R. Moccia. "Magnetic Properties of Polyatomic Molecules. I. Magnetic Susceptibility of H2O, NH3, CH4, H2O2". In: *The Journal of Chemical Physics* 49 (2 July 1968), pp. 882–889. ISSN: 0021-9606. DOI: 10.1063/1.1670155.

[3] Atta-ur-Rahman. *Nuclear Magnetic Resonance*. Springer US, 1986. ISBN: 978-1-4612-9350-7. DOI: 10.1007/978-1-4612-4894-1.

[4] J. Ballof et al. "The upgraded ISOLDE yield database – A new tool to predict beam intensities". In: *Nuclear Instruments and Methods in Physics Research Section B: Beam Interactions with Materials and Atoms* 463 (Jan. 2020), pp. 211–215. ISSN: 0168-583X. DOI: 10.1016/J.NIMB.2019.05.044.

[5] A. E. Barzakh et al. "Hyperfine anomaly in gold and magnetic moments of I=11/2- gold isomers". In: *Physical Review C* 101 (3 Mar. 2020), p. 034308. ISSN: 2469-9985. DOI: 10.1103/PhysRevC.101.034308.

[6] Edwin D. Becker. *High Resolution NMR*. Academic Press, 2000.

[7] A Beckmann, K D Böklen, and D Elke. "Precision measurements of the nuclear magnetic dipole moments of 6Li, 7Li, 23Na, 39K and 41K". In: *Zeitschrift für Physik* 270 (3 1974), pp. 173–186. ISSN: 0044-3328. DOI: 10.1007/BF01680407. URL: https://doi.org/10.1007/BF01680407.

[8] Markus Bier and S Dietrich. "Vapour pressure of ionic liquids". In: *Molecular Physics* 108 (2 2010), pp. 211–214. DOI: 10.1080/00268971003604609. URL: https://doi.org/10.1080/00268971003604609.

[9] ML Bissell et al. "Hyperfine anomaly in a short-lived nucleus 47K: state-of-the-art experiment meets state-of-the-art atomic and nuclear theory". In: *To be submitted* (2024).

[10] ML Bissell et al. *Magnetic moment of 11Be with ppm accuracy*. 2023. URL: https://cds.cern.ch/record/2845944.

[11] F Bloch. "Nuclear Induction". In: *Physical Review* 70 (7-8 Oct. 1946), pp. 460–474. DOI: 10.1103/PhysRev.70.460. URL: https://link.aps.org/doi/10.1103/PhysRev.70.460.

[12] Aage Bohr. "Nuclear Magnetic Moments and Atomic Hyperfine Structure". In: *Physical Review* 81 (3 Feb. 1951), pp. 331–335. ISSN: 0031-899X. DOI: 10.1103/PhysRev.81.331.

[13] Aage Bohr and Ben R Mottelson. *Nuclear Structure*. World Scientific Publishing Company, Jan. 1998. ISBN: 978-981-02-3197-2. DOI: 10.1142/3530.

[14] Aage Bohr and V. F. Weisskopf. "The Influence of Nuclear Structure on the Hyperfine Structure of Heavy Elements". In: *Physical Review* 77 (1 Jan. 1950), pp. 94–98. ISSN: 0031-899X. DOI: 10.1103/PhysRev.77.94.

[15] J. Bonnard et al. "Nuclear DFT electromagnetic moments in heavy deformed open-shell odd nuclei". In: *Physics Letters B* 843 (Aug. 2023), p. 138014. ISSN: 03702693. DOI: 10.1016/j.physletb.2023.138014.

[16] M. J.G. Borge. “Highlights of the ISOLDE facility and the HIE-ISOLDE project”. In: *Nuclear Instruments and Methods in Physics Research, Section B: Beam Interactions with Materials and Atoms* 376 (June 2016), pp. 408–412. ISSN: 0168583X. DOI: 10.1016/j.nimb.2015.12.048.

[17] Maria Borge and Yacine Kadi. “ISOLDE at CERN”. In: *Nuclear Physics News* 26 (4 2016), pp. 6–13. DOI: 10.1080/10619127.2016.1249214. URL: https://doi.org/10.1080/10619127.2016.1249214.

[18] Maria J G Borge and Björn Jonson. “ISOLDE past, present and future”. In: *Journal of Physics G: Nuclear and Particle Physics* 44 (4 Apr. 2017), p. 044011. ISSN: 0954-3899. DOI: 10.1088/1361-6471/aa5f03.

[19] R. N. Bracewell. *The Fourier transform and its applications*. McGraw-Hill, 2000. ISBN: 0-07-303938-1.

[20] H Brand and D Neidherr. *CS++ – NI Actor Framework-based Class Library*. 2016.

[21] H Brand and D Neidherr. *Status of the CS framework and its successor CS++*. 2014. DOI: 10.15120/GR-2015-1-FG-GENERAL-41.

[22] Holger Brand. *Private Communication*. 2021.

[23] B.H. Bransden and C.J. Joachain. *Physics of Atoms and Molecules*. 1st. Longman, 1983, p. 686. ISBN: 9780582444010. DOI: 10.1887/0750303468/b293c2.

[24] G. Breit and I. I. Rabi. “Measurement of Nuclear Spin”. In: *Physical Review* 38 (11 Dec. 1931), pp. 2082–2083. ISSN: 0031-899X. DOI: 10.1103/PhysRev.38.2082.2.

[25] S. Büttgenbach. “Magnetic hyperfine anomalies”. In: *Hyperfine Interactions* 20 (1 July 1984), pp. 1–64. ISSN: 0304-3834. DOI: 10.1007/BF02043319.

[26] B Castel and I. S. Towner. *Modern Theories of Nuclear Moments*. Oxford University Press, 1990. ISBN: 9780198517283.

[27] R. Catherall et al. “An overview of the HIE-ISOLDE Design Study”. In: *Nuclear Instruments and Methods in Physics Research Section B: Beam Interactions with Materials and Atoms* 317 (PART B Dec. 2013), pp. 204–207. ISSN: 0168-583X. DOI: 10.1016/J.NIMB.2013.07.030.

[28] R. Catherall et al. “The ISOLDE facility”. In: *Journal of Physics G: Nuclear and Particle Physics* 44 (9 Aug. 2017). ISSN: 13616471. DOI: 10.1088/1361-6471/aa7eba.

[29] CERN. *CERN Annual report 2017*. 2018. URL: https://cds.cern.ch/record/2624296.

[30] J Croese et al. “High-accuracy liquid-sample β-NMR setup at ISOLDE”. In: *Nuclear Instruments and Methods in Physics Research Section A: Accelerators, Spectrometers, Detectors and Associated Equipment* 1020 (2021), p. 165862. ISSN: 0168-9002. DOI: https://doi.org/10.1016/j.nima.2021.165862. URL: https://www.sciencedirect.com/science/article/pii/S0168900221008470.

[31] J Dobaczewski et al. “Solution of universal nonrelativistic nuclear DFT equations in the Cartesian deformed harmonic-oscillator basis. (IX) HFODD (v3.06h): a new version of the program”. In: *Journal of Physics G: Nuclear and Particle Physics* 48 (10 Oct. 2021), p. 102001. ISSN: 0954-3899. DOI: 10.1088/1361-6471/ac0a82.

[32] T. William Donnelly and Ingo Sick. “Elastic magnetic electron scattering from nuclei”. In: *Reviews of Modern Physics* 56 (3 July 1984), pp. 461–566. ISSN: 0034-6861. DOI: 10.1103/RevModPhys.56.461.

[33] Charlotte Duchemin et al. “CERN-MEDICIS: A Review Since Commissioning in 2017”. In: *Frontiers in Medicine* 8 (July 2021). ISSN: 2296858X. DOI: 10.3389/fmed.2021.693682.

[34] Simon B Duckett and Christopher J Sleigh. “Applications of the parahydrogen phenomenon: A chemical perspective”. In: *Progress in Nuclear Magnetic Resonance Spectroscopy* 34 (1 Feb. 1999), pp. 71–92. ISSN: 00796565. DOI: 10.1016/S0079-6565(98)00027-2.

[35] H.T. Duong et al. “Atomic beam magnetic resonance apparatus for systematic measurement of hyperfine structure anomalies (Bohr-Weisskopf effect)”. In: *Nuclear Instruments and Methods in Physics Research Section A: Accelerators, Spectrometers, Detectors and Associated Equipment* 325 (3 Feb. 1993), pp. 465–474. ISSN: 01689002. DOI: 10.1016/0168-9002(93)90392-U.

[36] Vernon J. Ehlers et al. “Hyperfine Structure of 67Ga and 72Ga”. In: *Physical Review* 176 (1 Dec. 1968), pp. 25–42. ISSN: 0031-899X. DOI: 10.1103/PhysRev.176.25.

[37] James Eills et al. *Spin Hyperpolarization in Modern Magnetic Resonance*. Feb. 2023. DOI: 10.1021/acs.chemrev.2c00534.

[38] ENI. *ENI 240L Operation and Service*. 1992.

[39] Valentin Fedosseev et al. “Ion beam production and study of radioactive isotopes with the laser ion source at ISOLDE”. In: *Journal of Physics G: Nuclear and Particle Physics* 44 (8 Aug. 2017), p. 084006. ISSN: 0954-3899. DOI: 10.1088/1361-6471/aa78e0. URL: https://iopscience.iop.org/article/10.1088/1361-6471/aa78e0.

[40] Eugene Feenberg and Kenyon C. Hammack. “Nuclear Shell Structure”. In: *Physical Review* 75 (12 June 1949), pp. 1877–1893. ISSN: 0031-899X. DOI: 10.1103/PhysRev.75.1877.

[41] H. Frånberg et al. “Off-line commissioning of the ISOLDE cooler”. In: *Nuclear Instruments and Methods in Physics Research Section B: Beam Interactions with Materials and Atoms* 266 (19-20 Oct. 2008), pp. 4502–4504. ISSN: 0168-583X. DOI: 10.1016/J.NIMB.2008.05.097.

[42] Takehisa Fujita and Akito Arima. “Magnetic hyperfine structure of muonic and electronic atoms”. In: *Nuclear Physics A* 254 (2 Dec. 1975), pp. 513–541. ISSN: 03759474. DOI: 10.1016/0375-9474(75)90234-1.

[43] Tim Giles. “ISOLDE V”. In: *Nuclear Instruments and Methods in Physics Research, Section B: Beam Interactions with Materials and Atoms* 463 (Jan. 2020), pp. 254–257. ISSN: 0168583X. DOI: 10.1016/j.nimb.2019.05.025.

[44] J.S.M. Ginges and V.V. Flambaum. “Violations of fundamental symmetries in atoms and tests of unification theories of elementary particles”. In: *Physics Reports* 397 (2 July 2004), pp. 63–154. ISSN: 03701573. DOI: 10.1016/j.physrep.2004.03.005.

[45] W. Gins et al. “A new beamline for laser spin-polarization at ISOLDE”. In: *Nuclear Instruments and Methods in Physics Research Section A: Accelerators, Spectrometers, Detectors and Associated Equipment* 925 (May 2019), pp. 24–32. ISSN: 0168-9002. DOI: 10.1016/J.NIMA.2019.01.082.

[46] Boyd M. Goodson. “Nuclear Magnetic Resonance of Laser-Polarized Noble Gases in Molecules, Materials, and Organisms”. In: *Journal of Magnetic Resonance* 155 (2 Apr. 2002), pp. 157–216. ISSN: 10907807. DOI: 10.1006/jmre.2001.2341.

[47] Alexander Gottberg et al. “Billion-fold enhancement in sensitivity of nuclear magnetic resonance spectroscopy for magnesium ions in solution”. In: *ChemPhysChem* 15 (18 2014), pp. 3929–3932. ISSN: 14397641. DOI: 10.1002/cphc.201402619.

[48] R. R. Gupta, ed. *Diamagnetic Susceptibility and Anisotropy of Inorganic and Organometallic Compounds*. Springer Berlin Heidelberg, 2007. ISBN: 978-3-540-23113-4. DOI: 10.1007/978-3-540-44694-1.

[49] Dennis A. Hall et al. “Polarization-Enhanced NMR Spectroscopy of Biomolecules in Frozen Solution”. In: *Science* 276 (5314 May 1997), pp. 930–932. ISSN: 0036-8075. DOI: 10.1126/science.276.5314.930.

[50] R D Harding et al. “Magnetic Moments of Short-Lived Nuclei with Part-per-Million Accuracy: Toward Novel Applications of beta-Detected NMR in Physics, Chemistry, and Biology”. In: *Phys. Rev. X* 10 (4 2020). DOI: 10.1103/PhysRevX.10.041061.

[51] Robin K. Harris et al. “Further conventions for NMR shielding and chemical shifts (IUPAC Recommendations 2008)”. In: *Pure and Applied Chemistry* 80 (1 Jan. 2008), pp. 59–84. ISSN: 1365-3075. DOI: 10.1351/pac200880010059.

[52] Robin K. Harris et al. “NMR nomenclature. Nuclear spin properties and conventions for chemical shifts(IUPAC Recommendations 2001)”. In: *Pure and Applied Chemistry* 73 (11 Jan. 2001), pp. 1795–1818. ISSN: 1365-3075. DOI: 10.1351/pac200173111795.

[53] Kris L. G. Heyde. “The Nuclear Shell Model”. In: 1990, pp. 54–135. DOI: 10.1007/978-3-642-97203-4_4.

[54] Roy E. Hoffman. “Measurement of magnetic susceptibility and calculation of shape factor of NMR samples”. In: *Journal of Magnetic Resonance* 178 (2 Feb. 2006), pp. 237–247. ISSN: 10907807. DOI: 10.1016/j.jmr.2005.09.009.

[55] Jim Hokanson. *TDMS Reader*. 2024. URL: https://de.mathworks.com/matlabcentral/fileexchange/30023-tdms-reader.

[56] Andrej Hurajt and Andrej Antusek. “Ab initio computational protocol for NMR shielding of beta-NMR probes”. In: *In preparation* (2024).

[57] National Instruments. *PXIe-1083 User Guide*. July 2020.

[58] National Instruments. *PXIe-5170/5171 User Guide*. June 2017.

[59] National Instruments. *PXIe-6341 User Guide*. 2020.

[60] ISOLDE. *Layout of the ISOLDE facility*. URL: https://isolde.web.cern.ch/isolde-logos-layouts-and-templates.

[61] Karol Jackowski, Michał Jaszuński, and Marcin Wilczek. “Alternative Approach to the Standardization of NMR Spectra. Direct Measurement of Nuclear Magnetic Shielding in Molecules”. In: *The Journal of Physical Chemistry A* 114 (7 Feb. 2010), pp. 2471–2475. ISSN: 1089-5639. DOI: 10.1021/jp9096056.

[62] Attila Jancso et al. “TDPAC and β-NMR applications in chemistry and biochemistry”. In: *Journal of Physics G: Nuclear and Particle Physics* 44 (6 2017), p. 064003. ISSN: 0954-3899. DOI: 10.1088/1361-6471/aa666b. URL: http://stacks.iop.org/0954-3899/44/i=6/a=064003?key=crossref.cf23e8ad0d6361338471985a7e054241.

[63] M Jankowski et al. “Fully-upgraded beta-NMR setup at ISOLDE for high-precision high-field studies”. In: *To be submitted* (2024).

[64] Michał Jaszuński et al. *The determination of accurate nuclear magnetic dipole moments and direct measurement of NMR shielding constants*. Nov. 2012. DOI: 10.1016/j.pnmrs.2012.03.002.

[65] B Jonson and A Richter. “More than three decades of ISOLDE physics”. In: *Hyperfine Interactions* 129 (1 2000), pp. 1–22. ISSN: 1572-9540. DOI: 10.1023/A:1012689128103. URL: https://doi.org/10.1023/A:1012689128103.

[66] A. Kanellakopoulos et al. “Nuclear moments of germanium isotopes near N=40”. In: *Physical Review C* 102 (5 Nov. 2020). ISSN: 24699993. DOI: 10.1103/PhysRevC.102.054331.

[67] Beatrice Karg and Magdalena Kowalska. *Liquid β-NMR studies of the interaction of Na and K cations with DNA G-quadruplex structures*. 2020. URL: https://cds.cern.ch/record/2717964.

[68] Beatrice Karg and Magdalena Kowalska. *Liquid β-NMR studies of the interaction of Na and K cations with DNA G-quadruplex structures*. 2022. URL: https://cds.cern.ch/record/2798880.

[69] James Keeler. *Understanding NMR Spectroscopy*. Apollo - University of Cambridge Repository, 2002. DOI: 10.17863/CAM.968. URL: https://www.repository.cam.ac.uk/handle/1810/257040.

[70] M Kowalska. *Interaction of Na ions with DNA G-quadruplex structures studied directly with Na beta-NMR spectroscopy*. 2017. URL: https://cds.cern.ch/record/2266838.

[71] M Kowalska et al. “New laser polarization line at the ISOLDE facility”. In: *Journal of Physics G: Nuclear and Particle Physics* 44 (8 Aug. 2017), p. 084005. ISSN: 0954-3899. DOI: 10.1088/1361-6471/aa77d7.

[72] M. Kowalska et al. “Nuclear ground-state spins and magnetic moments of Mg27, Mg29, and Mg31”. In: *Physical Review C - Nuclear Physics* 77 (3 Mar. 2008). ISSN: 1089490X. DOI: 10.1103/PhysRevC.77.034307.

[73] Magdalena Kowalska. *Online commissioning of the laser-polarization setup at VITO*. 2016. URL: https://cds.cern.ch/record/2157088.

[74] Kenneth S Krane. *Introductory Nuclear Physics*. Wiley, 1988.

[75] Erich Kugler. “The ISOLDE facility”. In: *Hyperfine Interactions* 129 (1 2000), pp. 23–42. ISSN: 1572-9540. DOI: 10.1023/A:1012603025802. URL: https://doi.org/10.1023/A:1012603025802.

[76] M H Levitt. *Spin Dynamics: Basics of Nuclear Magnetic Resonance*. Wiley, 2018. ISBN: 978-0-470-51117-6.

[77] Ewa Lopienska. “The CERN accelerator complex, layout in 2022. Complexe des accélérateurs du CERN en janvier 2022”. In: (2022). General Photo. URL: https://cds.cern.ch/record/2800984.

[78] E. Mané et al. “An ion cooler-buncher for high-sensitivity collinear laser spectroscopy at ISOLDE”. In: *European Physical Journal A* 42 (3 Dec. 2009), pp. 503–507. ISSN: 14346001. DOI: 10.1140/epja/i2009-10828-0.

[79] K. N. Marsh, J. A. Boxall, and R. Lichtenthaler. “Room temperature ionic liquids and their mixtures - A review”. In: vol. 219. May 2004, pp. 93–98. DOI: 10.1016/j.fluid.2004.02.003.

[80] Maria G. Mayer. “On Closed Shells in Nuclei”. In: *Physical Review* 74 (3 Aug. 1948), pp. 235–239. ISSN: 0031-899X. DOI: 10.1103/PhysRev.74.235.

[81] A. Mooser et al. “Direct high-precision measurement of the magnetic moment of the proton”. In: *Nature* 509 (7502 May 2014), pp. 596–599. ISSN: 0028-0836. DOI: 10.1038/nature13388.

[82] R. Neugart and G. Neyens. “Nuclear Moments”. In: Springer Berlin Heidelberg, 2006, pp. 135–189. DOI: 10.1007/3-540-33787-3_4.

[83] Matt Newville et al. *lmfit/lmfit-py: 1.3.1*. Apr. 2024. DOI: 10.5281/zenodo.10998841. URL: https://doi.org/10.5281/zenodo.10998841.

[84] G. Neyens et al. “Measurement of the spin and magnetic moment of31 Mg: Evidence for a strongly deformed intruder ground state”. In: *Physical Review Letters* 94 (2 2005), pp. 1–4. ISSN: 00319007. DOI: 10.1103/PhysRevLett.94.022501.

[85] Gerda Neyens. “Nuclear magnetic and quadrupole moments for nuclear structure research on exotic nuclei”. In: *Reports on Progress in Physics* 66 (4 Apr. 2003), pp. 633–689. ISSN: 0034-4885. DOI: 10.1088/0034-4885/66/4/205.

[86] Onsemi. *Silicon Photomultipliers (SiPM), Low-Noise, Blue-Sensitive C-Series SiPM Sensors*. 2014. URL: www.onsemi.com.

[87] J Papuga et al. “Spins and Magnetic Moments of 49K and 51K: Establishing the 1/2+ and 3/2+ Level Ordering Beyond N=28”. In: *Physical Review Letters* 110 (17 Apr. 2013), p. 172503. DOI: 10.1103/PhysRevLett.110.172503. URL: https://link.aps.org/doi/10.1103/PhysRevLett.110.172503.

[88] J. Papuga et al. “Shell structure of potassium isotopes deduced from their magnetic moments”. In: *Physical Review C - Nuclear Physics* 90 (3 Sept. 2014). ISSN: 1089490X. DOI: 10.1103/PhysRevC.90.034321.

[89] T. J. Parolin et al. “High resolution β-NMR study of 8Li implanted in gold”. In: *Physical Review B* 77 (21 2008), p. 214107. ISSN: 1098-0121. DOI: 10.1103/PhysRevB.77.214107. URL: https://link.aps.org/doi/10.1103/PhysRevB.77.214107.

[90] J.R. Persson. “Table of hyperfine anomaly in atomic systems — 2023”. In: *Atomic Data and Nuclear Data Tables* 154 (Nov. 2023), p. 101589. ISSN: 0092640X. DOI: 10.1016/j.adt.2023.101589.

[91] Román Picazo-Frutos et al. “Zero- to Ultralow-Field Nuclear Magnetic Resonance Enhanced with Dissolution Dynamic Nuclear Polarization”. In: *Analytical Chemistry* (Dec. 2022). ISSN: 0003-2700. DOI: 10.1021/acs.analchem.2c02649.

[92] Monika Piersa-Silkowska. “Beta-decay studies of very neutron-rich indium isotopes”. PhD thesis. University of Warsaw, 2021.

[93] E. M. Purcell, H. C. Torrey, and R. V. Pound. “Resonance Absorption by Nuclear Magnetic Moments in a Solid”. In: *Physical Review* 69 (1-2 Jan. 1946), pp. 37–38. ISSN: 0031-899X. DOI: 10.1103/PhysRev.69.37.

[94] Gregory Rees, Amy Sparks, and Magdalena Kowalska. *Measuring Interfacial Ionic Conductivity in All-Solid-State-Batteries with Li β-NMR Spectroscopy*. 2023. URL: https://cds.cern.ch/record/2873743.

[95] Adam Reeve. *npTDMS*. 2024. URL: https://pypi.org/project/npTDMS/.

[96] Peter Ring and Peter Schuck. *The Nuclear Many-Body Problem*. Springer-Verlag Berlin, 1980. ISBN: 978-3-540-21206-5.

[97] Jenny E. Rosenthal and G. Breit. “The Isotope Shift in Hyperfine Structure”. In: *Physical Review* 41 (4 Aug. 1932), pp. 459–470. ISSN: 0031-899X. DOI: 10.1103/PhysRev.41.459.

[98] S. Rothe et al. “Laser ion beam production at CERN-ISOLDE: New features - More possibilities”. In: *Nuclear Instruments and Methods in Physics Research, Section B: Beam Interactions with Materials and Atoms* 376 (June 2016), pp. 91–96. ISSN: 0168583X. DOI: 10.1016/j.nimb.2016.02.024.

[99] S. Rothe et al. “Targets and ion sources at CERN-ISOLDE — Facilities and developments”. In: *Nuclear Instruments and Methods in Physics Research Section B: Beam Interactions with Materials and Atoms* 542 (Sept. 2023), pp. 38–44. ISSN: 0168-583X. DOI: 10.1016/J.NIMB.2023.05.058.

[100] R F Garcia Ruiz et al. “Perspectives for the VITO beam line at ISOLDE, CERN”. In: *EPJ Web Conf.* 93 (2015), p. 7004. ISSN: 2100014X. DOI: 10.1051/epjconf/20159307004. URL: http://dx.doi.org/10.1051/epjconf/20159307004.

[101] W Sahm and A Schwenk. “39K, 40K and 41K Nuclear Magnetic Resonance Studies”. In: 29 (12 1974), pp. 1754–1762. DOI: doi:10.1515/zna-1974-1208. URL: https://doi.org/10.1515/zna-1974-1208.

[102] P L Sassarini et al. “Nuclear DFT analysis of electromagnetic moments in odd near doubly magic nuclei”. In: *Journal of Physics G: Nuclear and Particle Physics* 49 (11 Nov. 2022), 11LT01. ISSN: 0954-3899. DOI: 10.1088/1361-6471/ac900a.

[103] Florian Scheck. *Quantum Physics*. 2nd. Vol. 1. Springer-Verlag Berlin Heidelberg 2013, 2013, p. 746. ISBN: 9780521852777. DOI: 10.1093/oxfordhb/9780199696253.013.28. URL: http://oxfordhandbooks.com/view/10.1093/oxfordhb/9780199696253.001.0001/oxfordhb-9780199696253-e-28.

[104] V M Shabaev. “Hyperfine structure of hydrogen-like ions”. In: *Journal of Physics B: Atomic, Molecular and Optical Physics* 27 (24 Dec. 1994), pp. 5825–5832. ISSN: 0953-4075. DOI: 10.1088/0953-4075/27/24/006.

[105] Charles P. Slichter. *Principles of Magnetic Resonance*. Vol. 1. Springer Berlin Heidelberg, 1990. ISBN: 978-3-642-08069-2. DOI: 10.1007/978-3-662-09441-9.

[106] M. Stachura et al. “Versatile Ion-polarized Techniques On-line (VITO) experiment at ISOLDE-CERN”. In: *Nuclear Instruments and Methods in Physics Research Section B: Beam Interactions with Materials and Atoms* 376 (June 2016), pp. 369–373. ISSN: 0168-583X. DOI: 10.1016/J.NIMB.2016.02.030.

[107] A.N. State et al. “The slow control system of the FRS Ion Catcher”. In: *Nuclear Instruments and Methods in Physics Research Section A: Accelerators, Spectrometers, Detectors and Associated Equipment* 1034 (July 2022), p. 166772. ISSN: 01689002. DOI: 10.1016/j.nima.2022.166772.

[108] N J Stone. *Table of recommended nuclear magnetic dipole moments*. 2019. URL: http://inis.iaea.org/search/search.aspx?orig_q=RN:51052833%20https://www-nds.iaea.org/publications/indc/indc-nds-0794.pdf.

[109] N J Stone and H Postma. *Low-temperature Nuclear Orientation*. North-Holland, 1986. ISBN: 9780444869944.

[110] A. Takamine et al. “Hyperfine Structure Constant of the Neutron Halo Nucleus 11Be”. In: *Physical Review Letters* 112 (16 Apr. 2014), p. 162502. ISSN: 0031-9007. DOI: 10.1103/PhysRevLett.112.162502.

[111] Alberto Tampieri et al. “A brief introduction to the basics of NMR spectroscopy and selected examples of its applications to materials characterization”. In: *Physical Sciences Reviews* 6 (1 Feb. 2021). ISSN: 2365-659X. DOI: 10.1515/psr-2019-0086.

[112] Pico Technology. *PicoScope 2200A Series PC Oscilloscopes User’s Guide*. 2014.

[113] Eite Tiesinga et al. “CODATA recommended values of the fundamental physical constants: 2018”. In: *Reviews of Modern Physics* 93 (2 June 2021), p. 025010. ISSN: 0034-6861. DOI: 10.1103/RevModPhys.93.025010.

[114] Maurizio Vretenar et al. *Linac4 design report*. Vol. 6. CERN, 2020. DOI: 10.23731/CYRM-2020-006. URL: https://cds.cern.ch/record/2736208.

[115] D. J. Wineland, J. J. Bollinger, and Wayne M. Itano. “Laser-Fluorescence Mass Spectroscopy”. In: *Physical Review Letters* 50 (9 Feb. 1983), pp. 628–631. ISSN: 0031-9007. DOI: 10.1103/PhysRevLett.50.628.

[116] C. S. Wu et al. “Experimental Test of Parity Conservation in Beta Decay”. In: *Physical Review* 105 (4 Feb. 1957), pp. 1413–1415. ISSN: 0031-899X. DOI: 10.1103/PhysRev.105.1413.

[117] D. T. Yordanov et al. “Spins and electromagnetic moments of Cd101–109”. In: *Physical Review C* 98 (1 July 2018), p. 011303. ISSN: 2469-9985. DOI: 10.1103/PhysRevC.98.011303.

Acknowledgments

I would like to thank everybody supporting me during my time at CERN and the writing of this thesis. It has been an absolutely unique experience, in more ways than I ever imagined.

First and foremost, I would like to thank my supervisors, Thorsten Kröll and Magdalena Kowalska, for having given me the opportunity to work on a doctoral degree. Thorsten, we may not have seen each other that often in person, but I know you were always there to support and encourage me. I truly appreciate that and I am very thankful for the warm welcome you gave me in Darmstadt. Magda, I am very grateful for the support you gave me. Our discussions were always food for thought and I am thankful for all the things you taught me.

I would then like to all current and former members of the VITO collaboration and everybody at ISOLDE.

Beatrice, Kasia and Jared, I am very glad you were there during my first year. I benefited greatly from your experiences, in physics and in life, when you were at ISOLDE and after you left. Thank you! Mateusz. I wished we had had lunch together more often. I am grateful that you were always there to talk and discuss things, to help each other in good and in bad times. I am always impressed how you manage to take care of γ-MRI and so many things at the same time. I wish you and your family all the best. Mark, thank you for supporting me in so many ways, may they be physics discussions, technical questions or British humour. Just like you are not the same without coffee, you need to know that ISOLDE would not be the same without you. Nikolay, thank you for always being in a good mood and cheering me up, even in difficult times. You have an amazing talent of making the impossible possible, even on a limited budget. Keep up the bricolage. Liss, thank you for always being so supportive and eager to improve my Spanish.

Monika and Ilaria, you have done tremendous work for the DeVITO experiment and I hope you will get the appreciation you deserve. The two of you are great physicists and you can accomplish great things. And sometimes physics can wait and you should take care of yourself.

Michael and Amy, thank you for your support in so many ways, no matter whether it was proof reading abstracts or chapters when others were not available, discussing life or just having a good time.

To the current doctoral students at VITO, Mateusz, Ilaria, Daniel and Anu, I wish you the best of luck for finishing your work in a challenging environment. Mik and Agnieszka, whenever you visited, I felt as though I had more supervisors supporting me. Thank you! I would also like to say a big thank you to Mila, Kristyna and Marek. You have always had the ability to cheer me up, even when I was in a bad mood.

Timo, thank you for taking on the task of learning French with me. You need to know that I am very happy to call you a friend. You are always there when I need you. I enjoyed our time at CERN as well as our travels or going running. I hope we will have more of all that in the future.

Tobias, thank you for being there and making my time at CERN more eventful. I am glad you managed to

finish your master thesis in our group and I wish you all the best for your future studies.

Hannes, Jonte, Stanislav and Falk. I know I have been very busy in the last few years and I have not always paid as much attention to you as I would have liked and as you would deserve. I am very grateful for having you all in my life.

Finally, I want to thank my family for always being there, in good and in bad times. A big thank you to my dad, Michael, and my uncle, Klaus, who always supported me during my time in Geneva.

To my brother, Malte Christoph. Thank you for being there and taking care of everything at home. I wish you all the best for your studies. I know you can do it and I am sure you will prosper in something you really like.

I would like to especially thank my mom, Christiane, who always believes in me and supports me in everything I do. You do so many things supporting Malte and me, some are obvious, some are subtle, and I want you to know that I am very proud to have you.

This work has been sponsored by the Wolfgang Gentner Programme of the German Federal Ministry of Education and Research (grant no. 13E18CHA).